New Materials for Stereolithography 3D Printing

Keroles B. Riad

A Thesis
In the department
of
Chemical and Materials Engineering

Presented in Partial Fulfillment of Requirements
For the Degree of
Doctor of Philosophy (The Individualized Program) at
Concordia University
Montreal, Québec, Canada

July 2021

CONCORDIA UNIVERSITY

School of Graduate Studies

This is to certify that the thesis prepared

By: Keroles B. Riad

Entitled: New Materials for Stereolithography 3D Printing

and submitted in partial fulfillment of the requirements for the degree of:

Doctor of Philosophy (Individualized Program)

complies with the regulations of the University and meets the accepted standards with respect to originality and quality.

Signed by the final examining committee:

______________________________ Chair

Dr. Rachel Berger

______________________________ External Examiner

Dr. Alexandra Teleki

______________________________ External to Program

Dr. Martin Pugh

______________________________ Thesis Supervisor

Dr. Paula Wood-Adams

______________________________ Examiner

Dr. Pantcho Stoyanov

______________________________ Thesis Co-supervisor

Dr. Jerome Clavérie

______________________________ Thesis Co-supervisor

Dr. Suong Hoa

Approved by ______________________________

Dr. Rachel Berger, Graduate Program Director

8/18/2021 ______________________________

Dr. Mourad Debbabi, Dean Gina

Cody School of Engineering

Abstract

New Materials for Stereolithography 3D Printing

Keroles B. Riad, Ph.D.

Concordia University, 2021

It is the dream of every engineer to be able to design unrestrained by the limitations of conventional manufacturing and assembly. The technology of 3D printing brings those dreams at our fingertips, but is curtailed by the lack of materials that are appropriate for functional use. In the case of stereolithography 3D printing, the photocurable epoxy resin currently used is unstable under sunlight and is mechanically weak. Sunlight can excite currently used photo initiators compelling 3D printed parts to continue to polymerize, making it unstable. Further, epoxy resins are categorically weak due to its poor network structure.

Here, I introduce metal oxide semiconducting nanoparticles as a new class of initiators for epoxy photopolymerization. I demonstrate that the crystal structure of the semiconducting nanoparticles significantly affects the reaction kinetics of epoxy photopolymerization. I illustrate that the TiO_2(B) crystal structure, that was never observed before in flame-made titania, doubles the rate of epoxy photopolymerization relative to P25 titania, the gold standard for photocatalysis. The bandgap energy of metal oxide semiconducting nanoparticles can easily be controlled by selecting from a myriad of various standard materials and controlling their crystal size taking advantage of their quantized effect. Thus, I also demonstrate the ability to synthesize silica-embedded quantum dots using the industrially established technology of flame spray pyrolysis. Finally, I also demonstrate that graphene oxide liquid crystals can be photocured into a paper-like macroscopic structure with comparable mechanical properties to benchmark samples prepared according to the literature. This thesis contributes distinct steps towards photostable and strong stereolithography 3D printing resin.

Dedication

I dedicate this thesis to my nurses and doctors in the medical day center in the Glen hospital and the old Montreal children hospital; I owe them my life.

Acknowledgment

I thank my supervisors: Professors Wood-Adams, Hoa and Claverie for their invaluable support, guidance, extreme patience and for making my research experience so fulfilling. I thank Professor Pratsinis, Dr Wegner and everyone in the particle technology laboratory in ETH Zürich in Switzerland for their hospitality and invaluable guidance. I am also thankful to the undergraduate students who I had the privilege to supervise over the course of this research: Hannah Hackney and Rémi Ehounou. I am grateful for my lab mates for their help and support. I am also grateful to NSERC and Concordia University for their financial support. Finally, I am grateful to my family: Basem, Mervat, Gerges and Philo for bearing with me and for their unconditional love.

Contribution of Authors

Chapter 3 is an article that is co-authored with Dr. Alexandre Arnold, and Professors Jerome Claverie, Suong Hoa and Paula Wood-Adams. I have conceptualized the project, designed and executed the experiments, and wrote the manuscript all with the guidance of the listed professors. The NMR component of the study was conducted and interpreted by Dr Alexandre Arnold.

Chapter 4 is an article that is co-authored with Professor Paula Wood-Adams and Dr. Karsten Wegner. I have conceptualized the project, designed and executed the experiments, and wrote the manuscript all with the guidance of the listed co-authors. Dr Wagner mentored my learning of nanotechnology and, specifically, trained me on the FSP technology during my two research visits (spanning 9 months combined) to the Particle Technology Laboratory at ETH in Zürich headed by Professor Sotiris Pratsinis.

Chapter 5 is an article that is co-authored with Professors Suong Hoa and Paula Wood-Adams. I have conceptualized the project, designed and executed the experiments, and wrote the manuscript all with the guidance of the listed professors.

Chapter 6 is a draft manuscript that is yet to be submitted to an academic journal. This article is co-authored with Professors Suong Hoa and Paula Wood-Adams. I have conceptualized the project, designed and executed the experiments, and drafted the manuscript all with the guidance of the listed professors.

TABLE OF CONTENTS

List of Figures

List of Tables

1. Introduction

Material development drives many emerging technologies allowing for the rapid development of countless applications in many prosperous industries. Photocurable materials are at the center of nonconventional manufacturing, coating and dentistry among many technologies. This Ph.D. thesis aims to develop new photocurable materials for sterelithography 3D printing that address two major obstacles: 1) the instability of photocurable resin in sunlight, and 2) the categorical weakness of photocurable resin relative to their metal counterparts.

A more detailed review of the 3D printing technology can be found in my master's thesis.[1] Briefly, the 3D printing[2] technology works like a normal home printer that deposits ink on a paper one line at a time. A picture forms as these lines stack next to each other. Similarly, a 3D printer deposits two dimensional layers of material one on top of the other to create a three-dimensional shape. A designer does not need to worry about how a tool's cutting edge will access the part because of the additive nature of 3D printing. Therefore, 3D printing allows for the relatively cheap creation of complicated designs that are either too expensive or impossible to machine conventionally. However, the lack of 3D printable materials with adequate properties is curtailing the functional applications of 3D printing.

Several 3D printing processes exist such as fusion deposition, selective laser sintering and stereolithography. Fusion deposition uses filaments of materials that are easy to melt such as thermoplastics and chocolate. The filament is extruded through a nozzle equipped with a heating element. That nozzle traces in the X and Y directions to print a two-dimensional layer of material on a stage that moves in the Z direction to allow for more layers leading to a three-dimensional shape. Fusion deposition is commonly used for modeling and not functional parts due to the weak mechanical properties of thermoplastics. Parts made from fusion deposition also cannot function in high temperature environments as the prerequisite of the material is to have a low melting point. Selective laser sintering uses material in powder form such as nylon, metals and moondust that are sintered using a powerful laser. Selective laser sintering is one of the processes collectively referred to as metal 3D printing used in the industry. Metal 3D printing is used for some functional applications because metals are strong relative to other 3D printable materials.[3,4] However, metal 3D printing suffers from poor surface finish and the fact that it is energy intensive.[2] As the world grapples with the many challenges of the climate crisis, industry must pay close attention to the amount of energy use throughout all its processes including manufacturing. For example, the aerospace industry alone is projected to consume a quarter of the remaining carbon budget for a 1.5 °C world by 2050.[5] Additionally, many industries including aerospace are moving away from metals to composite materials.[6]

This thesis focuses on stereolithography 3D printing which uses light-sensitive liquid resin (glue) that usually consists of epoxy and/or acrylics. That liquid epoxy solidifies in the areas where a UV laser traces via a photocuring reaction. Eventually, a solid layer of epoxy forms in the middle of the liquid bath. Then the laser traces again to create a second layer on top of the first. The 3D printer repeats this process until a three-dimensional part is created.[2]

The resins used in stereolithography are made of lone monomers acting as “building blocks” with functional groups serving as “linking sites”. The laser initiates a reaction via which these sites link to each other and build a solid macroscopic polymer network (Figure 1-1). This process is commonly referred to as polymerization, curing or cross-linking. The strength of the network depends on how well-connected the building blocks are, the strength of the bonds, the properties of the building blocks, and the structure of the formed network.[7]

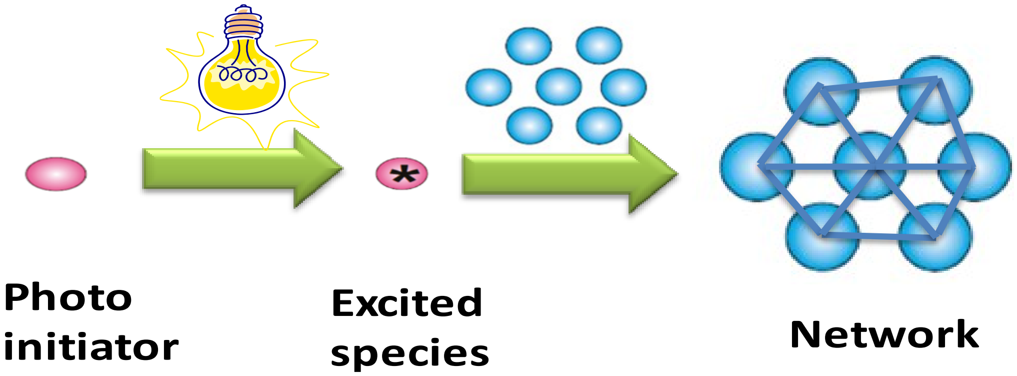

Figure 1-1: Schematic for stereolithography curing reaction initiated by light. The pink spheres represent the photo initiators while the blue sphere represent the monomers.

Stereolithography is more energy efficient than metal 3D printing. It is also faster and more accurate than other 3D printing processes. However, 3D printed parts made via stereolithography are unstable under sunlight and mechanically weak. Therefore, stereolithography is limited to modeling applications. At the beginning of this research project, I visited Axis prototypes, a 3D printing company in Montreal with more than a 20-year experience in providing stereolithography related services. During that visit, I learned that one of the main issues is the photo stability of the cured material and that UV coating is often used as a short-term fix. As an example of this, Mr Robin Clifford, Axis' managing director, talked to me about a project called "bug eye" that was intended to show children what a bug's eye looks like. Stereolithography was used to make the part using epoxy based photo curable material called DSM Somos 11122. Initially a clear UV coat was used to address photo instability issues. After approximately two to three months, the part had cracked due to increased brittleness because of photo instability. Superior coating was later used to improve the lifetime of the part to approximately three summers. Coatings only delay the problem as opposed to addressing the root cause of the photo instability.

This thesis aims to tackle two distinct challenges for stereolithography resin: instability under sunlight and poor mechanical properties. The first obstacle - the instability under sunlight - originates from the fact that all current photo-initiators have some sensitivity to sunlight.[8] That is to say that the wavelength absorption range of the commercial initiators includes a portion of the solar spectrum. Existing photo-initiators typically respond to UVA (315-400 nm) and UVB (295-315 nm) light which represents 6%[9] of the solar intensity at sea level.[10,11,12,13] Therefore, initiators that are inside parts 3D printed via stereolithography absorb sunlight, and continue to initiate polymerization. The continuing polymerization makes the part so brittle that it ultimately fractures and fails.

In this Ph.D. thesis I introduce a new class of photo-initiators that are made of semiconducting nanoparticles. The wavelength range that semiconducting nanoparticles are sensitive to is dictated by the particles' band gap energy. In turn, the band gap energy can be selected by choosing the right semiconducting material. That band gap energy can be further tuned by controlling the crystal size of the semiconducting nanoparticles using the "quantized effect". This ability to precisely control the wavelength of light that excites the semiconducting nanoparticles may allow us to select initiators that are insensitive to sunlight, and better enable us to have stable photocurable resins for stereolithography 3D printing.

The second obstacle - the relatively poor mechanical properties of photocurable resins - stems from the fact that photocured parts are made of polymers which are categorically weaker than traditional metals. For example, the tensile strengths of stereolithography resins available at Axis prototypes, a Montreal-based 3D printing company, range from 32 to 54 MPa. This weakness originates from the amorphous nature of crosslinked epoxy and/or acrylic polymers. The structure of a network is just as important to the overall strength as the intrinsic strength of individual bonds is.[7,14] Consider diamond and coal. Both are made of pure carbon-carbon bonds. Yet, diamond is much stronger than coal because of its crystal structure.

This categorical weakness of stereolithography resins is repelling industries from taking advantage of the technology. Therefore, stereolithography 3D printing is often used for prototyping and not the manufacturing of functional parts. Developing composite materials whose strengths are comparable with metals is a crucial step towards realizing the full potential of stereolithography 3D printing.

In this Ph.D. thesis, I introduce the ability to photocure graphene oxide liquid crystals. This ability transforms graphene oxide liquid crystals into a resin that is 3D printable via stereolithography. Fibers formed from graphene oxide liquid crystals have been demonstrated to possess tensile strengths higher than that of steel (300-600 MPa). This strength stems from the fact that liquid crystals have crystal-like ordering of graphene oxide sheets. Further, graphene has a Young's modulus of 1 TPa and a tensile strength of 130 GPa.[15] These mechanical properties make graphene the strongest material known. Graphene also has extraordinary thermal, optical and electrical properties that attract many industries. Creating usable three-dimensional macroscopic architectures remains a challenge. Demonstrating that graphene oxide liquid crystals can be photocured opens the door to stronger stereolithography resins.

This thesis is organized as a series of manuscripts each addressing a distinct step in the path towards achieving the objectives outlined earlier. Chapters 3, 4 and 5 address the first obstacle of instability under sunlight. Chapter 6 addresses the second obstacle of weak mechanical properties.

Chapter 3 is a manuscript that has been published in ACS Applied Nano Materials[16], and is publicly accessible via Spectrum. This article is co-authored with Dr. Alexandre Arnold, and Professors Jerome Claverie, Suong Hoa and Paula Wood-Adams. I have conceptualized the project, designed and executed the experiments, and wrote the manuscript all with the guidance of the listed professors. The NMR component of the study was conducted and interpreted by Dr. Alexandre Arnold. As shown in the graphic abstract (Figure 1-2), this article demonstrates that metal oxide semiconducting nanoparticles such as P25 Titania and flame-made ZnO photopolymerize epoxy when exposed to light. The band gap energies of P25 Titania and ZnO are in the UVA region that is within the solar spectrum. Therefore, metal oxide semiconducting nanoparticles with bigger band gap energy must be used to achieve the objective of developing a stereolithography resin that is insensitive to sunlight.

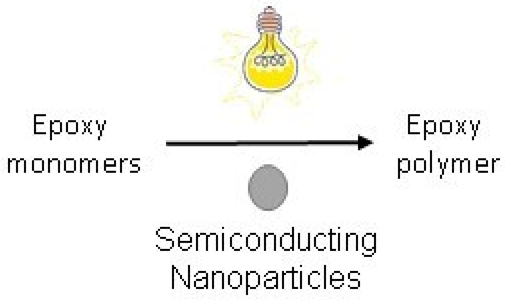

Figure 1-2: Graphic abstract introducing semiconducting nanoparticles as photoinitiators for the polymerization of epoxy.

At this stage, it is important to synthesize the quantum dots with a band gap energy that is wider than what is available in sunlight. It is also important that this synthesis method be industrially viable. Flame Spray Pyrolysis (FSP) is a mass-production technology for metal-oxide nanoparticles that has been shown to be capable of synthesizing quantum dots by using silica matrices to control the particles crystal size. Chapter 4 is a manuscript that has been published in the Materials Research Bulletin[17], and is publicly accessible via Spectrum. This article is co-authored with Professor Paula Wood-Adams and Dr. Karsten Wegner. I have conceptualized the project, designed and executed the experiments, and wrote the manuscript all with the guidance of the listed co-authors. Dr. Wagner mentored my learning of nanotechnology and, specifically, trained me on the FSP technology during my two research visits (spanning 9 months combined) to the Particle Technology Laboratory at ETH in Zürich headed by Professor Sotiris Pratsinis. This paper demonstrates that not only is flame-made Titania capable of photopolymerizing epoxy but also is 2-3 times more efficient due to the presence of a monoclinic crystal structure that has never been observed before in flame-made Titania (Figure 1-3).

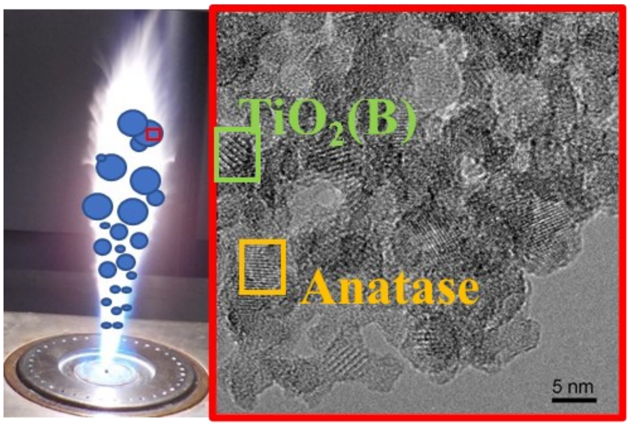

Figure 1-3: Graphic abstract demonstrating the presence of $TiO_2(B)$ *in flame-made titania.*

Now that the use of the FSP is demonstrated to maintain the photoinitiation capability of metal oxide semiconducting nanoparticles, we next go about creating the particles with a large enough band gap energy. This requires changing the metal oxide material, and utilizing the quantized effect. Chapter 5 is a manuscript published in ACS Omega (open access).[18] This article is co-authored with Professors Suong Hoa and Paula Wood-Adams. I have conceptualized the project, designed and executed the experiments, and wrote the manuscript all with the guidance of the listed professors. As shown in the graphic abstract (Figure 1-4), this article demonstrates the FSP's ability to synthesize quantum dots embedded in silica matrices of four metal oxides: ZnO, TiO_2, CuO, SnO_2. The band gap energy of the quantum dots included in that chapter range from UVC to dark red. Further, it also demonstrates that the addition of a silica matrix does not prohibit the epoxy photocuring reaction. The silica matrix slows down epoxy photopolymerization relative to pure flame-made Titania. On the other hand, the flame-made titania embedded in a silica matrix is a more efficient epoxy photoinitiator than commercial P25 Titania. Most importantly FSP-made ZnO and SnO_2 with 90% silica possessed band gap energies that are larger than what is available in sunlight on Earth. These quantum dots meet the criteria for photoinitators that can be used to make stable photocurable resin.

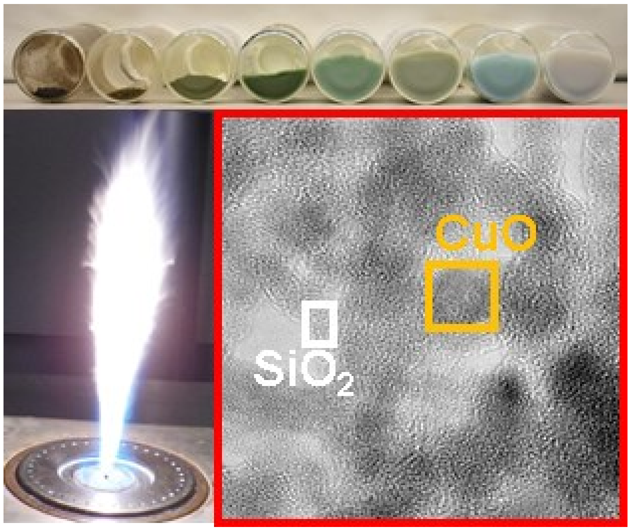

Figure 1-4: Graphic abstract featuring flame-made quantum dots.

Finally, chapter 6 is a draft manuscript that is yet to be submitted to an academic journal. This article is co-authored with Professors Suong Hoa and Paula Wood-Adams. I have conceptualized the project, designed and executed the experiments, and drafted the manuscript all with the guidance of the listed professors. As shown in the graphic abstract (Figure 1-4), it demonstrates that graphene oxide liquid crystals can be photocured into solid paper-like structures. The graphene oxide paper prepared by photocuring alcohol dispersions had comparable mechanical properties to those of benchmark samples prepared by vacuum filtering aqueous dispersions as is common in the literature.

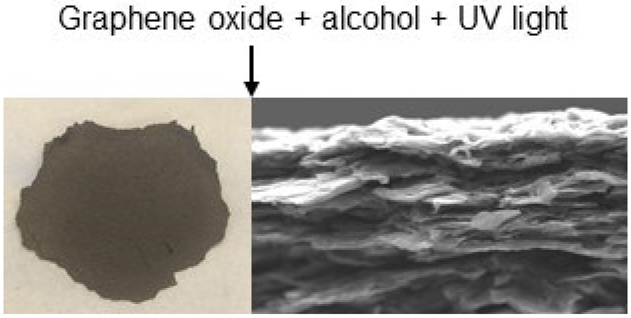

Figure 1-5: Graphic abstract featuring photocured graphene oxide paper.

The contributions of this thesis are a new class of epoxy photopolymerization catalysts, a new crystal structure in flame-titania, a mass production method for quantum dots, and the ability to photocure graphene oxide liquid crystals. Clearly, there remains more work ahead to achieve the objective of developing photostable and strong material for stereolithography 3D printing. However, not only is each one of these contributions a distinct step towards achieving that goal, but they also create opportunities for new research affecting various other applications.

2. Literature review

2.1. Photo-polymerization

Photo-polymerization is a chemical reaction triggered by light that changes the materials' phase (liquid to solid), solubility, adhesion and refractive index.[19] An array of applications has been making use of photopolymerization since Kodac developed the first synthetic photo-polymer, polyvinyl cinnamate, as a photoresist in printing plates.[19,20] These applications include the manufacturing of printed circuit boards, photocurable coatings, and stereolithography 3D printing.[19,21,22,23] Photo-polymerization can be preferable to heat polymerization because it is less unpleasant relative to heat in dentistry applications, and requires low energy.[19] However, controlling the critical wavelength required to trigger the photo-polymerization reaction remains an area of needed research.

Photo-polymerization mechanisms are generally classified into two categories: free-radical and cationic.[10] In the former, free-radicals are produced during photo-initiation via alpha cleavage or H-abstraction as shown in Figure 2-1.[10] In the latter, the initiator decomposes to generate cationic species and, ultimately, protons that ring-open reactive groups such epoxide groups.[11]

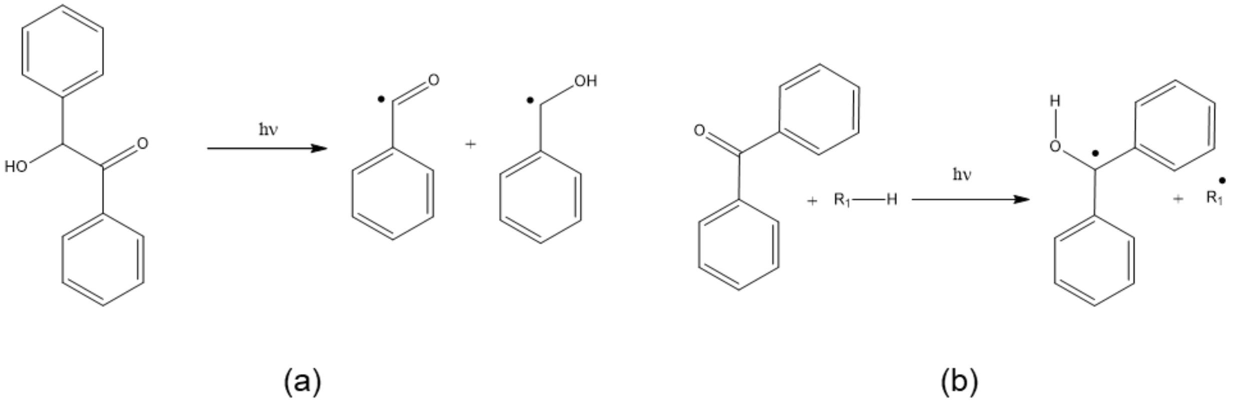

Figure 2-1: Light initiated a) α-cleavage free radical mechanism of benzoin, and b) The H-abstraction free radical mechanism of benzophenone initiated by light. Adapted from ref 10.

The radical photo-initiation of acrylic monomers has been extensively investigated using a variety of initiators including semiconducting nanoparticles.[12,24,25,26] Butylmethacrylate is showed to photopolymerize by ZnO quantum dots and other semiconducting nanoparticles like CdS via free radical photo-polymerization.[25] When the semiconducting material absorbs light of an energy equal to its bandgap energy, an electron-hole pair form. The electron in that pair acts as a free radical that initiates the polymerization of the acrylate.

In this thesis, I am interested in the photo-polymerization of epoxy, which requires a cationic initiator. Onium salts, first developed by Crivello[9], are the most used cationic initiators.[10] Equations 1 and 2, and Figure 2-2 show an example of a cationic photo-polymerization mechanism, described by Yagci et al.[10], where protons open up the epoxide rings and initiate polymerization[13]. The salt anion determines the acid strength and reaction efficiency, and must be non-nucleophilic so that it does not quench the cationic species. The salt cation governs the photochemistry, absorption wavelength, quantum yield and thermal stability because it is the component that absorbs the light.[9]

$$\mathrm{Ph_2I^+PF_6{}^-} \overset{\mathrm{h\nu}}{\rightarrow} \mathrm{PhI^{+^*}} + \mathrm{Ph^*} + \mathrm{PF_6{}^-} \qquad [1]$$

$$Ph\mathrm{I^{+^*}} + \mathrm{RH} \rightarrow \mathrm{PhI^*} + \mathrm{R} + \mathrm{H^+} \qquad [2]$$

Equations 1 and 2 are reproduced from ref 10.

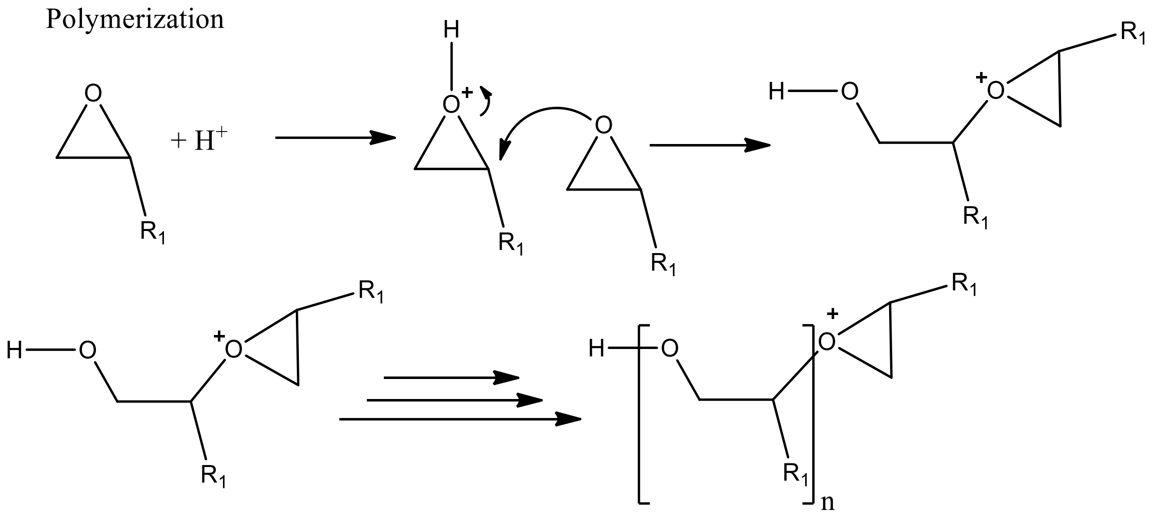

Figure 2-2: Cationic polymerization of epoxy. Adapted from ref 27.

The ozone layer blocks light of wavelengths lower than 300 nm from the solar spectrum on Earth.[8] Existing photo-initiators typically respond to UVA (315-400 nm) and UVB (295-315 nm) light which represents 6% at sea level[9] of the solar intensity at the Earth's surface.[10,11,12,13] Available photoinitiators have residual absorptions above 300 nm. Even initiators with very little absorption in this range show significant quantum yield and catalytic activity when illuminated by light above 300 nm.[8] Hare[8] explains that photo-initiators absorb light from 300-380 nm in the atmosphere and generate reactive species that further polymerize the material. Solar light therefore continuously changes the material properties of photopolymers often to the point of brittle fracture within weeks.[8] Not only is UV degradation a major problem for stereolithography 3D printing but also aircraft coating.[28] UV degradation of epoxy also releases toxic and carcinogenic volatile organic components into the environment.[29] UV absorbers and light stabilizers[28] are often used to mitigate this instability, but they only slow down degradation. Inorganic surface coatings (such as silica) [30] are also used but, like sunscreen on the beach, coating must be regularly reapplied.

Yet, past studies of cationic initiators focus on shifting the light wavelength to which the photo-initiator is sensitive towards the visible region. The intention is to replace the special lamps currently needed to quickly polymerize coatings with the solar spectrum.[10,31] The addition of various chromophores and metal complexes during the cationic salt synthesis can manipulate their absorption wavelengths, but they are costly.[9,31] Dyes could also be used as photosensitizers to broaden the absorption wavelength range.[31] The need for new initiators that are insensitive to sunlight and that allow for photostable resins remains unmet.

2.2. Quantum dots

Quantum dots are nanoparticles made of semiconducting materials and are the object of considerable interest in view of their remarkable optical and electronic properties.[32,33,34] Quantum dots have a high quantum efficiency, and narrow absorption and luminescence windows which can be conveniently tuned by changing their size due to the quantized effect[32,33,34], first observed by Ekimov and Onuschenko[35]. The quantized effect implies that the band gap energy of semiconducting nanoparticles become a function of their crystal size once that size is smaller than the material's exciton Bohr diameter, d_{Bohr}.

The exciton Bohr diameter of the semiconducting material is calculated via Equation 3. Where $\hbar = 1.05 \times 10^{-34}$ J·s is the reduced Plank's constant, ε is the dielectric constant of the material, $e = 1.6 \times 10^{-19}$ C is the elementary charge, and μ is the reduced mass of the material's exciton.

$$d_{Bohr} = 2R_{Bohr} = \frac{2\hbar^2\varepsilon}{e^2\mu} \qquad [3]$$

Equation 3 is reproduced from refs 36 and 37.

Equation 4 governs the relationship between material's crystal size (2R) and band gap energy (E^*). Where E_g is the material's bulk band gap energy (at $R\to\infty$). Equation 4 illustrates that the quantized effect is most significant at sizes below the exciton Bohr diameter but still takes place at bigger sizes. It is important to note that Equation 4 has limitations particularly at sizes below 3 nm because the effective mass approximation used in this model fails due to a significant increase in the electrons' kinetic energy.[38,39,40]

$$E^* = E_g + \frac{\hbar^2\pi^2}{2R^2\mu} - \frac{1.8e^2}{\varepsilon R} \qquad [4]$$

Equation 4 is reproduced from ref 41.

In this thesis, I study quantum dots made of SnO_2, ZnO, CuO and TiO_2. Table 1 shows the standard properties of each of those materials, where $m_0 = 9.1 \times 10^{-31}\ kg$ is the mass of a free electron.

Table 1: Material Properties

	TiO_2 (Anatase)[42]	ZnO (Zincite)	SnO_2 (Cassiterite)[43]	CuO (Monoclinic)
ε	31	3.7 (ref 44)	14	25 (ref 45)
μ/m_0	1.630	0.157 (ref 46)	0.275	0.381 (ref 47)
Eg (eV)	3.2	3.2 (ref 46)	3.6	1.5 (ref 47)
Bohr diameter (nm) from literature	2	2.5 (ref 46)	5.4	6.6-28.7 (ref 48)
Calculated Bohr diameter (nm) (eq 2)	2	2.5	5.4	7

SnO_2 is important in various applications such as lithium-ion batteries and gas sensing.[49] Scaling down the SnO_2 nanocrystal size leads to high gas sensitivity.[50] Ma et al. demonstrated that gas sensing properties are generally enhanced if the active material size is smaller than the thickness of the electron depletion layer.[51] Further, porous SnO_2 quantum dots are 5 times more sensitive than nonporous ones in gas sensing applications. [43] In fact, Wan et al. demonstrated that SnO_2 branched nanowires can detect sub-ppm concentrations of ethanol vapor without noble metal catalyst because of the small size, large surface areas, and porosity.[50] The tunable fluorescent properties of SnO_2 enable their use in nano light emitters.[52] SnO_2 is also a good anode material for battery application due to its relatively high theoretical reversable capacity.[49] On the other hand, the higher tendency of small particles to aggregate as well as the volume swell of SnO_2 lead to poor cycling stability.[49]

ZnO quantum dots are also used in UV protection films, chemical sensors, polymer stabilizer and catalysis.[41,44] The tunable fluorescent properties of ZnO allow applications in light emitting devices such as quantum lasers.[53] CuO quantum dots can be used as high temperature superconductors.[54] Further, Ben-Mohse et al[55] demonstrated that CuO nanoparticles can oxidize organic pollutants even in complete darkness. However, previous studies indicate that CuO is unstable at sizes below 25 nm.[56] TiO_2 nanoparticles are used as photocatalysts and solar cells electrodes.[42,57,58] Photo-corrosion of the semiconducting nanoparticle remains a disadvantage in photocatalytic reactions.[59]

The two most major obstacles faced by quantum dots preventing their commercialization are: 1) they are unstable mechanically (aggregate), thermally (grow with heat) and chemically (susceptible to corrosion) making their use unrepeatable, and 2) the unmet need for viable high-volume production.[49,39] The first challenge of instability is being overcome by embedding the quantum dots in amorphous matrices.[39] For example, embedding quantum dots in an amorphous carbon matrix counteracts the challenges faced quantum dots in battery applications including aggregation and volume swelling during lithiation. [49] Surprisingly, SnO_2 quantum dots embedded even in an unconducive silica matrix still showed improved properties over bare SnO_2 quantum dots when closely packed (high SnO_2 loading).[60] Quantum dots embedded in amorphous matrices have the same luminescence properties as bare ones.[61] With the advent of thermal stability, ability for repeated use, quantum dots embedded in amorphous matrices are now used for high powered lasers.[62,63] Further, this kind of coating improves wetting and dispersion that are critical to photocatalytic activity.[64]

The synthesis of quantum dots embedded in amorphous matrices suffer from the inherent challenge of high activation energy because of the composition and solubility of the semiconducting particles in the glass matrix. In fact, Xue et al claim that only the semiconductor QDs of group II-VI, IV-VI elements and perovskite QDs have been reported to be embedded in glassy matrices, in their 2020 review.[39] Out of all the materials explored in this thesis, only ZnO falls under these groups listed by Xue et al indicating just how rare and unexplored this approach is in metal oxide semiconducting quantum dots. Further, quantum dots embedded in amorphous matrices intended for photocatalytic applications must avoid hermetically sealing the semiconducting material in glass matrix as this will eliminate all surface reactions.[65] On the other hand, co-mixing the semiconducting material with the glass matrix leads to segregated particles exhibiting high photocatalytic activity.[65] Note that Cai et al. reported SnO_2/SiO_2 particles with SnO_2 crystal sizes of 6-8 nm (SnO_2 Bohr diameter is 5.8 nm[43]), but did not refer to those particles as “quantum dots”.

On the other hand, the need for viable high-volume production of quantum dots remains unmet. Quantum dots are usually synthesized using wet chemistry techniques that are relatively complex, require hours, and with a production rate in the order of grams per day.[39,42,43,44,48,49,66,67,68] I outline how I contribute to addressing this challenge in chapter 5.

Finally, I am interested in using quantum dots as photocatalysts for epoxy polymerization because semiconducting nanoparticles are good oxidizers. The principles of oxidation and reduction[13] via semiconductors were implemented when Fujishima and Honda first demonstrated the splitting of water with solar light using a semiconducting plate.[57] In this application, the water is oxidized by the photo-generated holes, to generate O_2, and protons which are reduced by the photo-generated electrons to form H_2 gas. Semiconductors are also able to oxidize alcohols to ketones, and produce protons.[24,69] Equations 5 and 6[24] show a typical alcohol oxidation reaction by a semiconducting material producing protons as described by Hoffman et al.[24]

$$\mathrm{ZnO} + \mathrm{h\nu} \rightarrow \mathrm{h_{vb}}^{+} + \mathrm{e_{cb}}^{-} \qquad [5]$$

$$\mathrm{ROH} + \mathrm{h_{vb}}^{+} \rightarrow \mathrm{ROH}^{*} + \mathrm{H}^{+} \qquad [6]$$

Equations 5 and 6 are reproduced from ref 24.

There is a wide variety of standard applicable metal oxide semiconducting nanoparticles with a range of band gap energies that include visible or deep UV regions such as copper oxide and tin oxide, respectively. Therefore, semiconducting nanoparticles are a tunable, cheaper, less toxic, and easier to synthesize alternative to the current commercial cationic organic initiators.

2.3. Flame spray pyrolysis (FSP)

Flame aerosol is a technology used to make fine particles since prehistoric times per cave wall paintings[70], and that constitutes a $15 billion industry in 2010[71]. Carbon Black is produced via flame to the tune of 15 million tons/year in 2021.[72] The applications of flame-made particles are as broad as the applications of nano- and microparticles technology. The number of academic publications on nanotechnology has been steadily increasing from ~700 publications in 1997 to over 25,000 publications in 2020, according to a simple search on "Web of Knowledge" for the word "nano". This includes gas sensing[73], nanomedicine[74], catalysis[16], and climate[75]. FSP-related studies have been playing an increasing role in nanotechnology. The number of FSP-related publications has also been increasing steadily from 5 publications in 1996 to 89 publications in 2020 according to a simple search on "Web of Knowledge" for "flame spray pyrolysis".

Figure 2-3 shows the basic steps of particle synthesis in flame. Generally, a precursor material with the desired inorganic elements is injected into a burner and dispersed through a flame using a dispersion gas.[76] The precursor could be in the gas form from the beginning.[76] Alternatively, the precursor could be in the form of droplets or solid particles that evaporate into gas given the flame's high temperature.[76] The vapors react forming oxide molecules: carbons become CO_2, hydrogens H_2O, and metal elements metal oxides.[76] The high flame temperature combined with an abundance of oxygen minimizes soot formation. The metal oxide molecules collide in the flame to form clusters and then nano and/or micro-particles.[76]

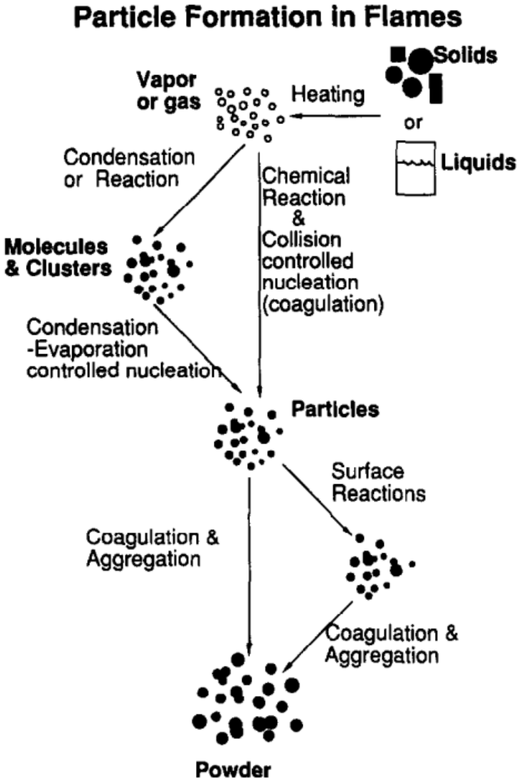

Figure 2-3: Particle flame synthesis. From ref 76.

First, primary particles form via nucleation and grow via full coalescence if the rate of sintering is faster than that of collisions.[76] Coalescence is the same process through which two raindrops become one bigger raindrop. Hard agglomerates (aggregates) form via strong chemical bonds (sintering or fusion) between primary particles in the high temperature region of the flame if the rate of sintering is faster than that of collisions.[76] The end of full coalescence is the onset of sintered hard agglomerates formation due to partial (incomplete) coalescence.[77,78] Soft agglomerates form via weak physical bonds between particles as the flame gets colder.[76] The end of sintering is the onset of soft agglomerates formation. Precursors containing different inorganic elements could be mixed to produce multi-element particles.[79] Alternatively, a multistage FSP-setup consisting of "rings" can be used to produce multi-element particles with a core-shell structure.[65] Hard agglomerates are useful as fillers (e.g., for car tires) while soft agglomerates are useful as pigments.[77] The agglomeration size and strength govern the viscosity of suspended particles, and the breakage of soft agglomerates could lead to shear thinning or thixotropic behavior.[78,80] The inherent difficulty of producing unagglomerated particles is a disadvantage of flame synthesis.[76]

Particle properties including crystal and particle size, and crystal structure are governed by the time the particles spend at high temperature. This high temperature residence time (<1 s, ref 77) is affected by a few inter-related factors: 1) the flame temperature governed by the enthalpy and concentration of the combusting precursor mixture, 2) the flame height that is inversely proportional to the amount of oxygen available to accelerate the oxidation process, and 3) the particles travel speed through the flame controlled by the dispersion gas flow rate.[79]

The longer the particles spend at the high temperature region of the flame, the more they grow, the larger their crystal and particle size, the smaller their specific surface area. With respect to crystallization, the time for crystal formation is limited to high temperatures and is of the scale of 1 ms.[81] This high temperature particle residence time is the key scalability design parameter as it has been demonstrated that production rate can be increased (up to 500 g/h) while preserving properties by keeping that time constant.[82] Production rate is a function of precursor flow rate.[82] The faster the precursor flow rate, the higher the production rate because there is simply more material going through the flame.[82] However, increasing the precursor flow rate increases the flame temperature and height.[82] It turns out that the high temperature residence time can be kept constant at various production rates by simply keeping constant the ratio between the precursor flow rate, in mL/min, and the dispersion gas flow rate, in L/min.[82] Therefore, flame conditions are conventionally referred to as the ratio between those two flow rates. A "1/5 flame", for example, means that the precursor flow rate is 1 mL/min, while the dispersion gas flow rate is 5 L/min. This simplicity in scaling up the production of particles synthesized at lab scale with specific properties significantly shortens the development time and investment in transferring lab-level research to industrially viable commercial technology. Figure 2-4 shows how the specific surface area remains constant as production rate is scaled up when the ratio between the precursor and the dispersion gas is kept constant.[83]

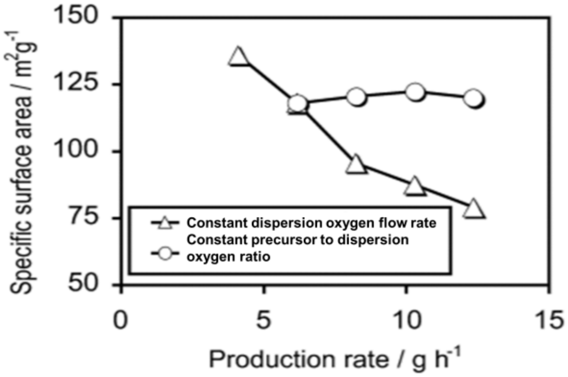

Figure 2-4: Specific surface area of Pt/Al_2O_3 as a function of production rate. Adapted from ref 83.

Other parameters include the choice of dispersion gas between, for example, oxygen, air, nitrogen and argon. The dispersion gas choice can impact whether the flame environment is oxidizing or reducing, and the rates of oxidation, combustion and cooling. A quartz tube can also be used to surround the flame to prevent air entrainment which controls the oxidation, combustion and cooling rates, making the flame hotter and longer. In the case of liquid precursors, flammable organic solvents are used in the mixture to provide self-sustaining flames.[79] The combination choice of this solvent and precursor is important due to their associated enthalpy, and its dictation of the pre-processing stability. Teoh et al.[71] tabulated a list of suitable precursor/solvent combinations for 45 elements.

The flame industry produces millions of metric tons of particles annually.[79] Flame aerosol technologies span various reactor setups such as diffusion flame, and spray pyrolysis.[79] However, it is difficult to use diffusion flames to make homogeneous multi-element particles due to the differences in vapor pressure of the precursors of different elements.[84]

In this thesis, I exclusively use flame spray pyrolysis of liquid precursors. Flame spray pyrolysis (FSP) is a one step process with no moving parts that produces metal oxide nanoparticles at industrial rates in the order of tons per day and can easily make multicomponent nanoparicles.[85] I note here that the "German National Science Foundation (DFG) named FSP a priority technology supporting over 30 PhDs, and, in 2016, the US National Institute of Health (NIH) awarded Harvard a 5-year, $5 million, grant to use the FSP to create a database mapping the toxicity of various nanoparticles. The Argonne National Laboratory in the United States is using artificial intelligence to assist in discovering new materials using FSP.[86] A multitude of spinoffs valued in the order of $100s million exist today based on FSP.[87]

Figure 2-5 shows a picture of the FSP setup at Concordia University. A typical flame spray pyrolysis reactor consists of a system that disperses liquid droplets, a pilot flame to serve as the initial heat and ignition source, and an oxidant for combustion (Figure 2-6).[79] The particles are collected on a glass-fiber filter on top of the flame (Figure 2-7), as the particles directed towards the filter using a vacuum pump.

Figure 2-5: FSP setup at Concordia University- first in Canada.

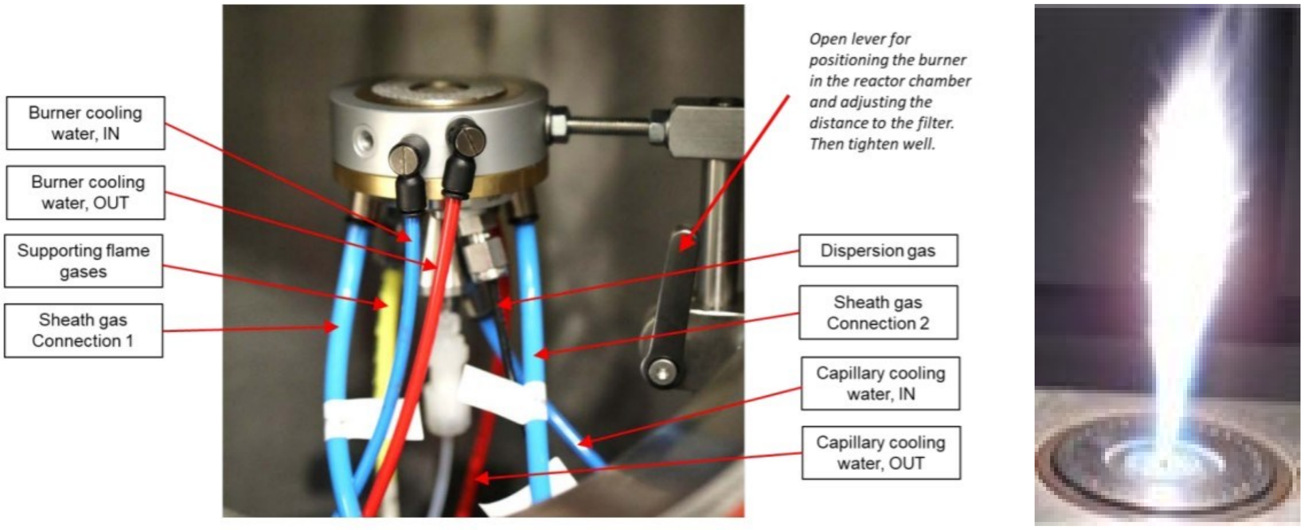

Open lever for positioning the burner in the reactor chamber and adjusting the distance to the filter. Then tighten well.

(a) (b)

Figure 2-6: a) a picture of the burner and tubes carrying the various gases and the cooling water. b) a picture of the flame during operation.

Figure 2-7: A picture of nanoparticles collected on the sample filter, synthesized on Halloween.

As discussed, various FSP process parameters can be used to control particle size such as the dispersion gas and/or precursor flow rates. However, precise control of the very small crystal size required to synthesize quantum dots remains elusive. Teleki et al[88] observed the blue shift in band gap energy that is characteristic of the quantized effect in titania that is collected at different heights from within the flame. Even though, the final product in that paper is in bulk size, it demonstrates that quantum dots exist at early stages of flame synthesis.[88] Prior to this work, there exists only one study demonstrating the ability of FSP to synthesize ZnO particles small enough to exhibit the quantized effect.[89] In that study, Mädler et al. added silica to the precursor mixture to provide a matrix that caps the size of ZnO crystals and provide access to smaller crystal size and narrower size distribution.[89] The coprecipitation of ZnO and silica hinders the sintering of ZnO or its coalescence and eventually growth.[89]

2.4. The self-assembly of graphene oxide liquid crystals

The discovery of graphene by Nobel laureate Novoselov[90] et al triggered a frenzy of research, and excitement due to its extraordinary properties: physical, mechanical, and electrical. This two-dimensional, one-atom-thin material exhibits a Young's modulus of 1 TPa, and a tensile strength of 130 GPa.[15] Such properties make it the strongest material known but translating them to a macroscopic scale remains a challenge.

Griffith[14] demonstrated that the strength of a material fundamentally depends on its structure, and not merely on the intrinsic strength of chemical bonds. He observed that polished samples are significantly stronger than non-polished ones, and that even micro-sized scratches are profoundly detrimental. The ideal structure of graphene provides its phenomenal strength. It follows that such an ideal structure can be a building block towards superior macroscopic structures. Numerous comprehensive reviews of a wealth of work on graphene nanocomposites are available.[91,92,93,94] However, the self-assembly of those sheets might be the path towards superior macroscopic structures.

Self-assembly is the organization of building blocks into nanostructures such as micelles and liquid crystals even in the absence of external forces.[95] A liquid crystal is a subset of self-assembled nanostructures that has a liquid-like nature and a crystal-like order.[96] Amphiphilic particles have been shown to spontaneously self-assemble under certain conditions. Amphiphilic particles (e.g. graphene oxide) are characterized by having both solvophobic (e.g. hydrophobic in water) and solvophilic (e.g. hydrophilic in water) groups.[95] Essentially, cluster formation is driven by the force generated when the solvation free energy of clusters is lower than the sum of the solvation free energies of the individual solutes.[97] This differential in the solvation free energy can exist when there is a large enough number of amphiphilic solutes (i.e. high volume to surface ratio). For amphiphilic solutes to self-assemble, this solvophobic force must be higher than the electrostatic repulsion between the solutes.[98]

It is important to differentiate between clustering and clustering *in an ordered state*. When the solvophobic force is stronger than the electrostatic repulsion, solutes will cluster. When there is *also* substantial electrostatic repulsion, these clustered solutes will self-assemble into an ordered state. In summary, two conditions must be met for self-assembly to take place: 1) some degree of electrostatic repulsion, and 2) a solvophobic force that is stronger than the electrostatic repulsion.

A critical trigger for the advances in graphene-related research is the achievement of Li[99] et al to disperse chemically converted graphene in water without the use of any dispersing agents. The challenge stems from the hydrophobicity of graphene's hydrocarbon sheet. The carbonyl groups on the edges of graphene oxide have negative charges leading to electrostatic repulsion that enables graphene oxide to become amphiphilic, and disperse in water without the need of additional dispersing agents. Further, the ability of the oxygen containing functional groups to form hydrogen bonds with solvents such as water enables it to "dissolve" in a stable solution.[100] GO solutions can be engineered to exhibit a wide range of rheological properties by simply varying the GO concentration. Such versatility originates in GO dispersion ability to form ordered states (often referred to as "liquid crystals") which is raising the prospects of exciting opportunities for the use of manufacturing techniques that requires specific viscoelastic properties as shown in Figure 2-8. Spray technologies require viscoelastic liquid, while printing and spinning technologies require more solid/gel like viscoelasticity.[101] Fundamentally, harnessing the chemistry of graphene oxide is key to any advances in both composites, and liquid crystals.[102]

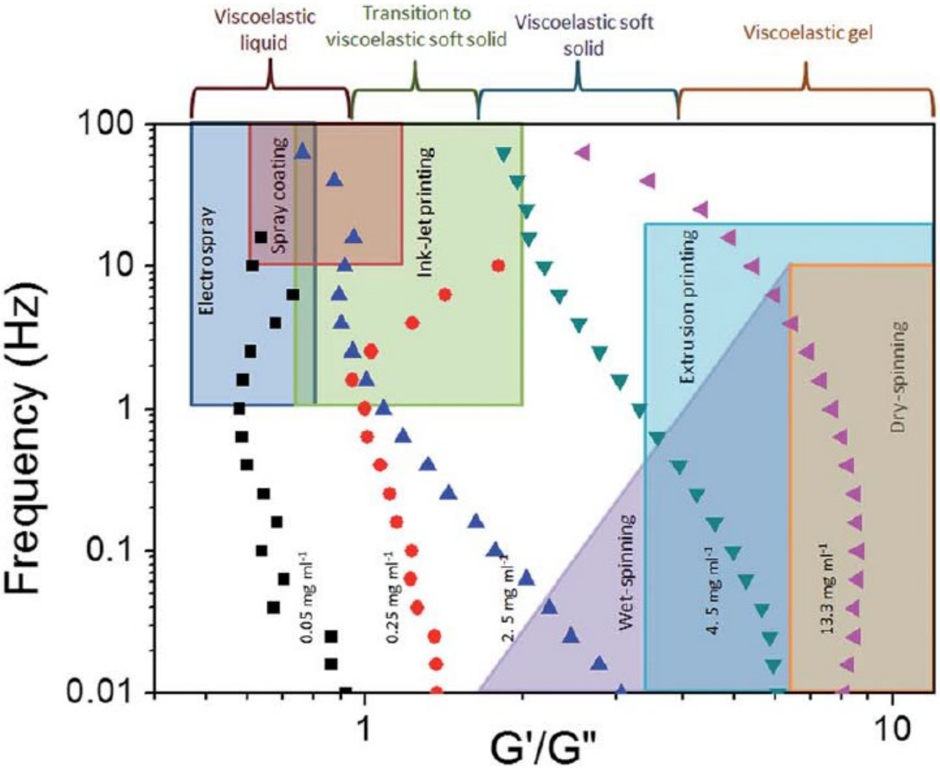

Figure 2-8: The various manufacturing processes enabled by the range of G`/G`` of graphene oxide dispersions. Concentrations are described in mg of GO per mL of water. From ref 101.

The process of self-assembly starts with isotropic, amphiphilic graphene oxide sheets that interact so that they stack to produce lyotropic liquid crystals with "nematic"[103], "columnar"[101], or "chiral"[103] liquid phases. Such interactions, reviewed by Pan[104] et al and by Zhang[105] et al, include covalent bonding, and non-covalent bonding. Non-covalent bonding includes hydrogen bonding, ionic bonds, and Π- Π interactions. Those interactions can co-exist in the same system.

This self-assembly process leads to various kinds of macroscopic structures as reviewed by Wu[106] et al such as paper and fibers. These solid structures are prepared using several methods including wet-spinning, freeze drying and filtration, that preserve the ordered structure observed in the liquid crystal phase. The highest tensile strength achieved in graphene fiber is 1,450 MPa (Table 2).[107] Graphene fibers show the most promise from a strength perspective, and have numerous applications: actuators, motors, dye-sensitized photovoltaic wires, and supercapacitors, as reviewed by Cheng[108] et al.

Table 2: Properties summary of self-assembled GO achieved in the literature

Reference	**Structure**	**Preparation method**	**Tensile strength (MPa)**	**Young's modulus (GPa)**
Ultrastiff and strong graphene fibers via full-scale synergetic defect engineering (Xu et al, Advanced Materials)[107]	Fibers	Wet-spinning + heating @ 3000 °C	1450	282
Highly thermally conductive and mechanically strong graphene fibers (Xin et al, Science)[109]	Fibers	Wet- spinning + heating @ 1300 – 2800 °C	1080	135
Ultrastrong bioinspired graphene-based fibers via synergistic toughening (Zhang et al , Advanced Materials)[110]	Fibers	Wet-spinning + heating @ 160 °C	842.6	Not reported
Mechanical reinforcement fibers produced by gel-spinning of poly-acrylic acid (PAA) and graphene oxide (GO) composites (Jiang et al, Nanoscale)[111]	Fibers	Wet-spinning + heating @ 60C	764.5	59.2
Liquid crystal self-templating approach to ultra strong and tough biomimic composites (Hu et al, Scientific Reports)[112]	Fibers	Wet-spinning + heating @ 90C	652	20.9
Ultra strong fibers assembled from Giant Graphene Oxide Sheets (Xu et al, Advanced materials)[113]	Fibers	Wet-spinning	501.5	11.2
Toward high performance graphene fibers (Chen et al, Nanoscale)[114]	Fibers	Wet-spinning	360.1	12.8
Preparation and characterization of graphene oxide papers (Dikin et al, Nature)[115]	paper	directional flow, vacuum filtration	120	32

Briefly[116], the restructuring of particles in solution is governed by the free energy of aggregates, ΔG°_{agg} as described in Equation 7.

$$\Delta G^{\circ}_{agg} = \Delta H^{\circ}_{agg} - T\Delta S^{\circ}_{agg} \qquad [7]$$

Where $\Delta H^{\circ}{}_{agg}$ is the aggregate's enthalpy and is negligible[97] at ambient conditions, and $\Delta S^{\circ}{}_{agg}$ is the aggregate's entropy. Clearly, self-assembly is entropy driven at ambient conditions. For charged amphiphilic particles such as graphene Oxide, $\Delta G^{\circ}{}_{agg}$ is the sum of the contribution from hydrophobicity, $\Delta G^{\circ}{}_{hc}$, and electrostatic repulsion, $\Delta G^{\circ}{}_{el}$, as per Equation 8. When the $\Delta G^{\circ}{}_{hc}$ is larger than $\Delta G^{\circ}{}_{el}$, aggregates (clusters) self-assemble. Note that both $\Delta G^{\circ}{}_{hc}$ and $\Delta G^{\circ}{}_{el}$ can be written in terms of enthalpy and entropy as per Equation 7. In the conditions where enthalpy is negligible, Equation 8 can be completely written in terms of entropy.

$$\Delta G^{\circ}{}_{agg} = \Delta G^{\circ}{}_{hc} + \Delta G^{\circ}{}_{el} \qquad [8]$$

The theoretical foundation for graphene oxide liquid crystals is in the hard platelets' theory of Nobel laureate, Onsager[117]. He remarked that effective van der Waal's co-volume cannot alone account for the formation of two phases in some colloidal solutions, and finally concluded that electrostatic repulsion between highly anisometric particles drives this behavior. Onsager's remarks agree with similar ones made by another Nobel laureate, Irving Langmuir[118], who first observed liquid crystal phases in clays, and proposed to approach analysis from osmotic pressure point of view as opposed to just potential energy. Onsager obliged, and further explained that the transition from the isotropic to the nematic phase of graphene oxide is governed by entropy. In completely rigid rods, considered by Onsager, there exist two competing drivers of entropy: orientational preferring isotropic arrangement, and positional preferring an anisotropic arrangement. As the concentration of those rods increase, orientational entropy decreases, while the volume exclude by the additional concentration increases positional entropy more. This net increase in entropy compels self-assembly as concluded from free energy calculations. In other words, the net increase in positional entropy compels those rods to stack in parallel to one another so that they can pack within the available space. Two critical concentrations of colloids exist: the first is the limit below which a purely isotropic phase exists, the second is the minimum above which a purely anisotropic phase exists. Both phases coexist in varying fractions between the two concentrations.

Think of paper clips in a box. If only a few are inside the box, they will randomly orient. However, as you add more clips, there will be a point beyond which no more clips can be added without the clips reorienting into an ordered state. Graphene oxide sheets, and most colloids for this matter, behave similarly. If those clips are charged or larger, then the critical number of clips above which ordering occurs will decrease. If the repulsive forces between the charged clips are so strong that they break the box (hydrophobicity) they are in, the clips will be randomly oriented. If these clips are flexible, then the number of clips needed to compel ordering will increase.

Onsager only considered completely rigid rods while graphene oxide sheets are flexible. Nobel laureate, Flory[119], first challenged the assumption that random entanglement of chains is normal for polymer, which he viewed as lacking critical assessment. He demonstrated that even for polymers, there are concentrations where parallel ordered structuring avoids the competition for a given lattice sites minimizing free energy. This should not be surprising given that polymer crystallization is not uncommon. Khokhlov and Semenov[120] expanded the theory to accommodate flexible to stiff polymers. Electrostatic interactions, and steric hindrance still drive positional entropy by virtue of their impact on excluded volume. On the other hand, the added flexibility considered in the Khokholov theory increases the magnitude of orientational entropy lost, as in the case of flexible graphene compared to completely rigid rods. This increase in entropy cost is because one needs not only to assign a one-point orientation of an effective segment, but also the tangential vector of all other points in the segment due to the flexibility of the colloid chain. This raises the critical colloidal concentration required to form anisotropic self-assembled phases in graphene oxide liquid crystals. Jalili[121] et al later adapted this understanding to the case of graphene oxide self-assembly. Not considering the flexibility of graphene sheets has led to large discrepancies between experiments and predictions derived based on assumptions of rigidity in reports such as that of Aboutalebi[122] et al.

Behabtu[123] et al remarked that per Onsager's work, there must be a concertation above which an ordered state is formed in graphene oxide dispersion. Surely enough, they were the first to observe a phase separation where the bottom part exhibited an ordered phase at high graphene oxide concentration. Graphene oxide separates into two phases: ordered (the bottom), and disordered (the top) when its concentration is between the two limits. It is worthy of note that such phase separation phenomenon was Onsager's original motivation for his general theory.

Xu[103] and Gao demonstrated the presence nematic graphene oxide liquid crystals. A critical factor that allowed their discovery is their novel synthesis modification to increase the oxidation degree of their graphene oxide to enhance solubility. This change greatly strengthened the repulsive forces between the graphene oxide sheets as indicated by the higher zeta potential they measured, -64 mV, compared to that of graphene oxide synthesized by the Hummer's method[124], -30 mV. The negative charge indicates strong electrostatic repulsive forces. This repulsion allows for the increase in excluded volume entropy necessary for the formation of graphene oxide liquid crystals, and leads to the enhanced solubility necessary to stabilize this colloidal system as indicated by the higher absolute value of the zeta potential.

The role of electrostatic repulsive forces can be further explored by taking advantage of the salt effect, the immediate coagulation of graphene oxide dispersion upon the addition of an electrolyte solution such as sodium chloride (NaCl).[99] The addition of NaCl weakens the repulsive forces between the graphene sheets proportionally to its concentration as illustrated by Zeta potential measurements shown in Figure 2-9b. As the concentration NaCl increases, the absolute value of the Zeta potential decreases indicating a corresponding decrease in the electrostatic repulsive forces and solubility, compelling coagulation into disordered solids (referred to as gelation in some papers[125]).

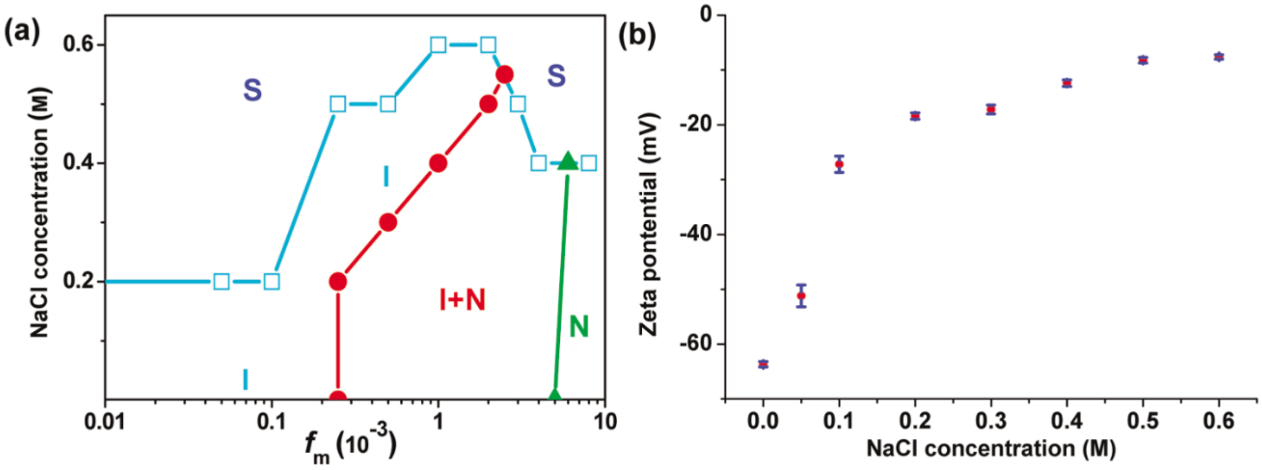

Figure 2-9: a) a phase diagram of the phases involved as a function of graphene oxide, and NaCl concentrations. b) Zeta potential versus NaCl concentration demonstrating the salt effect. S= Solid (coagulated); I=Isotropic (disordered); N=Nematic (ordered). From ref 103.

As shown in Figure 2-9a, the increase of graphene oxide concentration, f(m), increases steric hindrance increasing positional entropy, and therefore prompts the formation of a nematic phase that coexists with the isotropic phase in the intermediate range, and that exists in a pure state in the high range. The addition of salt decreases the electrostatic repulsive forces, decreasing excluded volume entropy. Therefore, the addition of salt resists the formation of nematic liquid crystals, and forms coagulated solids instead, above critical concentrations. Similarly, an acidic environment protonates the carboxylic groups, reducing the electrostatic repulsive forces and the absolute value of the zeta potential.[99]

Oh[126] et al investigated the effect of increasing the degree of oxidation on the critical concentration necessary to achieve pure nematic graphene oxide liquid crystals. The degree of oxidation is synonymous with the concentration of oxygen containing functional groups including the carbonyl groups responsible for the negative charge of graphene oxide. As the degree of oxidation increases, the critical concentration necessary to reach 100% nematic phase decreases, as shown in Figure 2-10. The authors attribute this observation to the increased hydrogen bonding, and we should also note that the additional carbonyl groups due to increased oxidation also increase the electrostatic repulsion as shown in Figure 2-11. The increased electrostatic repulsion also aids the self-assembly process, and decreases the critical concentration in question. Interestingly, the zeta potential in the nematic phase is more negative than the isotropic counterpart. While the authors expressed surprise at such an observation, it should have been predictable given the vital role electrostatic repulsion plays in the formation graphene oxide liquid crystals as per the theories outlined earlier.

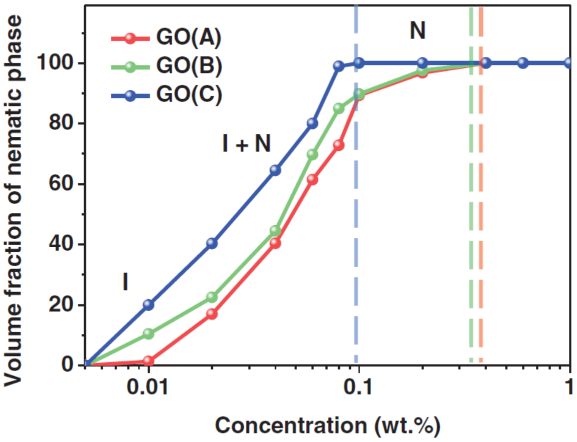

Figure 2-10: Effect of the degree of oxidation on the isotropic-nematic transition concentration. As the degree of oxidation increases (from GO A to GO C), the critical concentration decreases. I=Isotropic (disordered); N=Nematic (ordered). From ref 126.

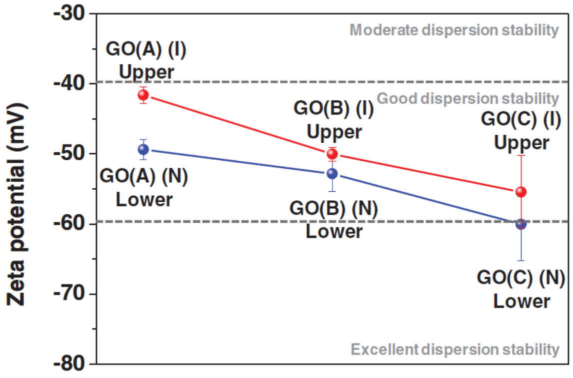

Figure 2-11: Effect of oxidation degree on the zeta potential of graphene oxide dispersions in both the nematic phase (lower), and the isotropic phase (upper). As the degree of oxidation increases, from GO (A) to GO (C), the negative charge increases (more in the nematic phase compared to the isotropic phase.I=Isotropic (disordered); N=Nematic (ordered). From 126.

Van der Beek and Lekkerkerker[127]developed an equation to predict colloidal volume fraction required for the isotropic-nematic transition (Equation 9) for charged colloidal platelets.

$$\emptyset_{pol} = \frac{3}{8}\sqrt{3}\frac{L}{D}\frac{1+\sigma_D{}^2}{1+3\sigma_D{}^2}\rho < D^3 > \qquad [9]$$

Where D is the average lateral size, σ_D is the polydispersity, L is the thickness, and ρ is a function of D^3, and is a dimensionless number density. While the authors acknowledge that electrostatic forces are crucial, they argue that only number densities are needed. Jalili[121] et al successfully uses this equation to provide indications in their study of the effect of graphene oxide size, even though it is developed for hard platelets and should be corrected to account for flexibility by using effective thickness and size.[127] Whether corrections are used for accurate numerical predictions or not, clearly the size magnitude and polydispersity of graphene oxide sheets have a direct influence.

The positional entropy is driven by the volume excluded and made inaccessible due to the presence of a given molecule.[97] Consequently, the size of graphene oxide sheets involved directly affects the magnitude of excluded volume entropy. Aboutalebi[122] et al eliminated the ultrasonication involved in the synthesis of graphene oxide, reducing the breakage of the sheets, and resulting in ultra large graphene oxide sheets. The graphene oxide sheets produced in this study has a size in the order of 10s of micrometers, and areas up to 10,000 μm^2. The resulting increase in excluded volume entropy due to the use of such large sheets reduced the critical graphene oxide concentration necessary to the spontaneous formation liquid crystals to lowest levels achieved at the time for any colloid system, 0.1 wt%. The effect of size on the critical graphene oxide weight fraction is best seen in the work of Kim[96] et al as shown in Figure 2-12. As the size of graphene oxide sheets decreases (Figure 2-12a) from A to B to C, the critical weight fraction of graphene oxide necessary to achieve a pure nematic phase increases (Figure 2-12b).

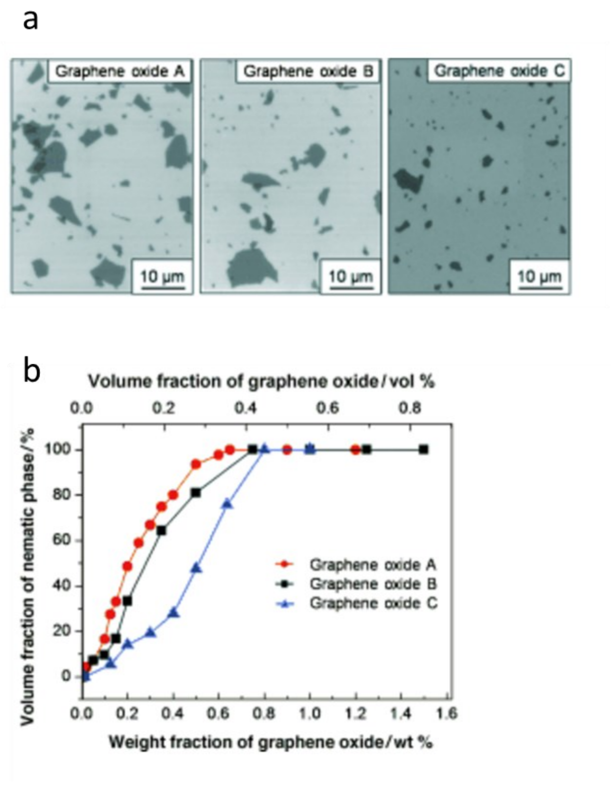

Figure 2-12: Effect of size on the graphene oxide critical concentration for liquid-nematic transition. As size of graphene oxide sheets decreases (from A to B to C), the weight fraction of graphene oxide necessary to achieve 100% nematic phase increases. Adapted from ref 96.

Jalili[121] et al demonstrated that even very small graphene oxide sheets can be induced to exhibit a nematic phase if only 4 wt% of large graphene oxide sheets are added to enhance the polydispersity of the mixture. Figure 2-13 summarizes the previous discussion. Large and polydisperse graphene oxide still require a minimum concentration to form a nematic phase (Figure 2-13a). Small, and almost monodisperse, graphene oxide cannot exhibit a nematic phase even at large concentration (Figure 2-13b). Adding a small amount of large graphene oxide to small graphene oxide dramatically increases the polydispersity allowing for a nematic phase to be formed at modest concentrations (Figure 2-13c).

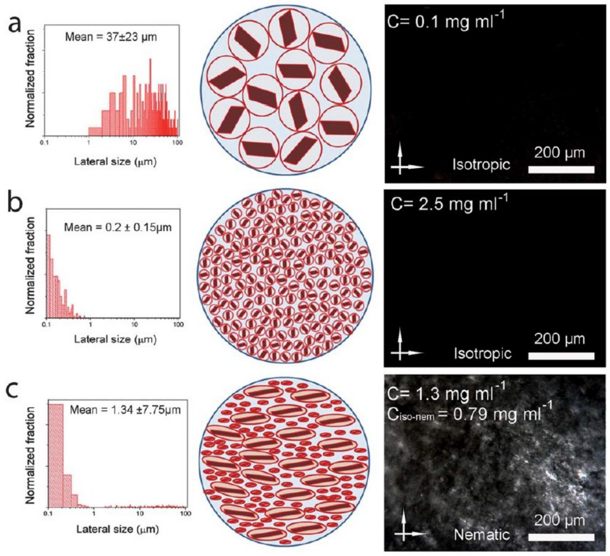

Figure 2-13: The effect of the magnitude and polydispersity of graphene oxide. a) isotropic phase of large, and polydisperse graphene oxide but at low concentration. b) isotropic phase of concentrated but small and almost monodisperse graphene oxide. c) nematic phase of concentrated, polydispersed but small graphene oxide. The images on the right are Polarized Light Microscopy. From ref 121.

Several experimental techniques are used to determine if an anisotropic state exists such as Polarized Light Microscopy (POM) and SEM. POM is used on liquid GO dispersions, while SEM is used on solid samples created after processes such as filtration and freeze drying.

The interaction of the anisotropic graphene oxide phase with light is mesmerizing. As Tkacz[128] explains that such graphene oxide phase exhibits birefringence, first observed by Langmuir[118], where light travels at different velocities depending on the direction it goes through the material. Light slows down if its polarization axis is parallel to the graphene oxide plane. These properties allow the use of polarized light microscopy to determine whether an ordered state exists or not, and quantify its fraction. Figure 2-14 shows graphene oxide dispersion of different concentrations. The volume fraction of the birefringent phase is a measure of the fraction of the nematic phase plotted in Figure 2-10 and Figure 2-12.

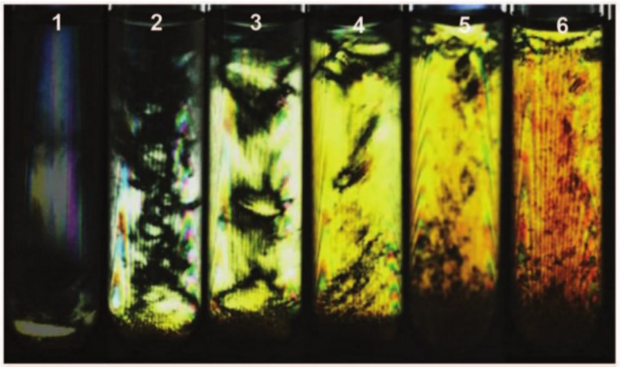

Figure 2-14: Polarized Light Microscopy of graphene oxide dispersion. The birefringent areas have a nematic ordering, while the darker regions are isotropic. 1) 0.01 wt%, 2) 0.02 wt%, 3) 0.04, 4) 0.06, 5) 0.08, 6) 0.1 wt%. From ref 126.

Figure 2-15 shows SEM images directly showing the self-assembly of graphene oxide sheets to an ordered state where they are parallel to one another. Figure 2-15a shows a flat graphene paper[115] where the graphene oxide sheets could have just as well been rigid. Interestingly, Dikin[115] et al is likely the oldest report where graphene oxide self-assembly can be seen, even though they never referred to it as self-assembly or a liquid crystal. Hu[112] et al wet-spun graphene fibers, crosslinked with hyperbranched polyglycerol (HPG). Yet, despite the round shape of the fiber's cross-section magnifying the effect of graphene oxide flexibility, SEM still demonstrates self-assembly into an ordered state as seen in Figure 2-15b.

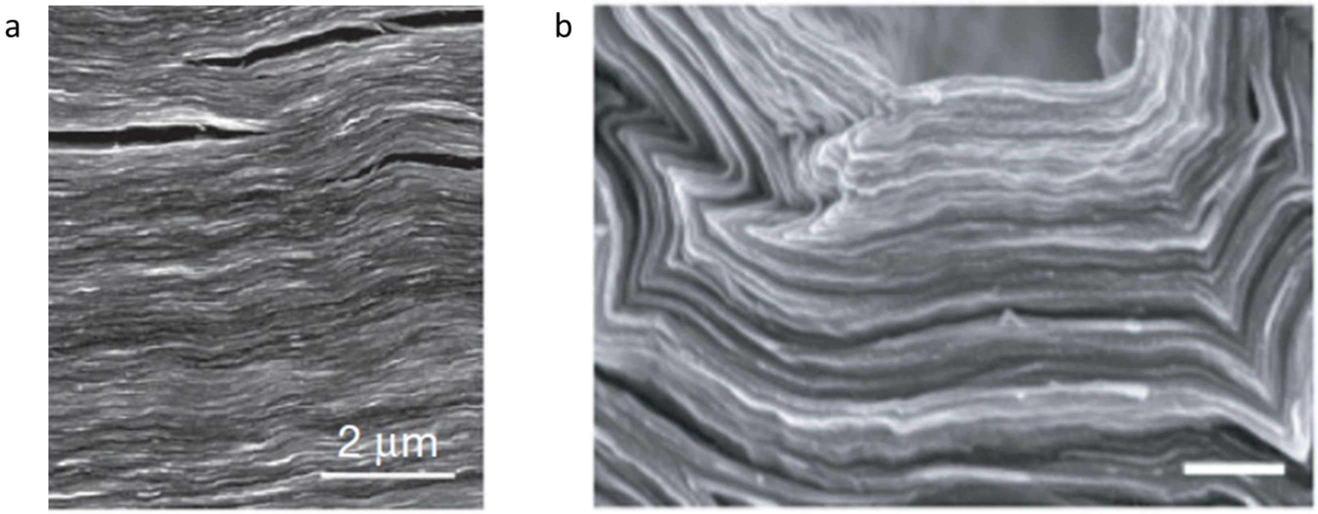

Figure 2-15: SEM images of self assembled graphene oxide. a) graphene oxide paper from ref 115. b) wet-spun graphene oxide fibers with a scale of 250 nm. From ref 112.

All the discussion thus far has been limited to aqueous dispersions, however Jalili[129] et al reported that it is also possible for graphene oxide to form liquid crystals in organic solvents (Figure 2-16). The magnitude of the electrostatic repulsion forces is much lower in organic solvents than in water.[130] Greaves[131] et al suggests that amphiphile self-assembly, observed in many systems before graphene oxide, is predominantly driven by solvophobic forces in non-aqueous solvents (analogous to hydrophopic effects in water).

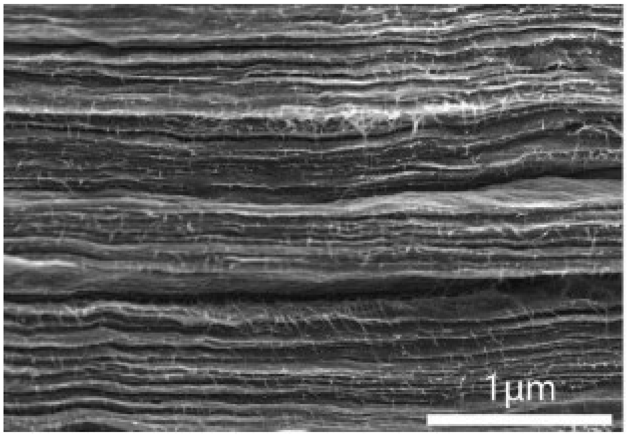

Figure 2-16: SEM of the fracture surface of free-standing paper of LC graphene oxide and single wall nanotubes made by cast drying. Adapted from ref 129.

Ray[97] explained that hydrophopic-like interactions are not limited to water but expand to non-aqueous solvents- solvophopicity. He observed that molecules of the solvents capable of forming micelles (self-assembled nanostructures of amphiphilic molecules such as detergents) have two or more centers for hydrogen bonds allowing for the formation of 3 dimensional solvent structures.[97,132] This solvophobicity is governed by solvent cohesiveness measured by the Gordon parameter[98], and the ability to form hydrogen bonds as measured by the Hansen parameter.[129] The process of liquid crystal self-assembly is obviously complex, and it is difficult to find consensus on the extent to which each factor contributes.

The evolution of our understanding of the self-assembly of the strongest known material into liquid crystals includes many giants who built on each other's work for nearly a century. Yet, the field is far from mature, and the most exciting opportunities remain ahead. Imagine now if we can make graphene oxide liquid crystals dispersed in alcohol, and then lock this superior macroscopic structure in place by strong covalent bonds instead of weak hydrogen bonds via photopolymerization. The alcohol is vital to allow the cationic photocuring with epoxide groups present in the basal planes of graphene oxide. Such photopolymerization will in turn enable the use of sterelithography 3D printing in making superior, mechanically strong, three dimensional structures of self-assembled graphene oxide liquid crystals. A downside to graphene oxide is the fact that it loses much of the electronic advantages that graphene has. However, those electronic properties could potentially be restored by reducing the 3D printed graphene oxide using hydrazine or heat (starting at 180 °C[129] all the way to 900 °C[133]).

3. Photo-polymerization using metal oxide semiconducting nanoparticles for epoxy-based coatings and patterned films

3.1. Abstract

Photo-polymerization is fundamental to many applications such as printed circuit board manufacturing, dentistry, coating, and stereolithography 3D-printing. However, the current organic cationic initiators are toxic, expensive and difficult to tune with respect to the wavelength of light required for the initiation of the photo-polymerization. Different applications require different wavelengths of light to initiate photo-polymerization. Thus, the ability to tune initiators is sought after. Here, we show that metal oxide semiconducting nanoparticles photo-polymerize epoxy via an oxidation reaction that we monitor using FTIR, NMR and titration techniques. Careful selection of metal oxide semiconducting materials with the desired band-gap energy controls the wavelength of light to which this class of epoxy photo-initiators respond. Additionally, those semiconducting nanoparticles are cheaper and less toxic relative to their commercial counterparts. Finally, semiconducting nanoparticles are standard materials with well-known syntheses offering a wide-range of readily available options. Our findings introduce a new class of epoxy photo-initiators that could impact industrial applications that rely on photo-polymerization, as well as nanocomposites where photo-induced reactions during use are undesirable.

3.2. Introduction

A vast array of high-impact applications that makes use of photopolymerization has been arising ever since Kodac developed the first synthetic photo-polymer, polyvinyl cinnamate, as a photoresist in printing plates.[19,20] These applications include the manufacturing of printed circuit boards, photocurable coatings, and stereolithography 3D printing.[19,21,22,23] The reason photopolymerization is catching so much attention is because it can be preferable to heat polymerization because it is less unpleasant relative to heat in dentistry applications, and requires low energy and no solvents.[19] However, controlling the critical wavelength required to trigger the photopolymerization reaction remains an area of needed research.

Photo-polymerization mechanisms are generally classified in two categories: free-radical and cationic.[10] In the former, free-radicals are produced during photo-initiation whereas in the latter, the initiator is photo-decomposed to generate cationic species and, ultimately, protons that ring-open reactive species such as epoxide groups.[11] The radical photo-initiation of acrylic monomers and resins has been extensively investigated using a variety of initiators including semiconducting nanoparticles.[24,25,12] In this work, we are interested in the photo-polymerization of epoxy, which requires a cationic initiator. Onium salts, first developed by Crivello[9], are the most commonly used cationic initiators.[10] Equations 1 ands 2 show an example of a cationic photopolymerization mechanism, described by Yagci et al.[10], where protons open up the epoxide rings and initiate polymerization[13]. The focus of most past studies of cationic initiators are on shifting the light wavelength to which the photo-initiator is sensitive.[10,31]

The principles of oxidation and reduction[69] via semiconductors were implemented when Fujishima and Honda first demonstrated the splitting of water with solar light using a semiconducting plate.[57] In this application, the water is oxidized by the photo-generated holes, to generate O_2, and protons which are reduced by the photo-generated electrons to form H_2 gas. Semiconductors are also able to oxidize alcohols to ketones, and produce protons.[69,25] Equations 5 and 6 show a typical alcohol oxidation reaction by a semiconducting material producing protons as described by Hoffman et al.[24]

Here, we demonstrate the ability of semiconducting nanoparticles to photo-polymerize epoxy. In our reaction, semiconducting nanoparticles oxidize alcohol and produce protons that then open epoxide rings and initiate polymerization (Figure 3-1). The electrons generated by exciting the semiconducting nanoparticles are scavenged by oxygen.[134] In fact, electron scavenging by oxygen is critical in the alcohol oxidation surface reactions of transition metals through chemisorption mechanisms.[135]

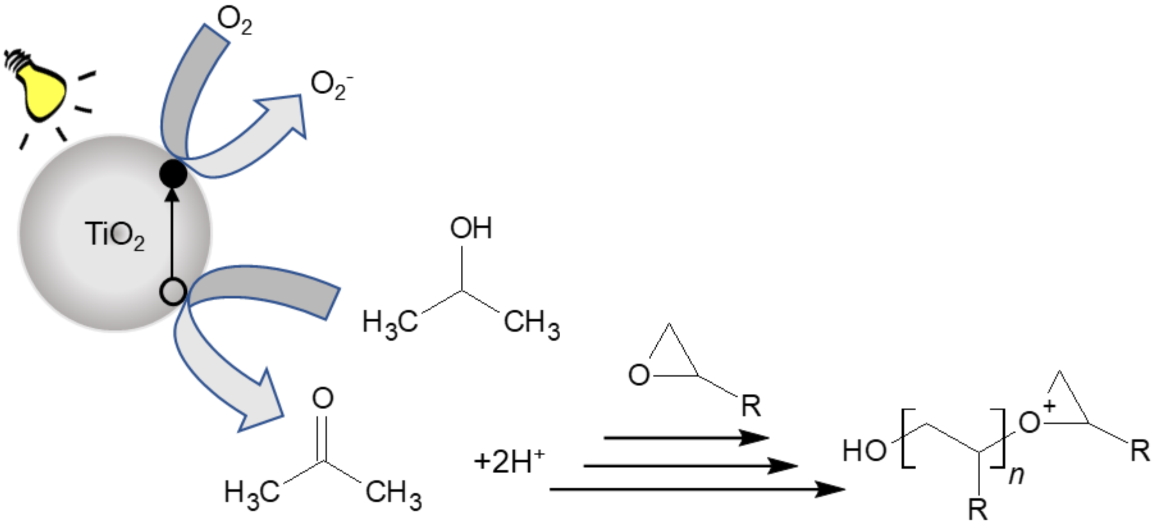

Figure 3-1: Proposed mechanism for the photo-polymerization of epoxy in the presence of isopropanol using semiconducting nanoparticles.

Semiconducting nanoparticles are a tunable, cheaper, less toxic, and easier to synthesize alternative to the current commercial cationic organic initiators. Chung et al demonstrated the versatility of semiconducting nanoparticles by creating PbS coated ZnO quantum dots exhibiting the highest certified efficiency of 8.55%, measured by recording current and voltage using a sourcemeter under simulated solar light illumination.[136] Such efficiency is achieved by band gab energy engineering where the energy levels are tuned in such a way where the excited electron is essentially blocked from recombining with the hole. There is a wide variety of standard applicable metal oxide semiconducting nanoparticles with a range of band gap energies that include visible or deep UV regions such as copper oxide and tin oxide, respectively. We focus on P25 TiO_2 in our work as it is among the best photo-catalysts available commercially[137]. We also use ZnO nanoparticles to generalize our conclusions. Both P25 TiO_2 and ZnO are standard materials with well-known synthesis processes and well investigated properties including quantum yields[138,139].

3.3. Experimental Section

3.3.1. Materials

The materials used for the experiments are epoxy monomers (1-4 cyclohexane dimethanol diglycidyl ether, mixture of cis and trans- technical grade), isopropanol (99.5%), xylene (reagent grade), 1-phenethyl alcohol (98%), methyl viologen dichloride hydrate (MV) (98%), commercial organic cationic initiator (bis (4-methylphenyl) iodonium hexafluorophosphate (98%)), P25 TiO_2 nanoparticles (25 nm, 50 m^2/g, anatase:rutile = 87:13), hydrogen bromide solution in acetic acid (33 wt%), toluene (99.8%), methanol (99.9%), 2-ethylhexanoic acid (2-EHA) (99%), and crystal violet indicator. These are obtained from Sigma Aldrich and used as-received. In some experiments, cyclohexene oxide (98%) is used as the epoxy monomer which is also obtained from Sigma Aldrich and used as received. Zinc 2-ethylhexanoate is obtained from Strem Chemicals and used as-obtained. Pure anatase TiO_2 (23 nm, 91 m^2/g) is purchased from mkNANO. ZnO nanoparticles are synthesized via flame spray pyrolysis using a 4/8 flame as described by Güntner et al.[140] The synthesized ZnO particles have a hexagonal zincite crystal structure with a crystal size of 29 nm (XRD), and a specific surface area of 39 m^2/g (Nitrogen adsorption).

3.3.2. Epoxy photo-polymerization

Mixtures (1.5 g) consisting of epoxy monomer, alcohol (isopropanol, 1-phenethyl alcohol), MV and nanoparticles (P25 TiO_2, ZnO) are stirred overnight and sonicated for 30 minutes with a

Misonix sonicator 3000 (5 seconds on, 20 seconds off). The exact compositions of the mixtures are specified in the results section. In some control samples, MV and/or nanoparticles are excluded. The mixtures are blade coated on microscope slides to make films that are radiated in a UVP (CL-1000L- 365 nm) photo-chamber with a light intensity of 4 mW/cm^2 at the surface of the samples. Figure 3-2 outlines this sample preparation procedure.

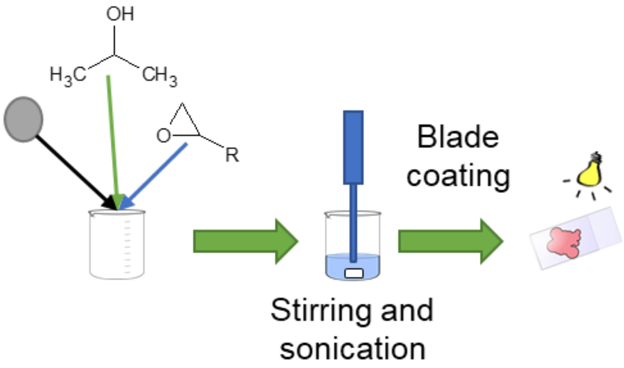

Figure 3-2: Sample preparation.

3.3.3. Reaction Monitoring

Liquid-state NMR experiments are done on cyclohexene oxide. Solid-state NMR experiments are done on samples initially consisting of monofunctional epoxy monomer, cyclohexene oxide, and isopropanol (5 wt%), polymerized by either a commercial organic cationic initiator or P25 TiO_2 (5 wt%) after 50 hours of UV radiation.

All spectra are recorded on a Bruker Avance III HD spectrometer operating at ^{13}C Larmor frequency of 150.87 MHz using a double resonance BBFO 5 mm probe for liquids and a Varian 3.2 mm BIO-MAS probe for solids. ^{13}C spectra of the soluble samples are acquired with NOE enhancement during the recycle delays. 16384 transients are added with 1 s acquisition time a spectral width of 234 ppm and a recycle delay of 2 s. The ^{13}C spectra of the solid samples are obtained at a Magic-Angle spinning frequency of 15 kHz using 1.5 ms cross-polarization at radio-frequency fields of 60 and 75 kHz for ^{1}H and ^{13}C respectively, a recycle delay of 5 s, an acquisition time of 20 ms during which high-power ^{1}H TPPM decoupling is applied at a radio-frequency field of 75 kHz. The spectral width is 300 ppm, and 8192 transients are accumulated.

The reaction is monitored using FTIR and titration. Fourier transform infrared (FTIR) spectroscopy (NEXUS in ATR mode) is conducted with 64 scans at 1 cm^{-1} resolution between 600 cm^{-1} and 4000 cm^{-1}. Titration is performed according to ASTM-D1652-97. During the titration, HBr solution (c = 0.5 mol/L) is used for data points with lower polymerization, and HBr solution (c = 0.06 mol/L) for the later points with higher degree of polymerization.

3.3.4. Nanoparticle Dispersion

An SEM investigation of the films is done once using a Quanta 200F (FEI, now: Thermo Fisher Scientific), operated in low vacuum mode (P(H2O) = 40 Pa) at an acceleration voltage U = 20 kV to ensure proper dispersion. Images are recorded with back-scattered electrons. Figure 3-3 shows SEM images of photo-polymerized films containing P25 TiO_2. Image analysis of the most agglomerated particles seen with SEM show an average agglomerated particle size to be 238 ± 10 nm. The largest agglomeration size observed is 254 nm. Sample size is 20 measurements of the largest agglomerations per image (total measurements = 40). The agglomerate particle size of P25 TiO_2 dispersed in water measured by DLS is about 350 nm. Thus, we assess that the P25 TiO_2 particles are well dispersed in our system.

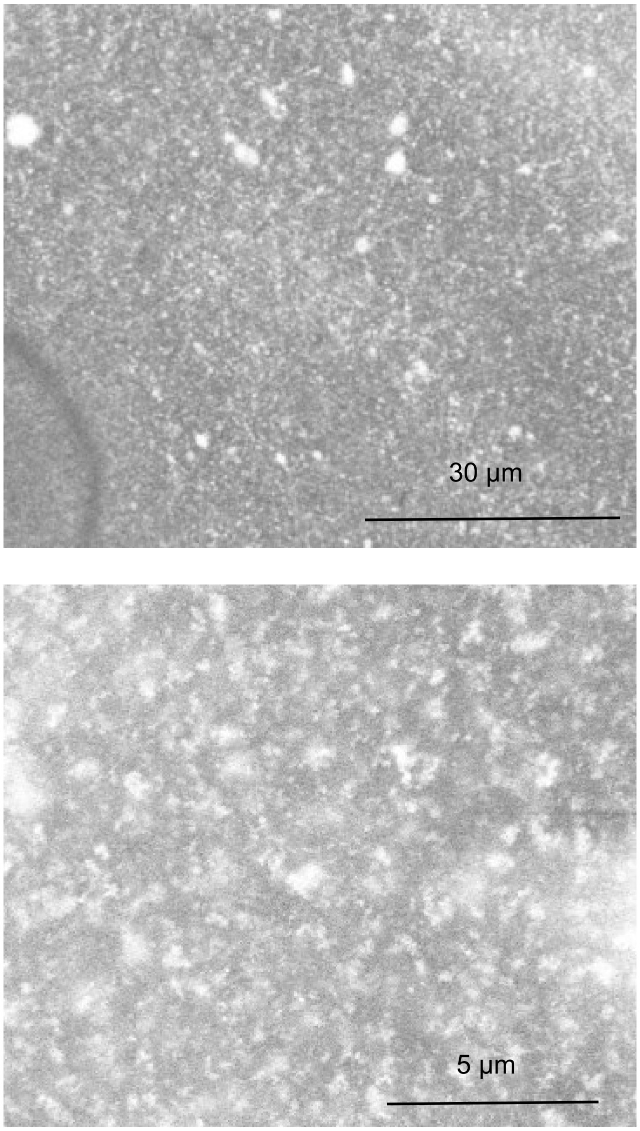

Figure 3-3: SEM images of a photo-polymerized film of a mixture containing epoxy, isopropanol (5 wt%), and P25 TiO2 (5 wt%). The film was irradiated for 150 hours. Image analysis demonstrates that the agglomerated particle size is 238 ± 10 nm. Maximum agglomeration size is 254 nm. Sample size is 20 measurements of the largest agglomerations per image (total measurements = 40).

3.4. Results and discussions

3.4.1. Polymerization Verification

Figure 3-4a shows liquid state ^{13}C NMR of the cyclohexene oxide monomer as received, showing a clear shift at 51.7 ppm that corresponds to epoxide rings. Figures 3b and c show solid state ^{13}C NMR of the polymerized cyclohexene oxide showing the methylene carbons at 20-33 ppm, and methine carbons at 68-90 ppm.[141] In general, the NMR spectra of the sample polymerized with the commercial cationic organic initiator (Figure 3-4b) and with the P25 TiO_2 (Figure 3-4c) have the same general shape indicating that the polymer synthesized using P25 TiO_2 is very similar to that synthesized using the commercial organic cationic initiator.

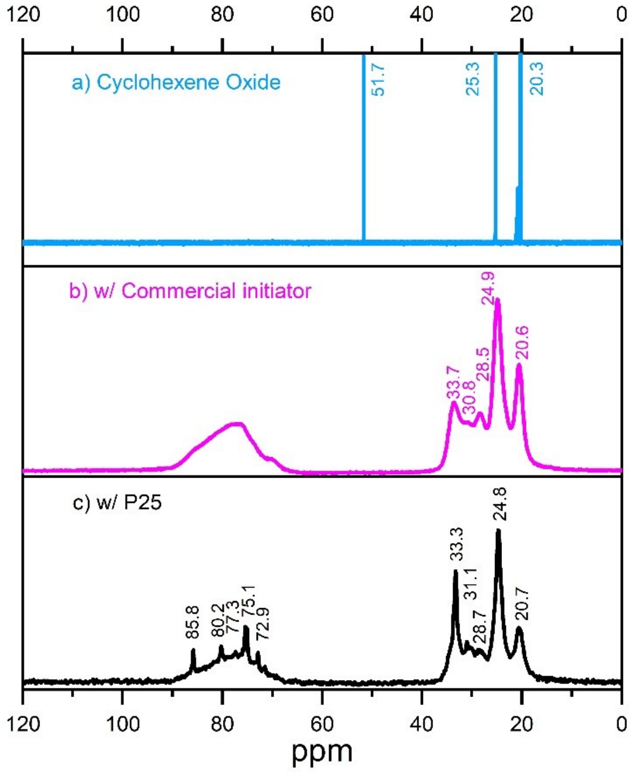

Figure 3-4: 13C NMR of a) cyclohexene oxide monomer (top, sky blue), b) sample cured with commercial cationic organic initiator (middle, magenta), and c) sample cured with P25 TiO2 (bottom, black).

The broad peak observed in Figure 3-4b between 70 and 90 ppm is the result of multiple overlapping peaks which cannot be resolved. The breadth of these peaks is most probably a consequence of the large molecular weight and low mobility of the species to which they are associated. This broad chemical shift distribution between 70 and 90 ppm is also observed in Figure 3-4c in addition to a few sharper chemical shifts at 72.9, 75.2, 80.2, 85.8 ppm. This indicates that the sample polymerized with P25 TiO_2 consists of two populations: a low mobility one with high molecular weight, and a high mobility population with low molecular weight. The presence of high mobility molecules in samples polymerized with P25 TiO_2 is further supported by our observation that it cross-polarizes less efficiently than the sample polymerized with the commercial cationic organic initiator.

We observe that the chemical shift at 51.7 ppm corresponding to the carbons in the epoxide ring disappears after radiation in Figure 3-4b and c in comparison with Figure 3-4a, confirming the epoxy consumption predicted by the proposed reaction mechanism in *Figure 3-1*. A chemical shift at ~175 ppm, corresponding to ketones, can be observed in the single pulse experiments (Figure 8-1) of the sample cured with P25 TiO_2. This peak at 175 ppm confirms ketone formation due to alcohol oxidation predicted by the proposed reaction mechanism in *Figure 3-1*.

3.4.2. Monitoring of Reaction Kinetics

We use FTIR spectroscopy to monitor photo-polymerization as is the convention.[13] In Figure 3-5 we show the effect of initiator presence/type and UV radiation exposure on the FTIR spectrum of the reaction mixtures.

The system does not polymerize in the absence of light, as shown by the identical spectra of samples before and after one month stored in the dark (Figure 3-5a and b). Further, the system does not polymerize in the absence of an initiator even after extensive radiation (Figure 3-5c). On the other hand, we observe polymerization in the presence of both light and semiconducting nanoparticles, P25 TiO_2 (Figure 3-5e) or ZnO (Figure 3-5f), evidenced by the decrease of the epoxide peak[142] at 910 cm^{-1}, consistent with C^{13} NMR observations (Figure 3-4c). We further observe a large peak at 1717 cm^{-1} in the systems photo-polymerized with semiconducting nanoparticles, P25 TiO_2 or ZnO, (Figures 3e and f) but not with the commercial initiator (Figure

3-5d). This peak corresponds to the ketone stretch predicted by *Figure 3-1*, consistent with C^{13} NMR single pulse experiments (Figure 8-1). Finally, we observe an increase in ether bonds further indicating polymerizations in systems initiated by semiconducting nanoparticles, P25 TiO_2 or ZnO, (Figures 3e and f).

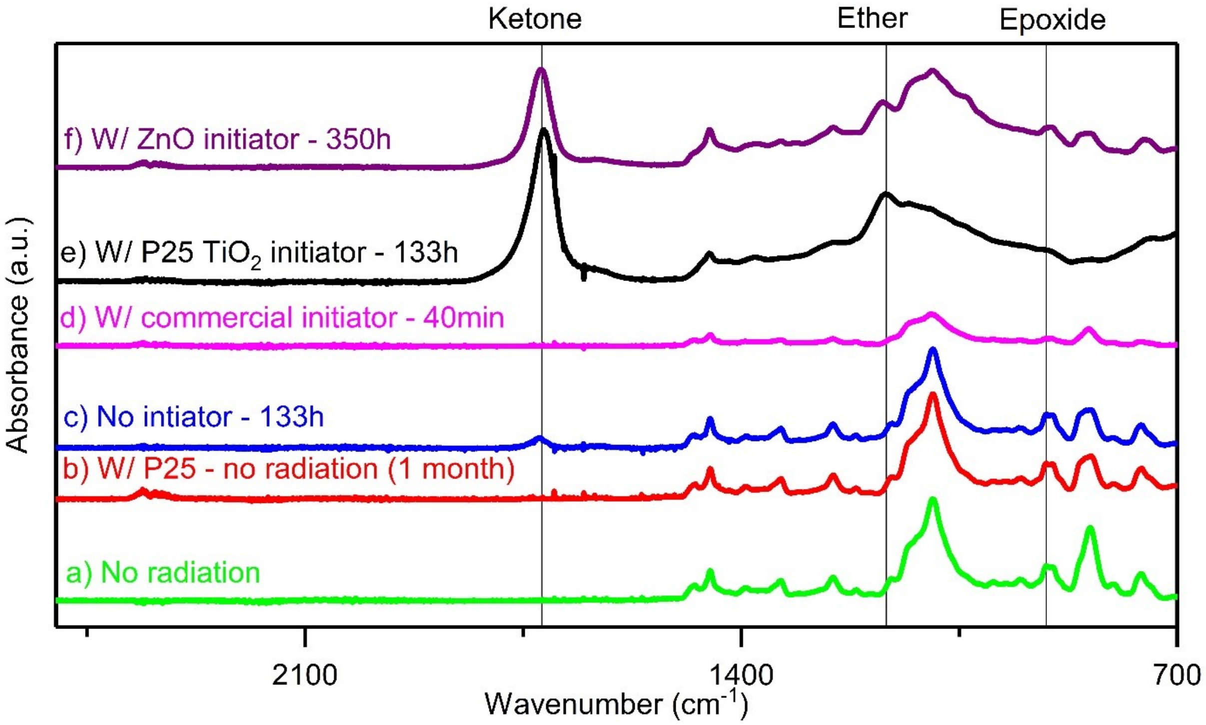

Figure 3-5: FTIR spectra of systems with epoxy and isopropanol (5 wt%) ¬a) not radiated (bottom, green), b) with P25 TiO2 (5 wt%) and no radiation (second from the bottom, red), c) radiated for 133h (third from the bottom, blue), d) with commercial initiator (5 wt%) radiated for 40 minutes (fourth from bottom, magenta), e) with P25 TiO_2 (5 wt%) radiated for 133h (fifth from the bottom, black), and f) with ZnO radiated for 350h (top, purple).

In Figure 3-6, we validate our FTIR quantification using chemical titration. The kinetics of epoxy consumption is monitored via the epoxide peak at 910 cm^{-1} (black squares). Chemical titration (green squares) of the epoxide group by HBr according to ASTM-D1652-97 validates the FTIR measurements and C^{13} NMR observations, all indicating the consumption of epoxy over radiation time.

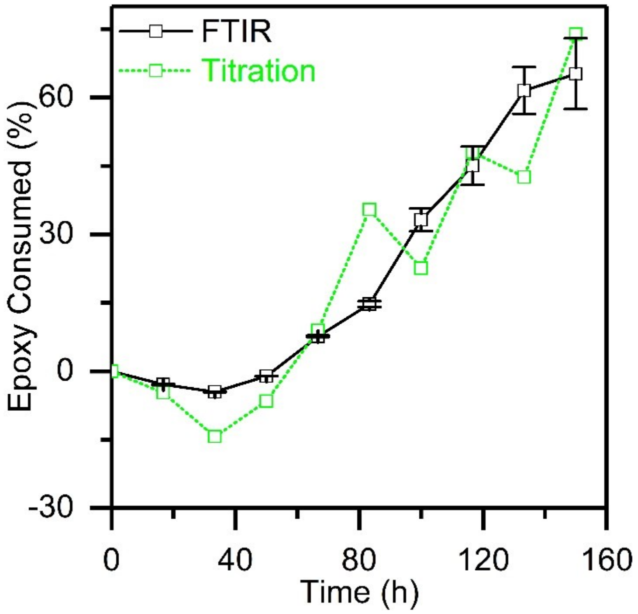

Figure 3-6: Titration (dotted green line with squares) confirmation of FTIR results (Solid black line with squares). Systems contain epoxy, isopropanol (5 wt%) and P25 TiO2 (5 wt%). Error bars indicate 90% confidence limits on the mean of 18 measurements for all t >0.

We monitor reaction kinetics by following the formation of ketones (Figure 3-7a), the consumption of epoxide (Figure 3-7b), and the formation of ethers (Figure 3-7c) via FTIR peaks at 1717, 1167, and 910 cm^{-1} respectively for all systems (Figure 3-5).

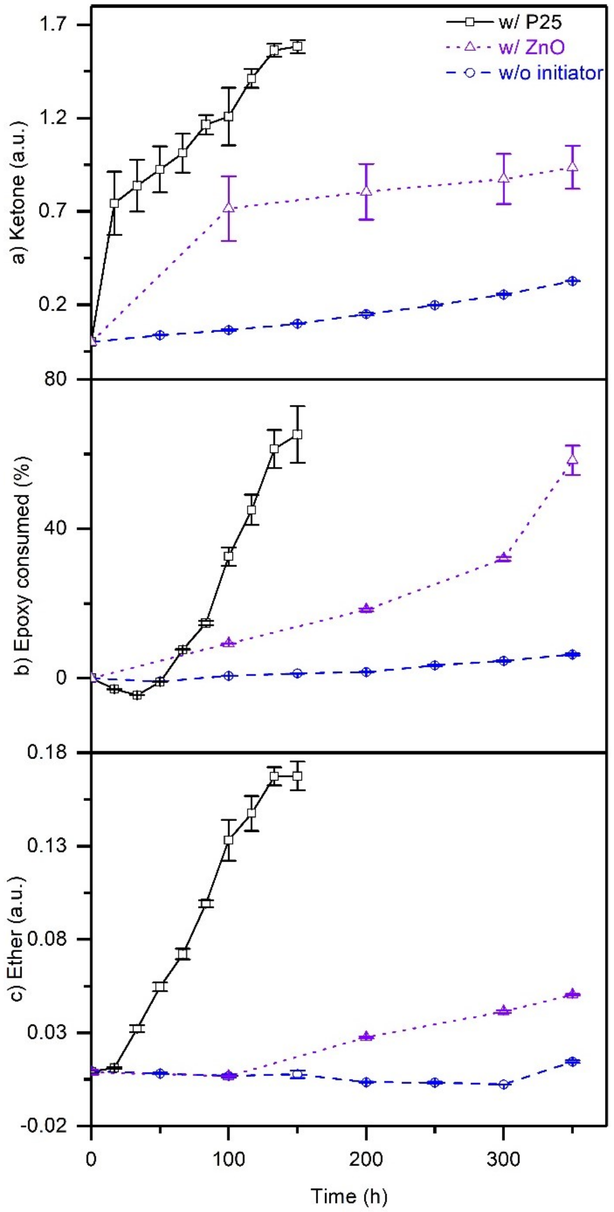

Figure 3-7: Reaction Kinetics: a) ketone formation (FTIR peak at ~1700 cm-1), b) epoxy consumption (FTIR peak at ~ 910 cm-1), and c) ether formation (FTIR peak at ~1167 cm^{-1}). Base composition: epoxy and isopropanol (5 wt%). Systems contain base composition (dashed line with blue circles); base composition with P25 TiO_2 (solid line with black squares) or ZnO (dotted line with purple triangles). All peak areas are normalized relative to the aliphatic peak area (2800-3000 cm^{-1}). Error bars indicate 90% confidence limits on the mean of 18 measurements for all t >0. Note that the horizontal axis is the same for all three graphs.

The control sample, without initiators, shows no sign of reaction in any of the three indicators. Systems with semiconducting nanoparticles, P25 TiO_2 or ZnO, show significant formation of ketones (Figure 3-7a), consistent with alcohol oxidation in *Figure 3-1* and C^{13} NMR single pulse experiments (Figure 8-1). Furthermore, we observe epoxy consumption (Figure 3-7b), and ether formation (Figure 3-7c), in both cases, consistent with epoxy polymerization in Figure 3-1, and C^{13} NMR observations (Figure 3-4c). The reaction is much slower when ZnO is used than when TiO_2 is used, consistent with the literature indicating that TiO_2 is a more efficient photo-catalyst than ZnO[143]. While P25 TiO_2 is used here because it is known to be the superior catalyst, we also use ZnO nanoparticles to generalize our conclusions to metal oxide semiconducting nanoparticles. An apparent induction period in epoxide consumption is observed in samples initiated by P25 TiO_2 (Figure 3-7b). This induction period has been observed and attributed to the formation of a secondary oxonium ion by Crivello.[144]

Finally, another control experiment is conducted using P25 TiO_2 coated with 2-EHA using a procedure similar to what is reported in the literature[145] (Figure 8-2). Coated P25 TiO_2 are inferior initiators to uncoated P25 TiO_2. This detrimental effect of nanoparticle coating indicates that our observations are of a surface reaction.

To speed up the reaction kinetics, we conducted a preliminary investigation of the effects of various system composition parameters including type and concentration of alcohol and TiO_2, and the concentration of electron scavenger. Figure 3-8 compares the reaction kinetics of the improved composition as compared to that of the original. The improved composition consumes 70% of the epoxy after 33 hours, which is 5 times faster than the 150 hours it took for the original composition. We note that in a process such as stereolithography the power intensity used would be several orders of magnitude higher than what is used in this study. This of course would lead to a faster reaction. Nonetheless, there remains a great deal of improvement to the reaction rate needed before it is implemented in a practical process. Parameters such as the semiconducting nanoparticle band gap energy and light wavelength should be explored to improve reaction kinetics because it is already well established that a good match between semiconducting nanoparticle band gap energy and light wavelength is critical in catalytic applications[146]. We note that titania has been found to increase the glass transition temperature and modulus of epoxy.[147] It has also been found that the modulus and yield strength of titania-epoxy composites are highest at 5 titania wt% and decrease at higher loadings due to the creation of microcracks.[148]

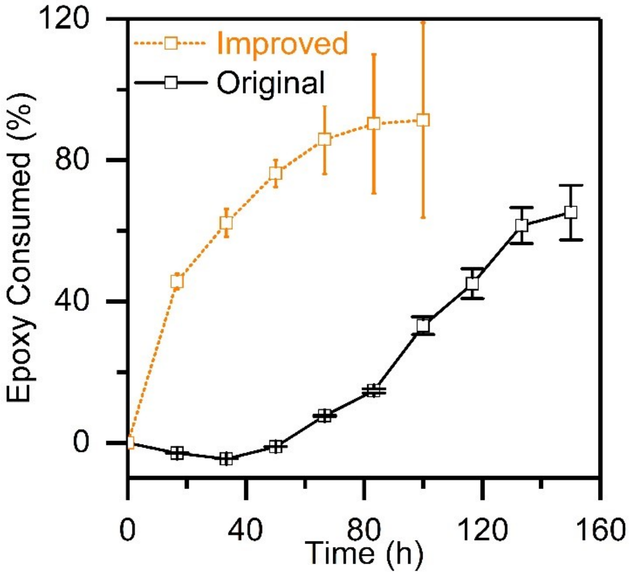

Figure 3-8: Composition improvement. The original system (solid black line) contains epoxy, isopropanol (5 wt%), and P252 (5 wt%). The improved system (dotted orange line) contains epoxy, 1-phenethyl alcohol (10 wt%), MV (0.5 wt%), and pure anatase TiO2 (25 wt%). Error bars indicate 90% confidence limits on the mean of 18 measurements for all t >0.

3.4.3. Film Characterization

We evaluate the physical properties of the films to confirm that the film is polymerized. We conducted a swelling experiment where we left a film (thin film of the improved system from Figure 3-8, 483h of radiation) immersed in a beaker of acetone for 24 hours. The film showed no visible changes in its appearance and no weight loss. On the other hand, an unpolymerized film of the same composition completely dissolved in acetone after 5 minutes. These swelling experiments indicate that the polymerized epoxy film is cross-linked.

3.5. Conclusions

We demonstrate that semiconducting nanoparticles can initiate epoxy photo-polymerization. Considering the myriad of semiconducting heterogeneous photo-catalysts, this work opens a new class of epoxy photo-initiators.

Another immediate implication of our findings is that epoxy/TiO_2 nanocomposites are likely to suffer from photo-instability because the band gap energy of TiO_2 is within the solar spectrum, and thus it will initiate the reactions reported here whenever exposed to sunlight. Such instability of epoxy/TiO_2 nanocomposites has been reported[149,150] but not previously related to the occurrence of the reactions reported here.

4. Flame-made TiO_2

4.1. Abstract:

Titania nanoparticles containing both monoclinic (TiO_2(B) – a promising battery material and catalyst) and anatase crystal phases are synthesized with a low-cost, scalable flame spray pyrolysis (FSP) process, as confirmed by X-ray diffraction, transmission electron microscopy and Raman spectroscopy. The latter reveals TiO_2(B) contents of up to 27 % in the crystalline phase fraction. The amount of TiO_2(B) increases as the time for nanoparticle growth in the flame decreases through quenching with ambient air. It can be controlled by varying the flow rates of precursor solution and dispersion oxygen into the flame. The FSP-made titania outperforms commercial titania P25 in the photocuring of epoxy, indicating its potential as a photocatalyst.

4.2. Introduction

Titanium dioxide nanoparticles are typically produced in industry with flame reactors through oxidation of titanium tetrachloride vapor, as is the majority of pigmentary-grade titania.[151] In fact, TiO_2 is the second largest commodity made by flame reactors, outnumbered in tonnage only by carbon black.[85] Unless dopants are employed to increase the rutile yield, e.g. for application as white pigments[151,152], product powders are a mixture of anatase and rutile polymorphs. One prominent example is high surface area (~50 m^2/g) titania P25 (Evonik Industries AG) with approximately 88 wt% anatase and 12 wt% rutile[137] that has broad application as a photocatalyst. Titania nanopowders have also been produced by flame spray pyrolysis (FSP)[153,154] in which a liquid mixture of an organic solvent and a titanium-containing compound, typically titanium (IV) tetraisopropoxide, is sprayed and combusted. With flames burning in air, similar phase compositions as for P25 are obtained, while careful adjustment of the oxygen partial pressure in the FSP reactor allows to control the anatase content over a broad range of 6 to 96 wt% with the balance rutile.[155]

TiO_2 can also attain other crystal phases than anatase and rutile, namely brookite, TiO_2(II), TiO_2(H), and monoclinic TiO_2(B).[156] Recently, TiO_2(B) has gained special attention as it has the lowest density[157] and most open crystal structure[158,159] of all titantia polymorphs with open channels along the b-axis in the [001] direction.[160] These properties allow for fast Li+ intercalation[161], making it ideal for rechargeable lithium-ion battery applications.[157,162,163] Furthermore, smaller TiO_2(B) nanoparticles provide shorter diffusion paths[164], improving battery charging and discharging times.[158] Furthermore, TiO_2(B), is attractive due to its energy bands which differ from and interact with the energy bands of other crystal structures.[165] Consequently, it may lead to photocatalytic activity similar to or better than P25 in other applications.[165,166]

TiO_2(B) is found in nature only in trace amounts[156] and was first synthesized from potassium octatitanate via hydrolysis and ion exchange followed by complete dehydration.[167] Other synthesis routes include the basic sol-gel[168] and related microwave[166,169] processes. All current synthesis routes are multi-step, multi-day processes. For example, sol-gel synthesis involves an autoclave heating step that lasts multiple days. The fastest synthesis of bulk nanoparticles (a few grams) appears to be microwave-assisted sol-gel process that reduces the autoclave heating step to 3 hours[169]. On the other hand, flame synthesis is a single-step process that can produce nanoparticles in minutes, at rates on the order of 100 metric tons per day industrially.[76] To the best of our knowledge, the TiO_2(B) phase has never been reported in the products of flame reactors.

Here, we take a closer look at titania nanopowders produced via flame spray pyrolysis with the help of Raman spectroscopy, high resolution transmission electron microscopy (HRTEM) and X-ray diffraction (XRD). We observe up to 27 wt% of TiO_2(B) in product powders along with anatase and some rutile, and show how this fraction can be controlled by process conditions. The

FSP-made powders are evaluated in the photocuring of epoxy and compared against P25 as well as TiO_2(B) produced by a wet-phase process.

4.3. Experimental

4.3.1. Particle synthesis

A precursor solution with 0.25 mol/L total metal concentration is prepared by diluting precursors with xylenes (Sigma Aldrich, Reagent grade). The precursors used are titanium (IV) tetraisopropoxide (Sigma Aldrich, 97%), Zn-2-ethylhexanoate (Strem Materials, 80%), tin-2-ethylhexanoate (Sigma Aldrich, 92.5-100%), copper-2-ethylhexanoate (Strem Materials, 16-19% Cu), hexamethyldisiloxane (Sigma Aldrich, 98.5%) for Ti, Zn, Sn, Cu, Si respectively. This precursor is fed at 1 to 5 mL/min through the capillary of the flame spray pyrolysis reactor[170,171] and atomized by 2 to 5 L/min of oxygen. These process conditions are denoted by P/D here where P is the precursor flow rate in mL/min, and D is the dispersion oxygen flow rate in L/min. The precursor spray is ignited with a pilot flame fueled by 1.25 L/min of CH_4 premixed with 2.5 L/min of O_2. Product titania particles are collected on glass fiber filters (Albet-Hahnemühle, GF 6, 25.7 cm diameter) placed in a water-cooled stainless-steel holder with the help of a vacuum pump (Busch, Seco SV 1040 C). In some experiments, the flame is surrounded by a quartz glass tube (5 cm inner diameter, 20 cm length) following Waser et al.[172] When the tube is installed, sheath oxygen of 10 L/min is introduced in co-flow to the spray flame to reduce nanoparticle deposition on the tube walls. In some instances, samples are annealed for 2 hours at 500 °C in air in a muffle furnace (Carbolite CWF 1300).

TiO_2(B) is synthesized using a sol-gel method according to Amstrong et al.[162] and Yang et al.[165] Anatase titania (Sigma Aldrich) is treated with 10 M NaOH at 180 °C for 48 hours in an autoclave with Teflon beaker. The resulting cake is mixed with dilute HCl (0.05 M) for 4 hours followed by washing with distilled water and filtration. Product titanate is transformed into TiO_2(B) by annealing in air for 4 hours at 400 °C in a muffle furnace (Carbolite CWF 1300).

4.3.2. Particle characterization

X-ray powder diffraction (XRD) is performed on a Bruker D8 Advance diffractometer (Cu Kα radiation, 40 kV, 30 mA, Bragg–Brentano geometry, equipped with Lynxeye detector, 0.02° step size, 2 s/step) in the range of $10° < 2\theta < 70°$. Samples are analyzed pure and with 15 wt% of nickel oxide as an internal standard to quantify the amorphous and crystalline contents[137,173,174]. Phase fractions are determined by peak area integration at 15°, 25.5°, 27.5°, and 42.5° for TiO_2(B), anatase, rutile and NiO respectively. The following equations are used:

$$f_{(anatase,rutile,monoclinic)} = \frac{area_{anatase,rutile,monoclincic}}{(\frac{85}{15})\times area_{NiO}} \qquad (10)$$

$$f_{amorphous} = 1 - f_{anatase} - f_{rutile} - f_{monoclinic} \qquad (11)$$

Transmission electron microscopy (TEM) is performed on a Tecnai F30 (FEI) microscope operated at 300 kV (point resolution ca. 0.2 nm). Images are recorded with a Multiscan CCD 794 camera (Gatan Inc.). Specific surface areas are determined by nitrogen adsorption (Micrometritics Tristar II) at 77 K employing the Brunauer-Emmett-Teller (BET) isotherm after degassing the sample in nitrogen at 150 °C for at least 2 hours. An SSA-equivalent primary particle diameter is calculated as $d_{SSA}[nm] = 6000 / (SSA\cdot[m^2/g]\ \rho p\ [g/cm3])$, where a density of $\rho_p = 3.8\ g/cm^3$ for anatase titania is used.

Raman spectra are recorded with a Renishaw spectrometer, using a 785 nm laser at 50% power with 10 seconds exposure time from 100 cm^{-1} to 800 cm^{-1}. 5% laser power is used in the case of sol-gel TiO_2(B) due to signal saturation at higher power. The Raman shifts at 144 and 123 cm^{-1} for anatase and TiO_2(B) respectively are deconvoluted to quantify the relative ratio of anatase to TiO_2(B) nanoparticles following Beuvier et al.[175] The average and standard deviation of scans of 6 different spots are reported.

4.3.3. Epoxy curing

Mixtures (1.5 g total weight) consisting of 1-4 cyclohexane dimethanol diglycidyl ether (referred to as "epoxy" here, Sigma-Aldrich, technical grade), 5 wt% isopropanol (Sigma-Aldrich, 99.5%), and 5 wt-% nanoparticles are stirred overnight and then sonicated for 30 minutes while being water-cooled (5 seconds on, 20 seconds off for a total time of 40 minutes, 95% amplitude, 40 W, 100000 J total energy) using a Vibracell VCX 500 equipped with a cup horn. Mixtures are prepared using commercial titania P25 (Evonik) or FSP-made nanoparticles. The mixtures are blade-coated on microscope glass slides using 0.0025-inch-thick kapton tape (McMaster-Carr). These films are then radiated using a 365 nm UVA lamp (UVP, XX-15M), with a light intensity of approximately 2 mW/cm^2 at the surface of the films for up to 144 hours. The cure percentage is measured by Fourier transform infrared (FTIR) spectroscopy in ATR mode on 6 different spots of each film using 64 scans at 1 cm^{-1} resolution scanning from 600 cm^{-1} to 4000 cm^{-1} (Bruker Vertex 70v).

4.4. Results and Discussion

4.4.1. Particle characteristics

Figure 4-1 shows how the specific surface area (SSA) of titania nanoparticles can be controlled between 98 and 252 m^2/g by varying the oxygen dispersion gas flow at constant 1 mL/min precursor feed (squares) or changing the precursor flow at constant 5 L/min dispersion-O_2 (triangles). Specifically, the SSA increases from 160 to 252 m^2/g as the dispersion gas flow increases from 2 (1/2 flame) to 5 L/min (1/5 flame). This is typically observed in FSP synthesis of nanoparticles as higher dispersion gas flows lead to shorter, colder and more dilute flames, and hence shorter high temperature residence times for nanoparticle growth.[82,170] In contrast, increasing the precursor feed at constant oxygen dispersion gas flow decreases the SSA from 252 m^2/g (1/5 flame) to 98 m^2/g (5/5 flame) due to longer high temperature residence times and higher particle concentrations. The SSA of the 5/5 product is in excellent agreement with Jossen et al.[176] reporting 100 m^2/g for a similar flame but toluene as solvent.

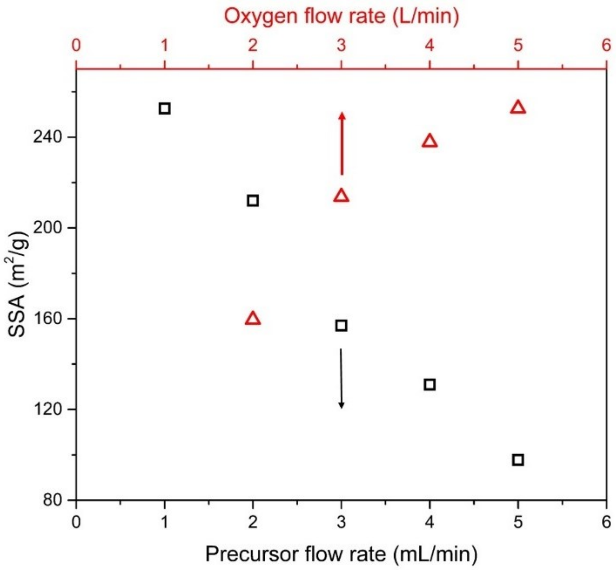

Figure 4-1: Specific surface area of FSP-made titania as a function of precursor flow rate at constant 5 L/min dispersion O_2 flow (black squares, bottom abscissa) as well as of dispersion O_2 flow at constant 1 mL/min precursor flow (red triangles, top abscissa). Increasing the precursor flow and thereby the flame enthalpy and particle concentration decreases the SSA rather linearly while it is increased by higher oxygen flow rates.

Figure 4-2 shows the XRD patterns of commercial titania P25 (top), FSP-titania as well as sol-gel made TiO_2(B) (bottom) in the region of the most intense reflections between $10° \leq 2\Theta \leq 35°$. The pattern of P25 shows the characteristic reflections of anatase (25.5°, PDF 86-1156) and rutile (27.5°, PDF 87-0710). Peak analysis with the help of a 15 wt% NiO standard (reflection at 42.5°, data not shown, PDF 44-1159) reveals a fully crystalline sample with 88 wt% anatase and 12 wt% rutile similar to Ohtani et al.[137] Note, however, that in some P25 samples, Ohtani et al.[137] reported up to 13 wt% amorphous fraction. An amorphous content of ~23 wt% was determined here for FSP-titania made in the 5/5 flame (green line in Figure 4-2), along with 68 wt% anatase and the balance rutile. Similar amorphous fractions in FSP titania were recently reported by Fujiwara et al.[174] for different flame conditions and precursor solutions. The anatase to rutile ratio of the FSP 5/5 sample here is similar to that of P25 as well as FSP-made titania reported by Jossen et al.[176], that did not consider the presence of an amorphous fraction.

When the ratio of precursor to dispersion oxygen flow is decreased by reducing the precursor or increasing the dispersion oxygen flow rate, diffraction peaks become broader indicating smaller crystallites in agreement with the increasing specific surface area (Figure 4-1). Furthermore, the rutile reflection at 27.5° becomes weaker and a reflection at 15° appears indicating the presence of another phase while the peak at 25.5° remains dominant. This is most pronounced for the 1/5 flame having the lowest precursor and highest dispersion oxygen flow rates making it the shortest and coldest flame. These effects did not allow a reliable quantitative determination of the amorphous product fraction for flame ratios below 5/5. However, at least similar amorphous contents are expected as shorter high temperature particle residence times and faster quenching should promote the formation of amorphous domains.

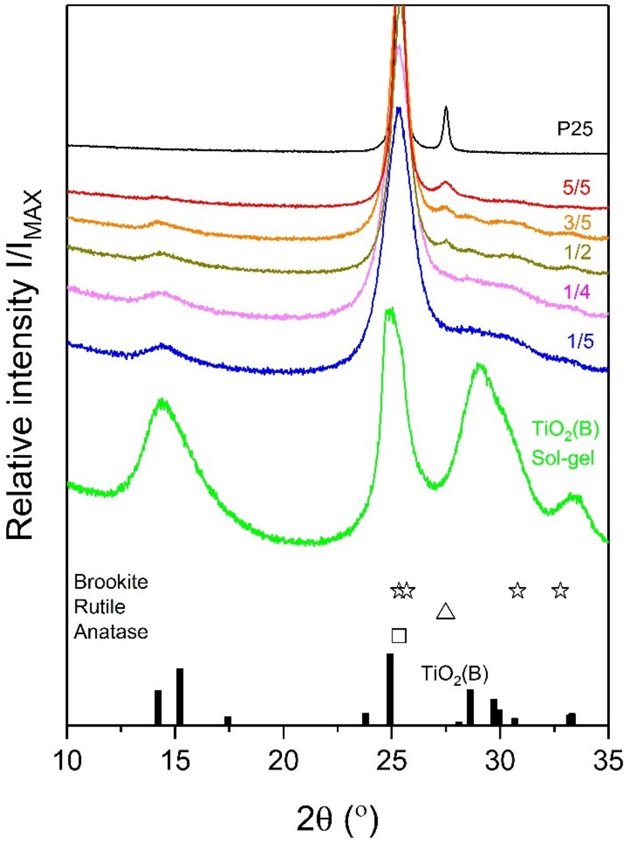

Figure 4-2: XRD patterns of P25 (top), FSP-made titania made with precursor / dispersion oxygen ratios of 1/5 to 5/5, and pure sol-gel TiO2(B) (bottom) along with the characteristic reflections of TiO2(B) (bars, bottom legend), anatase (square), rutile (triangle)

The reflection at 15° neither is characteristic for anatase (square, top of Figure 4-2) nor rutile (triangle) nor brookite titania (stars, PDF 29-1360). It is the characteristic reflection of $TiO_2(B)$, as shown by comparison with PDF 46-1237 (bars at the bottom of Figure 4-2) and corresponds to the 001 plane and a spacing of 0.64 nm which is unique to $TiO_2(B)$.[168] The XRD pattern of a predominantly $TiO_2(B)$ nanopowder made here by a sol-gel process is shown in the bottom row of Figure 4-2. Reflections at 15°, 25.5°, 28° and 33° can be observed. While the reflection at 15° is unique to $TiO_2(B)$ amongst all TiO_2 crystal structures, the reflection at 25.5° is the dominant reflection for both $TiO_2(B)$ and anatase titania. This overlap makes it difficult to identify $TiO_2(B)$, especially as X-ray diffractograms of TiO_2 frequently only show the 2Θ region above 20°, as in previous reports on FSP-made titania.[176,171,177] The other reflections of TiO_2(B) at 28° and 33° are much weaker and overlap with reflections of rutile (28°) and brookite (33°).

Figure 4-3 shows high-resolution TEM images of nanoparticles made in the 1/5 flame. Primary particle sizes are in the order of 5 nm in agreement with an SSA-equivalent particle size of 6 nm, and characteristic for this powder made in a rather cold flame with short high temperature residence time. Sinter necks between primary particles indicate aggregation as the time available for particles is insufficient for them to fuse into larger spheres. Lattice fringes are discernible up to the surface corroborating a monocrystalline structure in many particles. The unique 0.64 nm spacing of the 001 plane of TiO_2(B) that gives rise to the reflection at $2\Theta = 15°$ (Figure 4-2) appears (magnification in Figure 4-3) in some particles. This indicates the presence of individual TiO_2(B) crystals in the product nanopowder.

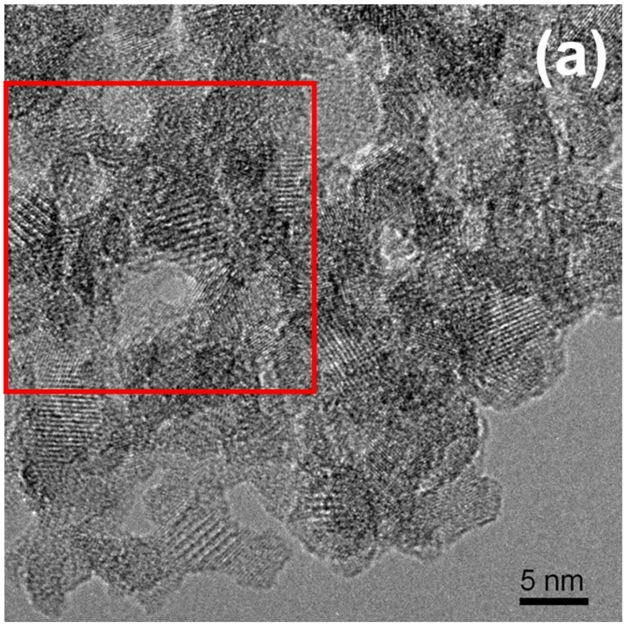

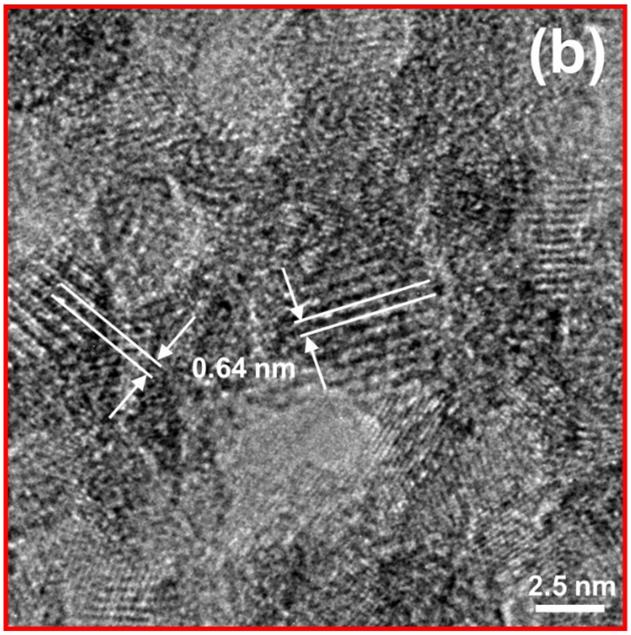

Figure 4-3: HRTEM image of titania nanoparticles made in the 1/5 FSP flame showing aggregated primary particles of ~5 nm size. The magnified area (red rectangle) shown in (b) reveals the 0.64 nm spacing characteristic for TiO_2(B) in some particles.

Raman spectroscopy is conventionally used to quantify the TiO_2(B) crystal fraction.[175] Figure 4-4 shows the Raman spectra of P25 (top), the FSP-made titania nanopowders of Figure 4-2, and sol-gel derived TiO_2(B) (bottom). P25 and all FSP-made powders show the characteristic and pronounced anatase bands[178] at 144, 201, 398, 515 and 639 cm^{-1}. The band at 144 cm^{-1} shifts slightly as the dispersion oxygen flow rate increases or the precursor flow rate decreases (inset). Such a shift has been reported before for decreasing anatase crystallite sizes.[179] Here, smaller primary particles (Figure 4-1) and crystals (Figure 4-2) are produced as the precursor to dispersion oxygen flow ratio decreases. A characteristic Raman mode of rutile titania is at 447 cm^{-1} but is rather weak and typically difficult to see.[178] This rutile mode is indicated by a small hump in the spectrum of P25 but is hardly discernible in FSP-made powders here, in line with low rutile contents suggested by XRD (Figure 4-2).

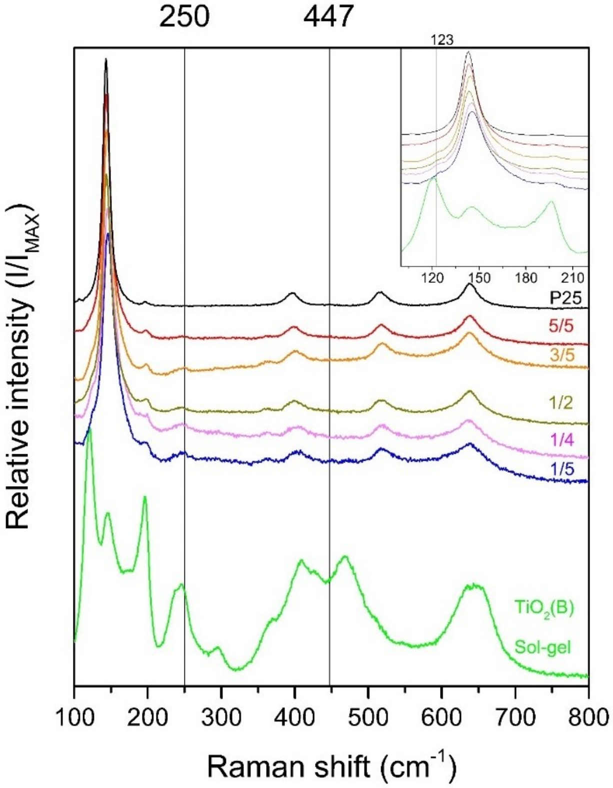

Figure 4-4: Raman spectra of P25 (top), FSP-made titania, and pure sol-gel TiO2(B) (bottom) showing the band at 250 cm^{-1} corresponding to $TiO_2(B)$. The higher magnification in the inset shows the shoulder at 123 cm^{-1} corresponding to $TiO_2(B)$ as well as the shift of the Raman band around 144 cm^{-1} due to particle size.

A band at 250 cm^{-1} and a shoulder at 123 cm^{-1} can be observed in FSP-made titania but not in P25. Those bands are characteristic of $TiO_2(B)$[163,175], as is apparent from the $TiO_2(B)$ sample made in the liquid phase (bottom spectrum in Figure 4-4). The $TiO_2(B)$ bands at 250 cm^{-1} and shoulder at 123 cm^{-1} are strongest in the particles made in the coldest flame with 1/5 setting and weakest in the particles made in the hottest flame, (5/5) in line with XRD results (Figure 4-2). Such $TiO_2(B)$ bands are also discernible in the Raman spectra of similarly made FSP-titania reported by Teleki et al.[180] but had not been assigned.

The ratio of anatase to $TiO_2(B)$ is quantified by deconvoluting Raman shifts at 144 cm^{-1} (anatase) and 123 cm^{-1} following Beuvier et al.[175] Figure 4-5 shows the amount of $TiO_2(B)$ in the crystalline fraction of the nanopowder as a function of specific surface area, assuming negligible rutile content. We observe a clear trend of increasing TiO_2(B) content from ~13 wt-% at 98 m^2/g (5/5 flame) to ~27 wt-% at 252 m^2/g (1/5 flame) despite the large error bars related to the accuracy of the deconvolution procedure. Particles made in different flames but with similar specific surface area (flames 2/5 and 1/3 or 3/5 and 1/2 flames in Figure 4-5) have similar TiO_2(B) contents. It should be kept in mind that the FSP-made titania is likely containing an amorphous fraction, as indicated by Fujiwara et al.[174] and our finding of ~23 wt% for the product of the 5/5 flame. Therefore, actual fractions of crystalline anatase and TiO_2(B) in the product should be lower than shown in Figure 4-5. Though, none of those flame conditions produce pure TiO_2(B), it has been shown that titania particles with as little as 5 wt% of TiO_2(B) improve the first discharge capacity of lithium batteries by 20% and rate performance by 25% compared to pure anatase particles[181].

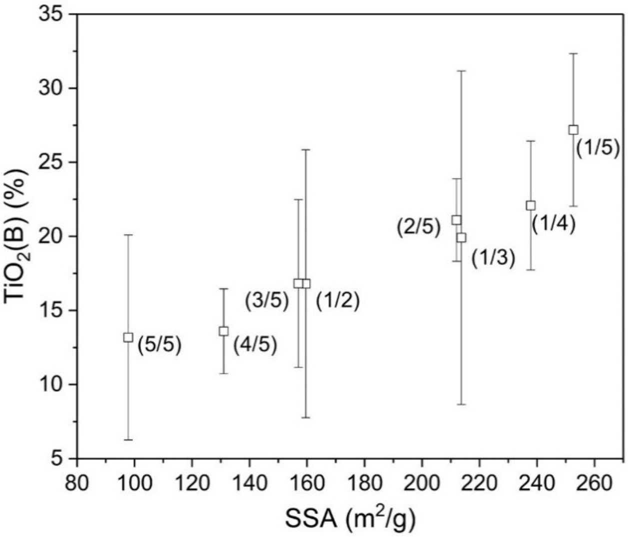

Figure 4-5: Amount of TiO_2(B) in the crystalline titania fraction (%) as a function of the specific surface area (m^2/g). Increasing the specific surface area by decreasing the precursor to dispersion gas feed ratio (P/D) increases the weight fraction of monoclinic titania, TiO_2(B), from ~13% at 98 m^2/g to ~27% at 252 m^2/g (1/5 flame). Note that the rutile content was negligible in these powders and that a potential amorphous fraction would lower the contributions of the crystalline phases.

The increasing TiO_2(B) content with increasing specific surface area (Figure 4-5) indicates that colder and shorter flames, i.e. shorter high temperature particle residence times and possibly faster quenching, promote the formation of monoclinic titania. TiO_2(B) is metastable and recrystallizes into anatase titania at temperatures above 550 °C.[182] FSP flames typically have maximum temperatures above 2300 °C[82,170,171,183], much higher than the TiO_2(B) to anatase transition temperature. However, computational fluid dynamics simulations and FSP reactor scaling proposed by Gröhn et al.[82] suggests that a 1/5 xylene-based flame should have a high temperature particle residence time in the order of 1 ms while it is ~10 ms in a 4/5 flame. There is simply not enough time at high temperature for TiO_2(B) to recrystallize into the more stable anatase and rutile phases at the high quenching rates encountered in the FSP flames. Other possible explanations for the presence of such a metastable phase in small flame-made particles may be the preferred crystallization in the simplest structure and the formation of the lowest density phase to counteract high surface energies.[184] This is consistent with our observations of increasing TiO_2(B) content with shorter high temperature residence time and resulting smaller primary particles, since TiO_2(B) has the lowest density among all TiO_2 phases and the monoclinic system is one of the simplest crystal structures.

Annealing the nanopowder with the highest TiO_2(B) content made in the 1/5 flame at 500°C for 2 hours removes all characteristic signals of TiO_2(B) in both XRD and Raman. Note that this temperature is lower than the phase transition temperature reported by Brohan et al.[182] Additionally, the rutile XRD reflection at 27.5 can be observed after annealing, as anatase starts to convert into the thermodynamically stable rutile at such temperatures.[185] Similarly, surrounding the 1/5 flame by a tube and thereby preventing ambient air entrainment and flame quenching[172] leads to longer high temperature residence times, and eliminates all signs of TiO_2(B) in XRD and

Raman (data not shown). Longer residence times at high temperature may be the reason why no TiO_2(B) but some rutile is observed in flame-synthesized commercial titania P25.

4.4.2. Epoxy curing

The performance of FSP-titania made in the 1/5 and 5/5 flames is tested for the photocuring of epoxy and compared to P25, the gold standard for photocatalytic activity, and sol-gel TiO_2(B). Photocuring of polymers is integral in applications like coating, dentistry, the manufacturing of printed circuit boards, and stereolithography 3D printing.[9,10,19] Previous work demonstrates a novel mechanism to photocure epoxy using semiconducting nanoparticles.[16] Here, we use this reaction to evaluate the photocatalytic activity of the FSP-titania. Note that the power intensity used in these experiments is 2 mW/cm^2, orders of magnitude lower than the W/cm^2 used in typical stereolithography 3D printing applications employing epoxy photocuring.

Figure 4-6 shows curing kinetics of the 1/5 (squares) and 5/5 (triangles) FSP titanias, P25 (circles), and sol-gel TiO_2(B) (diamonds) as calculated from FTIR spectra by normalizing the epoxide peak[186] at ~910 cm^{-1} relative to the aliphatic peaks. P25 and titania made in the 5/5 flame having the lowest TiO_2(B) content and being closest in composition to P25 perform similarly, even though titania made in the 5/5 flame has more than twice the surface area (98 m^2/g) as P25 (47 m^2/g). FSP particles made in the 1/5 flame which have the highest TiO_2(B) crystal fraction and the highest surface area (252 m^2/g) perform 2-3 times more efficiently than P25. This improvement cannot be explained by the higher surface area alone given the small effect of surface area inferred by comparing the similar performances of P25 and 5/5 titania. This relatively small effect of particle surface area has previously been observed for this reaction also with pure anatase particles.[16] Sol-gel TiO_2(B), with SSA of 39 m^2/g, has the poorest performance of all the particles tested. This is attributed to the fact that these are single phase particles. It is well known that multiple crystal structure[16,165], or even multiple materials[187,188], slow down electron-hole recombination, improving catalytic properties. Thus, interactions between the anatase and TiO_2(B) crystal structures in our mixed phase FSP-made particles reduce the rate of electron hole recombination, significantly improving the photocatalytic activity. Note that the TiO_2(B) to anatase ratio in 1/5 titania is the same as the rutile to anatase ratio in P25.

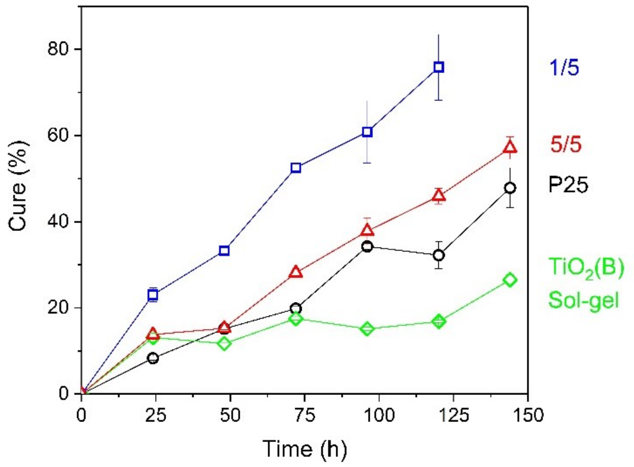

Figure 4-6: Epoxy photocuring calculated from FTIR spectra as a function of time using titania made in 1/5 and 5/5 FSP flames, commercial titania P25, and sol-gel TiO_2(B) as catalysts. Mixtures are epoxy, isopropanol (5 wt%), and nanoparticles (5 wt%). Error bars are 90% confidence limits. Note that flame-made titania outperforms P25, and single phase TiO_2(B).

4.5. Conclusions

For the first time, we demonstrate the presence of TiO_2(B) in titania nanoparticles made by flame spray pyrolysis, accounting for up to ~27 % of the crystalline fraction. The formation of this metastable phase is attributed to very short (milliseconds) high-temperature residence times and steep temperature gradients of the FSP flame. In addition to anatase and TiO_2(B), FSP-made titania may contain an amorphous weight fraction, as high as ~23%. These phases should be considered in the characterization and performance evaluation of flame-made nanopowders. Based on catalyst weight, flame-made titania can show higher photocatalytic efficiency for photocuring epoxy compared to P25, the gold standard for photocatalytic activity. Continuous, single-step mass production of such particles can be readily achieved with flame spray pyrolysis in the same manner as P25 is currently mass produced.

Monoclinic/anatase mixed particles may open the door to a new class of catalysts and new applications. Here, we show only one such application, catalyzing epoxy photo-curing. The performance of these particles should also be investigated in photovoltaic and battery applications. Perhaps this mixture of TiO_2(B) and anatase could replicate the impact of the mixture of rutile and anatase of P25.

5. Flame-made metal oxide quantum dots embedded in a silica matrix

5.1. Abstract

Quantum dots have unique size-dependent properties and promising applications. However, their use in many applications remains hindered by mechanical, thermal and chemical instability, and the lack of viable quantum dot mass-production processes. Embedding quantum dots in matrices such as silica counteracts the instability challenges in some applications while preserving their unique properties and applicability. Here, we synthesize quantum dots of four different metal oxides embedded in a silica matrix in a one-step mass production process using flame spray pyrolysis.

5.2. Introduction

Quantum dots are the object of considerable interest due to their remarkable optical and electronic properties such as high quantum efficiency, and narrow size-dependant absorption and luminescence windows.[32,33,34] The quantized effect[35] is most easily observed when the crystal size is below the Bohr diameter.[34] The applications of metal oxide quantum dots range from photocatalysis (TiO_2)[42,57,58], UV protection films (ZnO)[41,44], gas sensing (SnO_2)[50,51], high temperature superconductors (CuO).[54] Further, semiconducting quantum dots have been shown to photo-polymerize acrylics via free radical polymerization.[12,24,25] We have recently shown that semiconducting nanoparticles such as TiO_2 and ZnO can photopolymerize epoxy via cationic polymerization.[16] The two most major obstacles faced by quantum dots preventing the commercialization of many of those applications are their mechanical, thermal and chemical instability, as well as the lack of viable large-scale production.[39,49,59]

The stability of quantum dots can be improved by embedding them in amorphous matrices.[39] For example, embedding quantum dots in an amorphous carbon matrix counteracts the aggregation and volume swelling challenges encountered during lithiation in battery applications.[49] Ge et al.[189] also embedded CuO quantum dots (1-2 nm) in a silica matrix which showed improved thermal stability. Further, these amorphous matrices improve wetting and dispersion that are critical to photocatalytic activity.[64]

The synthesis of quantum dots embedded in amorphous matrices suffer from the inherent challenge of high activation energy because of the composition and solubility of the semiconducting particles in the amorphous matrix.[39] Further, quantum dots embedded in amorphous matrices intended for photocatalytic applications must avoid a core-shell structure where the semiconducting material core is hermetically sealed by the amorphous shell as this will eliminate surface reactions.[65] On the other hand, segregated particles with distinct crystalline and amorphous domains exhibit high photocatalytic activity.[65]

The need for viable high-volume production of quantum dots remains unmet. Quantum dots are usually synthesized using wet chemistry techniques that are relatively complex, require hours, and with a production rate in the order of grams per day.[39,42,44,48,49,68] Alternatively, flame spray pyrolysis (FSP) is a one step process that produces metal oxide nanoparticles at industrial rates in the order of tonnes per day.[85] FSP also allows great versatility in combining different materials. Various FSP process parameters can be used to control particle size such as the dispersion gas and/or precursor flow rates.[17] However, precise control of the very small crystal size required to synthesize quantum dots remains elusive. Teleki et al[88] observed the blue shift in band gap energy that is characteristic of the quantized effect in titania that is thermophoretically collected at different heights from within the flame. To the best of our knowledge, there is currently only one publication on synthesizing ZnO particles small enough to exhibit the quantized effect via FSP.[89] In that study, Mädler et al. added silica to the precursor mixture to provide a matrix that caps the size of ZnO crystals and provides access to the smaller crystal size and narrower size distribution that exists at early stages within the flame. The coprecipitation of ZnO and silica hinders the sintering of ZnO or its coalescence. Further, Tani et al[190] demonstrated the thermal stability of flame-made ZnO/SiO_2 particles. Here, this approach is generalized as we demonstrate that FSP can be used to synthesize quantum dots, embedded in a silica matrix, of many metal oxide semiconducting materials: TiO_2, ZnO (over a broader size range than what Mädler et al. explored), SnO_2 and CuO.

5.3. Theory

The exciton Bohr diameter of a semiconducting material, d_{Bohr} is calculated via Equation 12.[36,37]

$$d_{Bohr} = 2R_{Bohr} = \frac{2\hbar^2\varepsilon}{e^2\mu} \qquad (12)$$

Where $\hbar = 1.05 \times 10^{-34}$ J·s is the reduced Plank's constant, ε is the dielectric constant of the material, $e = 1.6 \times 10^{-19}$ C is the elementary charge, and μ is the reduced mass of the material's exciton.

Equation 13 governs the relationship between the crystal size in terms of radius and band gap energy (E^*).[40]

$$E^* = E_g + \frac{\hbar^2\pi^2}{2R^2\mu} - \frac{1.8e^2}{\varepsilon R} \qquad (13)$$

Where E_g is the bulk band gap energy of the material (at $R \rightarrow \infty$). Equation 13 illustrates that the quantized effect is most significant at sizes below the exciton Bohr diameter but still occurs at bigger sizes. It is important to note that Equation 13 has limitations because of the assumptions it involves[34,39], particularly at sizes below 3 nm due to a significant increase in the electrons' kinetic energy[191].

Table 3 shows the standard properties of each of the materials used in this study, where $m_0 = 9.1 \times 10^{-31}\ kg$ is the mass of a free electron. The exciton Bohr diameter calculated using Equation 1, and the tabulated material properties, are consistent with the values found in the literature.

Table 3: Material properties

	TiO_2 (Anatase)[42]	ZnO (Zincite)	SnO_2 (Cassiterite)[43]	CuO (Monoclinic)
ε	31	3.7 (ref 44)	14	25 (ref 45)
μ/m_0	1.630	0.157 (ref 46)	0.275	0.381 (ref 47)
Eg (eV)	3.2	3.2 (ref 46)	3.6	1.5 (ref 47)
Bohr diameter (nm) from literature	2	2.5 (ref 46)	5.4	6.6-28.7 (ref 48)
Calculated Bohr diameter (nm) (eq 2)	2	2.5	5.4	7

5.4. Results and discussion

Figure 5-1 shows XRD patterns of flame-made TiO_2, ZnO, SnO_2 and CuO. Where X is the molar fraction of the metal oxide and the balance is silica. Therefore, when "X" is 1, the particles are made of pure metal oxide and contain no silica. On the other hand, particles contain silica when "X" is smaller than one. The XRD patterns indicate that ZnO, SnO_2 and CuO have hexagonal, tetragonal and monoclinic crystal structures respectively. TiO_2 has anatase (reflection at 25°), monoclinic (weak reflection at 15°) crystal structures, consistent with our earlier observations[17], and traces of rutile (reflection at 30°). The XRD patterns of flame-made TiO_2 with X=1, 0.8 and 0.7 can be used to reliably calculate average crystal size, d(XRD), (Table 4) which are found to be 5.8, 3.3, 2.3 nm respectively. The TiO_2 average crystal size, d(XRD), decreases as the silica loading increases (X decreases). Similarly, the XRD patterns of ZnO, SnO_2 and CuO can be used to reliably calculate average crystal size, d(XRD), only when X=1. Figure 8-3 shows the XRD patterns of particles with X=0.7 demonstrating that the very small crystal sizes which significantly broaden XRD reflections and the presence of amorphous silica render calculations of the average crystal size, d(XRD), for all other flame-made particles considered here unreliable. This challenge was previously encountered by Tani et al in similar flame-made ZnO/SiO_2 particles.[190] The average crystal size, d(XRD) of flame-made TiO_2, ZnO, SnO and CuO (X=1) are 5.8, 28.6, 4.8 and 7.4 nm respectively. The average crystal size, d(XRD) of SnO_2 (X=1), 4.8 nm, is smaller than the exciton Bohr diameter of 5.4 nm.

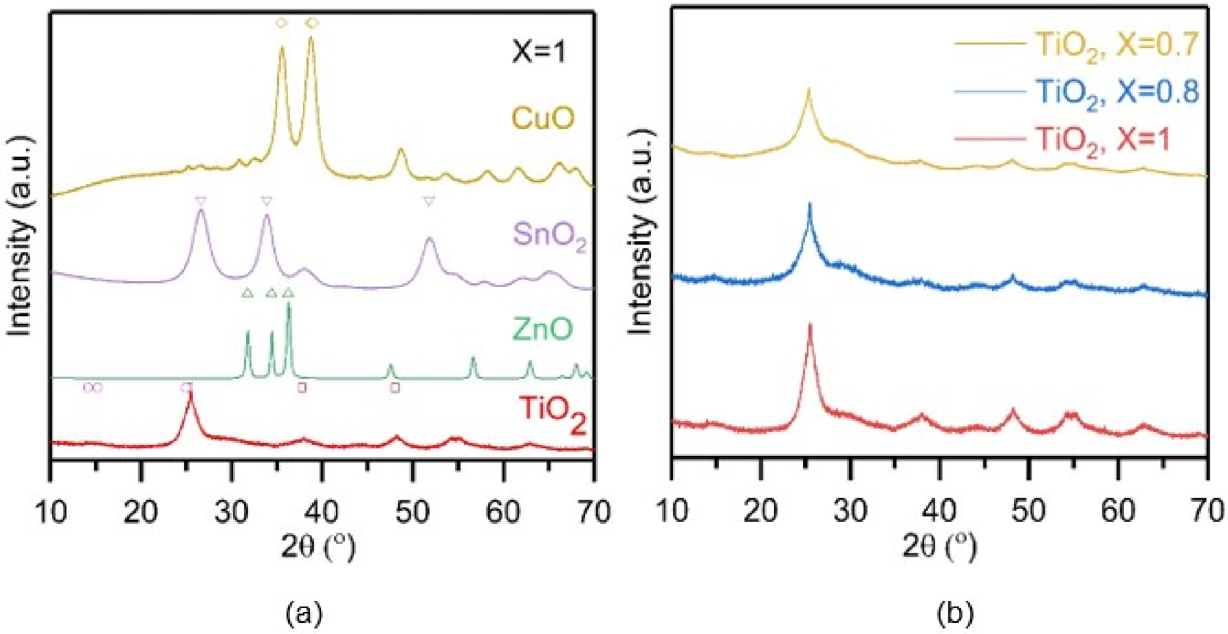

Figure 5-1: XRD patterns of flame-made particles. a) TiO_2, CuO, SnO_2 and ZnO (X=1), and b) TiO_2 (X=1, 0.8 and 0.7). The positions of the most important reflections in standard ICDD XRD patterns of TiO_2 (anatase, PDF card 00-021-1272, squares), TiO_2 (monoclinic, PDF Card 00-46-1238, circles), ZnO (hexagonal, PDF card 00-036-1451, upside triangles), SnO_2 (tetragonal, PDF card 00-041-1445, downside triangles) and CuO (monoclinic, PDF card 00-045-0937, diamonds) are indicated.

Table 4: Size and bandgap energy

Material	d(Bohr) (nm)	X	Crystal and particle sizes (nm)			Bandgap energy (eV)	
			d(XRD)	d(BET)	d(UV-VIS)	Calculated	Measured
TiO_2	2	1	5.8	5.5	2.1	3.2	3.4
		0.8	3.3	5.5	2.1	3.3	3.4
		0.7	2.3	5.6	1.7	3.4	3.5
		0.1		9.0	0.9		4.3
ZnO	2.34	1	28.6	42.0	Bulk	3.2	3.2
		0.8		7.1	8.2		3.4
		0.7		7.8	6.9		3.4
		0.3		4.8	4.3		3.7
		0.1		4.2	2.1		5.4
SnO_2	5.4	1	4.8	5.4	5.2	3.8	3.8
		0.7		4.7	4.0		3.9
		0.5		4.9	3.7		4.0
		0.3		4.9	3.0		4.2
		0.2		5.6	2.7		4.3
		0.1		6.4	2.2		4.7
CuO	7	1	7.4	8.9	4.5	1.6	1.7
		0.9		7.8	3.3		1.9
		0.7		5.5	1.8		2.7
		0.5		5.5	1.7		2.9
		0.3		6.1	1.6		3.0
		0.2		9.6	1.6		3.0
		0.1		10.3	1.4		3.5
		0.05		14.3	1.4		3.7

Table 4 also shows the BET-equivalent particle size, d(BET), calculated from SSA measurements (Table 8 in supplemental information) via Equation 14. The average particle size d(BET) is generally comparable to the average crystal size d(XRD), if not slightly bigger because of the presence of amorphous silica. ZnO is the only exception perhaps because flame-made ZnO particles could have a rod-like shape[192] (Figure 8-4), while (BET) calculations from SSA assume spherical particles (Equation 14). As the silica content increases (X decreases), the average particle size, d(BET) decreases to a minimum, levels off and then starts increasing. The presence of such minima has been previously observed in flame-made ZnO quantum dots.[89] The average particle sizes, d(BET), of SnO_2 (X=0.7, 0.5 and 0.3) and of CuO (X=0.7, 0.5 and 0.3) are smaller than their exciton Bohr diameters of 5.4 nm and 7 nm respectively. Since the overall particle size in these cases are smaller than the Bohr diameter then certainly the crystal sizes are also smaller than the Bohr diameter.

Figure 5-2 shows HR-TEM images of flame-made a) TiO_2, b) ZnO, c) SnO_2, and d) CuO with X=0.7. Figure 5-2a shows the lattice spacing of both anatase (0.3 nm) and monoclinic (0.6 nm) TiO_2 crystal structures consistent with our earlier observations[17]. Figure 5-2b shows lattice spacing of a hexagonal (0.27 nm) ZnO crystal structure. Further, Figure 5-2b and Figure 8-5 show the rod-like shape of ZnO mentioned earlier. Figure 5-2c shows lattice spacing of a tetragonal (0.34 and 0.27 nm) SnO_2 crystal structure. Figure 5-2d shows lattice spacing of a monoclinic (0.26 nm) CuO crystal structure. All observed lattice spacings are consistent with XRD patterns (Figure 5-1). We can observe that in all cases crystals are between 2-5 nm in diameter, even though it is difficult to objectively quantify crystal size using imaging techniques. Most importantly, the HR-TEM images do not show outlier large particles normally observed in the case of broad size distributions. Further, we do not observe a silica coating that would be present in a core-shell structure. Instead, we observe distinct amorphous and crystalline domains indicating segregated particles consistent with Teleki's[65] observations of similar metal-oxide/silica particles made using a co-mixing FSP process.

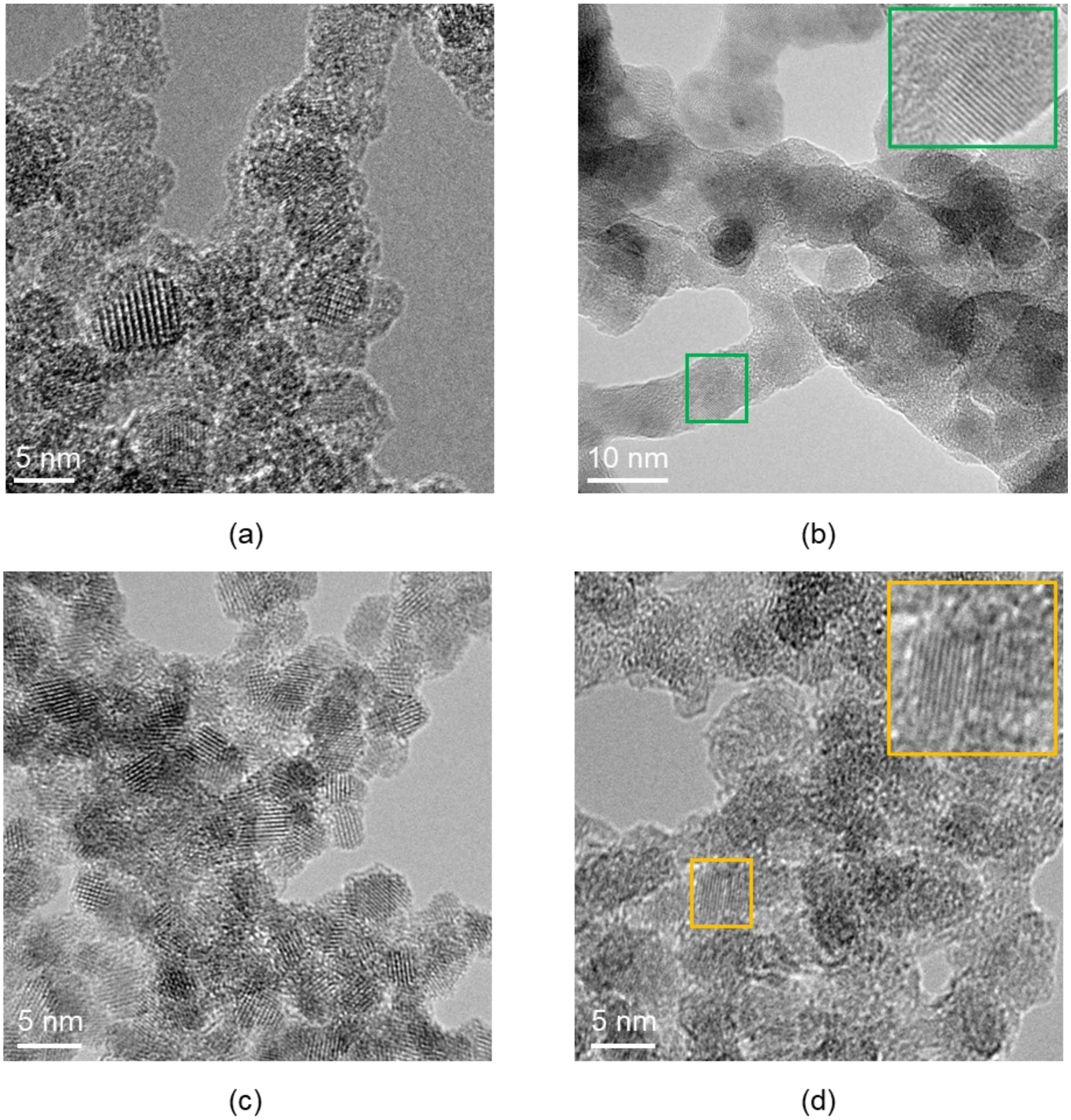

(a) (b) (c) (d)

Figure 5-2: HRTEM of a) TiO2, b) ZnO, c) SnO2, and d) CuO flame-made particles (X=0.7). Insets in b and d are magnifications of observed crystal structures.

Figure 5-3 shows solid-state UV-VIS spectra of TiO_2, ZnO, SnO_2 and CuO flame-made particles with various silica loading. The sudden drop that appears around 3.52 eV is an instrument artifact due to a lamp change. In all cases, as the silica loading increases (X decreases), the absorption on-set shifts to higher energy. This blue shift is consistent with the effect due to quantum confinement predicted by Equation 13 that becomes observable as the crystal size approaches the exciton Bohr diameter calculated in Table 3. It is also important to note that it would be impossible to observe this quantized effect if the particle size distribution were too broad.[42] The inset of Figure 5-3d shows a photograph of flame-made CuO with various silica loading, demonstrating that their absorption is in the visible region. Note that the color of flame-made CuO particles changes from dark red in the case of CuO (X=1), to green in the case of CuO (X=0.7), to blue in CuO (X=0.1) and almost white in the case of CuO (X=0.05). Finally, we observe repeatable anomalous peaks in the spectra of CuO (X=0.5 and 0.3) between 2-2.5 eV, but we are unable to determine their source.

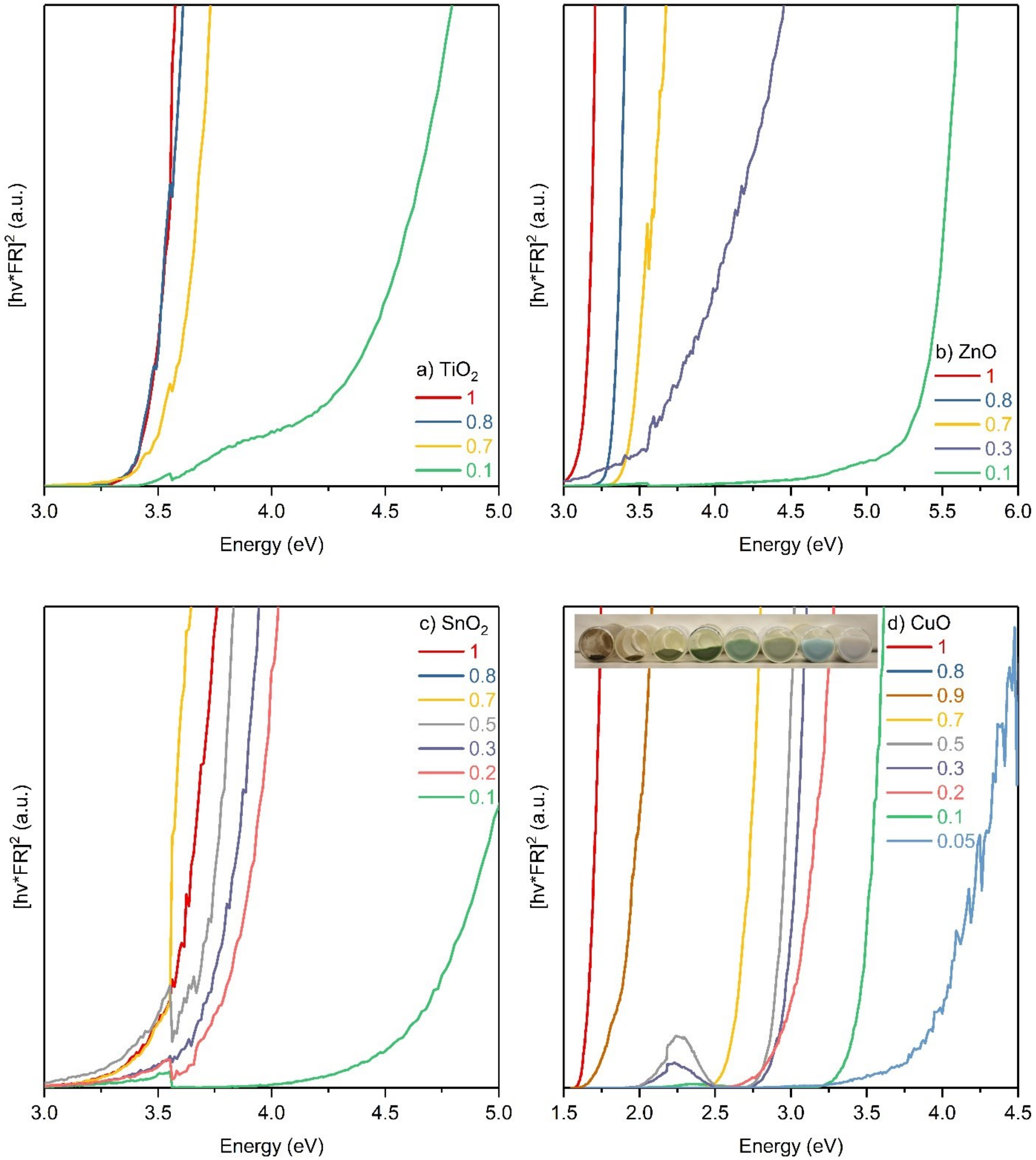

Figure 5-3: Solid-State UV-VIS Tauc plots of flame-made metal oxide semiconducting nanoparticles. a) TiO2, b) ZnO, c) SnO2, and d) CuO (inset: photograph showing the color of the CuO particles, courtesy of Andrew Kingsley Jeyaraj- Copyright 2020). Figure shows a blue shift in band gap energy as silica loading increases, X decreases.

Table 4 shows the measured and theoretical bandgap energies (E*) of the synthesized particles. The band gap energies were measured using the exponential region of the absorption edge as described in the literature using UV-VIS Tauc Plots (Figure 5-3).[193] The theoretical band gap energy is calculated via Equation 2 using the average crystal size d(XRD) (Table 4), when XRD is reliable. The theoretical and measured band gap energies are close, with less than 6% (max 0.2 eV) difference for all flame-made particles without silica (X=1). Further, the measured band gap energies of flame-made TiO_2 with X=0.8 and 0.7 are also consistent with the theoretical values and exhibit a quantized effect (3% error, 0.1 eV difference). In all cases, as the silica loading increases (X decreases), the measured band gap energy increases to higher values consistent with the quantized effect predicted by Equation 13.

Table 4 shows the back-calculated crystal size, d(UV-VIS), associated with the measured bandgap energy determined via Equation 13. The crystal size, d(UV-VIS), is smaller than average particle size, d(BET), in most cases. This is because of the presence of the silica matrix. In one case, d(UV-VIS) is larger than average particle size, d(BET). In addition to experimental uncertainty, this discrepancy is because d(UV-VIS) uses onset absorption stemming from the larger crystals[89], while d(BET) is an average size[194]. In all cases, d(UV-VIS) decreases as silica loading increases (X decreases). The crystal sizes, d(UV-VIS) of flame-made TiO_2 (X=0.7 and 0.1), ZnO (X=0.1), SnO_2 (X=0.7. 0.5, 0.3, 0.2 and 0.1), and CuO (all) are smaller than the respective exciton Bohr diameter (2, 2.34, 5.4, 7 nm).

Porosity is an important factor affecting the particles' ability to catalyze surface reactions. Full adsorption BET isotherms are collected for flame-made SnO_2 (X=1 and 0.3), and plotted in Figure 5-4a. The pore size distribution (Figure 5-4b) indicates that most of the pores fall within the 25-50 nm range. This pore size range is much larger than the particle size, d(BET), as well as

HR-TEM observations (Figure 5-2). This indicates that the pores are intraparticle a result of the aggregation that takes place in the flame. Similar flame-made particles of a catalytic material embedded in a glassy matrix have been observed to exhibit high catalytic activity because the intraparticle pores provide direct access to the catalyst.[83]

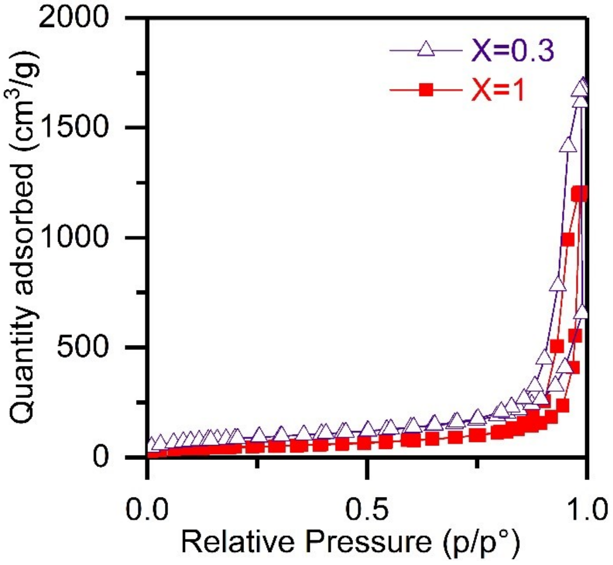

(a)

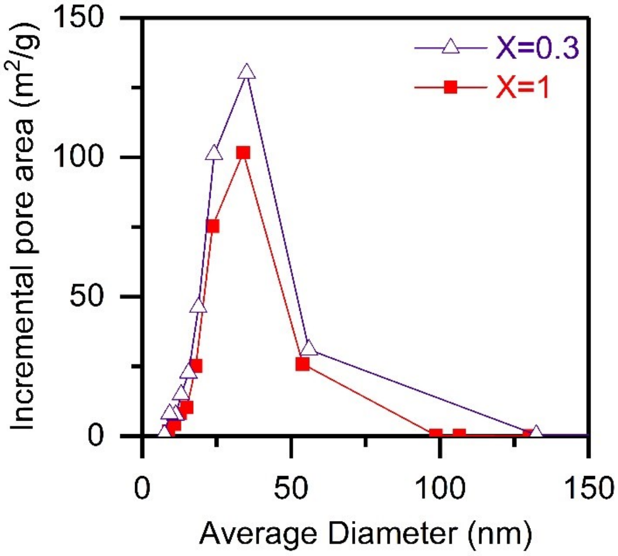

(b)

Figure 5-4: SnO2 (X=1 and 0.3) (a) full isotherms and (b) pore size distribution.

Figure 5-5 shows the epoxy photopolymerization[16] rate initiated by flame made TiO_2 (X=1, 0.8, 0.7 and 0.1) and commercial P25. Flame-made TiO_2 (X=1) show superior photocatalytic performance as compared to commercial P25 titania, the gold standard for photocatalysis.[17] The silica matrix in flame-made TiO_2 (X=0.8 and 0.7) quantum dots slows the reaction but does not prohibit it indicating that the silica matrix does not hermetically seal the semiconducting material surface. The epoxy photocuring reaction catalyzed by flame-made TiO_2 quantum dots (X=0.8 and 0.7) is faster than that catalyzed by P25. The superior performance of flame-made TiO_2 quantum dots whether or not they are embedded in a silica matrix can be attributed to factors including its high surface area (relative to 50 m^2/g in P25 TiO_2), the presence of the monoclinic crystal structure[17], and improved wetting and dispersion because of the silica matrix[64]. On the other hand, the decreasing reaction rate as the silica loading increases (X decreases) can be attributed to the increase in the band gap energy of the particles (Table 4 and Figure 5-3) beyond the energy of light emitted by the UVA source in these photocuring experiments, as well as the decrease in the effective mass of TiO_2. This practically eliminates the reaction when catalysed by TiO_2 (X=0.1), despite the very large surface area of 282 m^2/g.

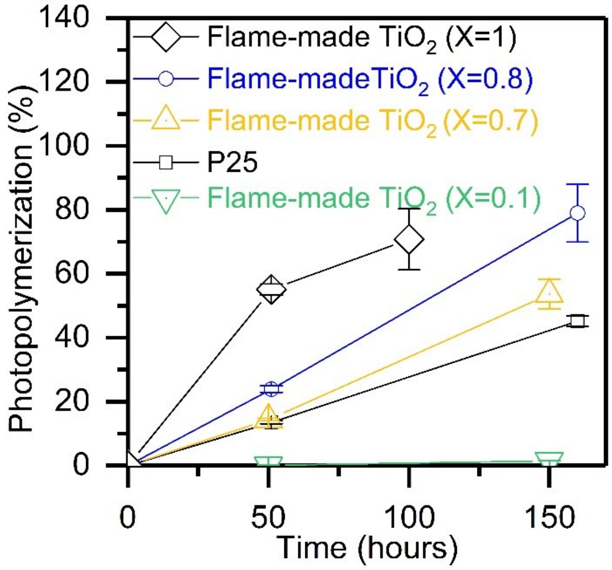

Figure 5-5: Photocatalytic activity of epoxy photopolymerization by flame made TiO_2 (X=0.8, 0.7 and 0.1) compared to commercial P25 TiO_2. Error bars are 90% confidence integrals (n=6).

5.5. Conclusions

We synthesized via flame silica-embedded metal oxide quantum dots of TiO_2, ZnO, SnO_2 and CuO showing that quantum dots of any band gap energy between the dark red side of the visible spectrum to the UVC region can be synthesized by FSP by choosing the appropriate metal oxide material and the silica content. Silica encapsulation enables the use of these quantum dots in various applications requiring higher mechanical, thermal and/or chemical stability than what is afforded by matrix-free quantum dots. The silica matrix of the flame-made metal oxide quantum dots does not hermetically seal the particles allowing particle-surface photocatalytic reactions to take place. Most significantly, the FSP synthesis process allows the mass-production of those silica-embedded metal oxide quantum dots at an industrial scale ready for application use.

5.6. Experimental Section

5.6.1. Particle Synthesis

A solution with 0.25 mol/L total metal concentration is prepared by diluting precursors with xylenes (Sigma Aldrich, Reagent grade). The precursors used are titanium (IV) tetraisopropoxide (Sigma Aldrich, 97%), Zn-2-ethylhexanoate (Strem Materials, 80%), tin-2-ethylhexanoate (Sigma Aldrich, 92.5-100%), copper-2-ethylhexanoate (Strem Materials, 16-19% Cu), hexamethyldisiloxane (Sigma Aldrich, 98.5%) for Ti, Zn, Sn, Cu, Si elements respectively. This solution is fed at 1 mL/min through the capillary of the flame spray pyrolysis reactor and atomized by 3.75 L/min of oxygen. The precursor spray is ignited with a pilot flame fueled by 1.25 L/min of CH_4 premixed with 2.5 L/min of O_2. Product nanoparticles are collected on glass fiber filters (Albet-Hahnemühle, GF 6, 25.7 cm diameter) placed in a water-cooled stainless-steel holder with the help of a vacuum pump (Busch, Seco SV 1040 C). Figure 5-6 depicts the flame synthesis process.

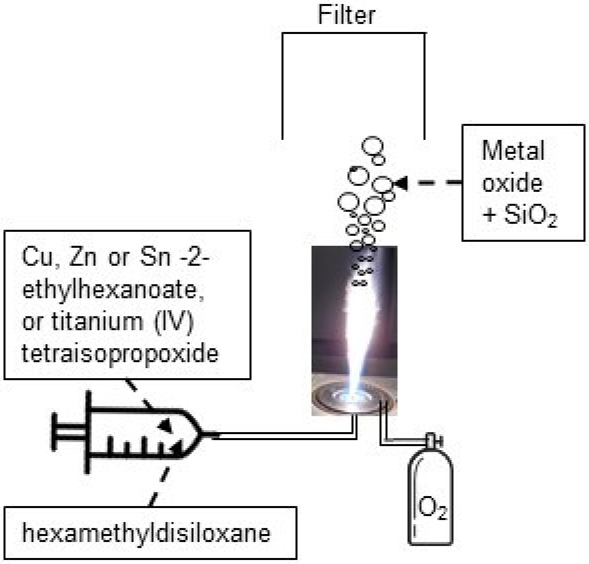

Figure 5-6: FSP synthesis process.

5.6.2. *Characterization*

X-ray powder diffraction (XRD) is performed on a Bruker D8 Advanced diffractometer (Cu Kα radiation, 40 kV, 30 mA, Bragg−Brentano geometry, equipped with Lynxeye detector, 0.02° step size, 2 s/step) in the range of $10° < 2\theta < 70°$. The average crystal size, d(XRD), is calculated using the Rietveld method.[195]

Specific surface areas are determined by nitrogen adsorption (Micrometritics Tristar II) at 77 K employing the Brunauer-Emmett-Teller (BET) isotherm after degassing the sample in nitrogen at 150 °C for at least 2 hours. Average particle size d(BET), in nm, is calculated using Equation 14 from specific surface area measurements using nitrogen adsorption.

$$d(BET) = \frac{6000}{SSA \times \rho} \qquad (14)$$

Where SSA is the specific surface area in m^2/g, and ρ is density in g/cm^3. Our flame-made particles are composites of metal oxides in silica matrix, and therefore Equation 15 is used to calculate their densities (ρ).

$$\rho_{composite} = X \times \rho_{metal\ oxide} + (1 - X) \times \rho_{silica} \qquad (15)$$

The densities[196] of TiO_2 (Anatase), ZnO (Zincite), SnO_2 (Cassiterite), CuO (monoclinic), and silica are as follows 3.79[156], 5.61, 6.85, 6.31, 2.2 g/cm^3, respectively.

For porosity-related measurements, a Tristar 3000 is used to record the full adsorption isotherm of the as-prepared powder. The desorption isotherm is used to determine the pore size distribution.

Solid-state UV-VIS spectra are measured by a Varian Cary 500 UV–vis spectrophotometer equipped with an integrating sphere using samples diluted ten times with barium sulfate (Sigma Aldrich, 99.99%).

Transmission electron microscopy (TEM) images with bright field is performed using a JEOL 2100 F FEG-TEM operated at 200 kV. Images are recorded with a Gatan Ultrascan 1000 camera.

X-ray photoelectron spectroscopy (XPS) spectra are collected using a K-Alpha ThermoScientific spectrometer with an Aluminum Kα, 1486.6 eV source. An X-ray beam size with Φ400 μm is used, and 3 points are measured on the sample surface. To minimize the effect of possible charge on the sample surface, the flood gun generated low energy electrons (plus Ar+ ion) is utilized to compensate charging. The survey scanning to provide the information of element percentage (at.%) for all possible atoms on the sample surface, is set up at a full energy scale, pass energy of 200 eV, scanning step size of 1 eV, dwell time of 50μs, and is an average of 3 scans. The high-resolution scanning to provide the chemical state (bond) information for individual element C, O and Cu, is set up at a specific energy scale (C1s: 274.5 – 298.5 eV; O1s: 524.8 - 544.8 eV, Cu2p: 920-970 eV, pass energy of 50 eV, scanning step size of 0.1 eV, dwell time of 50 μs, and is an average of 10 scans.

Figure 8-5 shows XPS spectra of flame-made copper oxide (X=1, 0.7 and 0.1). Peaks at binding energies of 940-945 eV, and 965 eV exist in CuO but not Cu_2O.[111] Thus, these XPS spectra confirm that the CuO oxidation state is dominant in our flame-made copper oxide whether silica is used or not.

5.6.3. Photocatalytic activity

Mixtures (1.5 g total weight) consisting of 1-4 cyclohexane dimethanol diglycidyl ether (Sigma-Aldrich, technical grade), 10 wt% 1-phenylethanol (Sigma-Aldrich, 99.5%), and 5 wt-% nanoparticles are stirred overnight and then sonicated for 30 minutes while being water-cooled (5 seconds on, 20 seconds off for a total time of 40 minutes, 95% amplitude, 40 W, 100000 J total energy) using a Vibracell VCX 500 equipped with a cup horn. Mixtures are prepared using commercial titania P25 (Evonik) or flame-made TiO_2 (X=0.8). The mixtures are blade-coated on microscope glass slides using 0.0025-inch-thick kapton tape (McMaster-Carr). These films are radiated using a 365 nm UVA lamp (UVP, XX-15M), with a light intensity of approximately 2 mW/cm^2 at the surface of the films. The cure percentage is measured by Fourier transform infrared (FTIR) spectroscopy in ATR mode on 6 different spots of each film using 64 scans at 1 cm^{-1} resolution scanning from 600 cm^{-1} to 4000 cm^{-1} (Bruker Vertex 70v). Additional details are published previously.[16]

6. Photocuring graphene oxide liquid crystals

6.1. Abstract

Graphene is the strongest known material. However, the challenge of translating that strength from the micro to the more useful macro scale remains unmet. Preparing solid structures from self-assembled graphene oxide liquid crystals has allowed the creation of paper and fibers with excellent mechanical properties. Conventionally, vacuum filtration, wet spinning and freeze drying are used to prepare such structures from graphene oxide liquid crystals. Here, we introduce photocuring as an additional option to create solid structures of self-assembled graphene oxide liquid crystals that allows for thicker samples and other shapes to be realized. We assess self-assembly using SEM and XRD, and mechanical properties using nanoindentation and tensile testing. The photocured graphene oxide paper prepared here exhibited comparable mechanical properties to benchmark samples prepared by vacuum filtration.

6.2. Introduction

The discovery of graphene by Nobel laureate Novoselov[90] et al triggered a frenzy of research, and excitement due to its extraordinary properties: physical, mechanical, and electrical. This two-dimensional, one-atom-thin material exhibits a Young's modulus of 1 TPa, and a tensile strength of 130 GPa.[15] Such properties make it the strongest material known but translating them to a macroscopic scale remains a challenge. Griffith[14] demonstrated that the strength of a material fundamentally depends on its structure, and not merely on the intrinsic strength of chemical bonds. The self-assembly of graphene oxide sheets into liquid crystals that can be transformed into solid macroscopic structures is a promising approach to addressing that challenge.

A liquid crystal is a subset of self-assembled amphiphilic nanostructures that has a liquid-like nature and a crystal-like order.[96] This self-assembly process is possible because of the work of Li[99] et al to oxidize hydrophobic graphene to amphiphilic graphene oxide that disperses in water without the use of any agents. The carbonyl groups on the edges of graphene oxide sheets have negative charges leading to electrostatic repulsion enabling its amphiphilicity. Further, the ability of the oxygen containing functional groups to form hydrogen bonds with solvents such as water enables it to "dissolve…forming a homogeneous and stable solution".[100] Amphiphilic graphene oxide sheets can form lyotropic liquid crystals with "nematic" [103], "columnar" [101], or "chiral"[103] phases.

This self-assembly process leads to various kinds of macroscopic structures such as paper and fibers[106]. These solid structures are prepared using various methods including wet-spinning, freeze drying, and filtration, that preserves the ordered structure in the liquid crystal phase. The highest tensile strength achieved for graphene fiber is 1,450 MPa.[107] Dikin[115] et al prepared graphene oxide paper with a 120 MPa tensile strength and a 32 GPa Young's modulus using vacuum filtration of aqueous dispersions.

It is also possible for graphene oxide to form liquid crystals in multiple organic solvents.[129] The magnitude of the electrostatic repulsion force is much lower in organic solvents than in water.[130] Amphiphilic self-assembly, observed in many systems before graphene oxide, is predominantly driven by solvophobic forces in non-aqueous solvents (analogous to hydrophopic effects in water).[131]

Here, we introduce photocuring as a technique to prepare solid structures from graphene oxide dispersions. Since water prevents the cationic photocuring reaction of epoxy, we follow Jalili[121] et al and prepare photocured graphene oxide liquid crystals from dispersions in alcohol: ethylene glycol and 1-phenylethanol (1-PtOH). We demonstrate that the epoxide groups on the basal plane of graphene oxide sheets forming an ordered liquid crystal can "crosslink" into a solid structure with substantial mechanical properties. This opens the door to thicker structures of self-assembled graphene oxide prepared by photocuring multiple layers on top of each other, and maybe shapes other than paper and fibers.

6.3. Results and discussion

Table 5 shows the results of swell experiments conducted to determine if films of graphene oxide dispersions can be photocured. We assess that a film is “solid” if the film does not disperse in either water or alcohol. The films made from dispersions without photo-initiators did not solidify under any conditions including when the samples were UV radiated for 24 hours. Dispersions did not solidify when kept in the dark for a month even when it contained a photo-initiator. Covering the films prevented solidification under UV radiation for 24 hours; in these conditions they are exposed to heat but not light, even when it contained a photo-initiator. On the other hand, when photo-initiators are incorporated, films of graphene oxide dispersions in ethylene glycol and in 1-PtOH solidified when they were UV radiated for 24 hours. These observations indicate that graphene oxide can undergo a photocuring reaction.

Table 5: Swell test results of graphene oxide films on glass slides

Alcohol	Experimental conditions	w/o initiator	w/ initiator
Ethylene glycol	Darkness for a month	Not solid	Not solid
	Bench top UV lamp w Cover for 24 h	Not solid	Not solid
	Bench top UV lamp w/o Cover for 24 h	Not solid	Solid
1-PtOH	Darkness for a month	Not solid	Not solid
	Bench top UV lamp w Cover for 24 h	Not solid	Not solid
	Bench top UV lamp w/o Cover for 24 h	Not solid	Solid

Next, we assess the ordering and mechanical properties of our graphene oxide sheets. For benchmarking, we prepare graphene oxide paper from aqueous dispersion using vacuum filtration as common in the literature[115]. We also prepare graphene oxide paper using vacuum filtration of dispersions in alcohol (either ethylene glycol or 1-PtOH) to assess the effect of photocuring relative to vacuum filtration. Finally, to assess the impact, we anneal graphene oxide paper from the vacuum filtered aqueous dispersions and the photocured dispersions in 1-PtOH. Figure 6-1 shows a photograph of an annealed graphene oxide paper prepared by photocuring a dispersion in 1-PtOH.

Figure 6-1: A photograph of graphene oxide paper prepared by photocuring a dispersion in 1-PtOH followed by annealing, demonstrating its substantial size and uniformity.

Figure 6-2 shows SEM images of the fracture surfaces of various graphene oxide papers. Figure 6-2a and b show the fracture surfaces of the literature benchmark[115] graphene oxide paper prepared via vacuum filtration of the aqueous dispersions with and without annealing. In both cases, we clearly observe ordered layers where the graphene oxide sheets are parallel to one another. Figure 6-2c and d show the fracture surfaces of graphene oxide paper prepared via vacuum filtration of dispersions in alcohol: ethylene glycol and 1-PtOH respectfully. Subjectively, there is some ordering when ethylene glycol is used. On the other hand, we observe clear ordered layers in the case of 1-PtOH where graphene sheets are parallel to one another. Figure 6-2e and f show the fracture surfaces of graphene oxide prepared by photocuring of dispersions in alcohol: ethylene glycol and 1-PtOH respectively. Similarly, our subjective assessment is that there is some ordering in the photocured graphene oxide paper when ethylene glycol is used while we observe clear ordering when 1-PtOH is used. Finally, Figure 6-2g shows the fracture surface of photocured graphene oxide paper of 1-PtOH dispersions followed by annealing. In that case, we observe clear ordered layers where the graphene oxide sheets are parallel to one another. For this system, we observe a relatively large spacing between the photocured graphene oxide sheets in the absence of annealing (Figure 6-2f). The spacing decreases dramatically after annealing (Figure 6-2g).

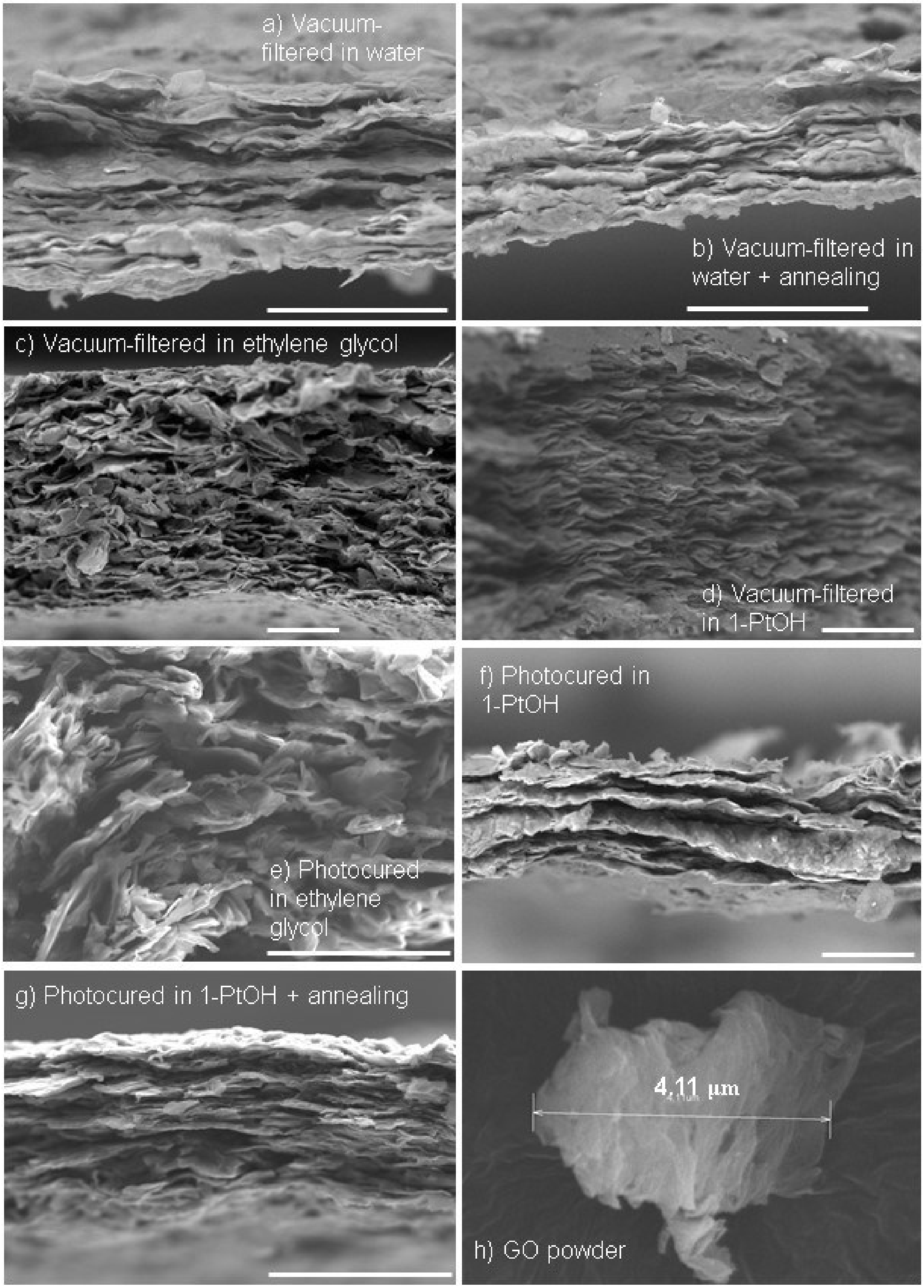

Figure 6-2: SEM images of fracture surfaces of various graphene oxide papers. Scales are 50 µm.

Figure 6-3 shows XRD patterns of various graphene oxide papers. The reflections observed indicate the spacing between the graphene oxide sheets. That spacing between graphene sheets (d) is inversely proportional to the measured incident angle (θ), calculated using the Rietveld method[195], and tabulated in Table 7. We use the Debye-Scherrer equation[197] to calculate the dimension of an ordered stack of graphene oxide using the width of the XRD reflections (Table 6).

Figure 6-3h shows the XRD of the as-purchased Graphene oxide for reference. The spacing in the graphene oxide paper we prepared by vacuum filtration of aqueous solutions (7 Å, Figure 6-3a) is smaller than the 8.3 Å observed by Dikin et al[115]. This can be explained by considering the work done by Chen et al[114] where they observed that d space between graphene sheets decreases from 8.8 Å to 3.7 Å as the carbon to oxygen atomic ratio of the graphene sheets increases from 2.18 to 11.41 (due to reduction of oxygen containing groups). The spacing we observe is consistent with those benchmarks considering that the carbon to oxygen atomic ratio we measured in our graphene oxide powder using XPS is 2.44. We also observe that the d spacing in the annealed paper prepared from aqueous dispersion (6.9 Å, Figure 6-3b) is smaller than it was before annealing (7 Å, Figure 6-3a). This is consistent with the thermal stability studies conducted by Jeong et al[198] who observed that annealing gradually reduces the oxygen containing groups which in turn gradually decreases the spacing between the sheets measured by XRD[107,110,114]. The carbon to oxygen atomic ratio in the annealed paper prepared from an aqueous dispersion is 2.54 as measured by XPS.

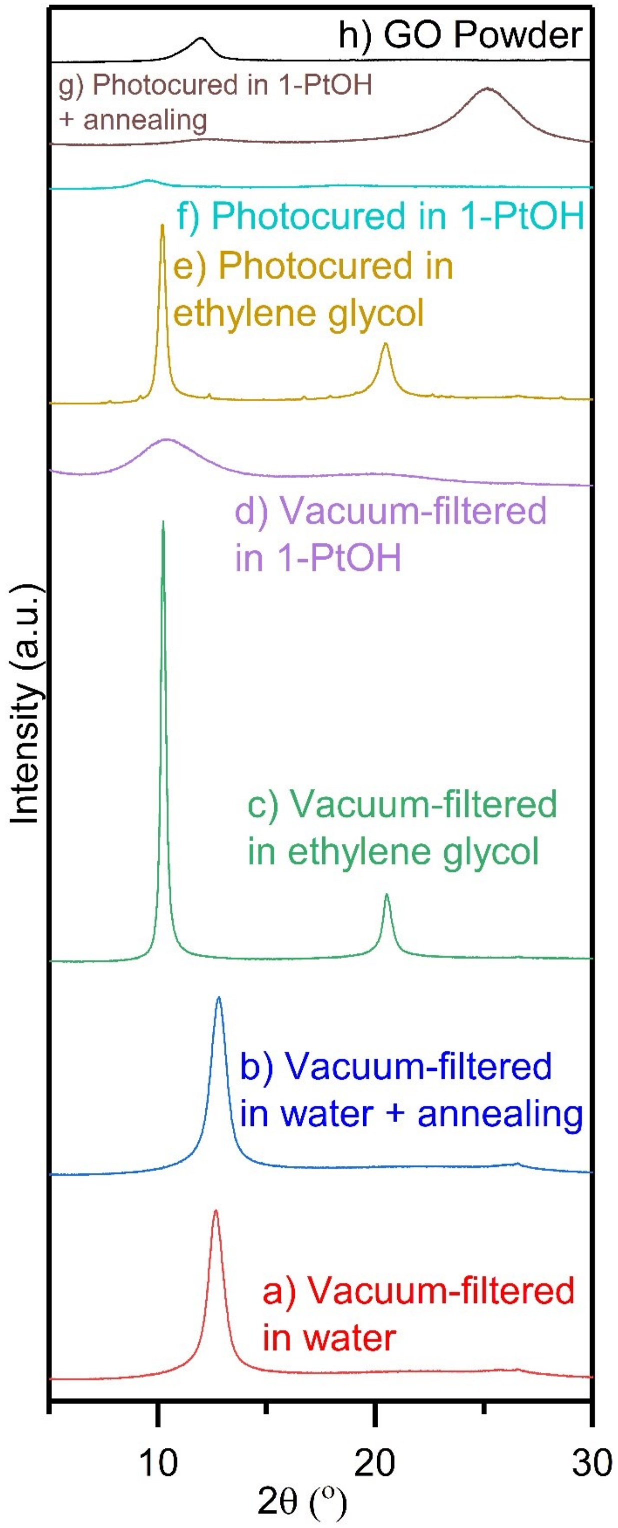

Figure 6-3: XRD patters of graphene oxide paper of various controls.

The main XRD reflection indicates larger spacing between the graphene oxide sheets of vacuum filtered alcohol dispersions in the case of both ethylene glycol (Figure 6-3c, ~8.6 Å) and 1-PtOH (Figure 6-3d, ~8.5 Å) than the observed spacing in the samples prepared from aqueous dispersions (Figure 6-3a, ~7 Å). This is consistent with observations made by Jalili et al[129] indicate the dependance of the d spacing on the medium used. Interestingly, there are two distinct reflections when ethylene glycol is used (Figure 6-3c, 8.6 Å and 4.3 Å). It turns out that ethylene glycol has the ability to reduce oxygen containing functional groups.[199] This reduction decreases the spacing between some of the graphene oxide sheets to the observed 4.3 Å, consistent with the relation between oxygen containing groups and d spacing referenced earlier [114]. Clearly, the graphene oxide is not fully reduced as some epoxide has been used in the photocuring reaction observed in Table 5, and thus the reflection of the 8.6 Å spacing remains. This is supported by XPS measurements indicating that the carbon to oxygen atomic ratio in the vacuum filtered paper from ethylene glycol dispersions is 2.64. We also note that the XRD reflection at 10.5° in the graphene oxide paper prepared by vacuum filtering 1-PtOH dispersions is significantly broader than the reflections observed in other samples. This breadth indicates that the dimension of an ordered stack of graphene oxide in 1-PtOH is 2.6 nm (Table 6) corresponding to about 3 stacked graphene oxide sheets, as calculated using the Debye-Scherrer equation[197]. This is smaller than the dimensions of the ordered stack of graphene in the other systems which ranges from 8.9 in aqueous systems to 28.4 nm in ethylene glycol systems.

Table 6: XRD data

Graphene oxide paper	Spacing between two graphene oxide sheets (Å)		Mean dimension of an ordered stack of graphene oxide (nm)	
	d_1	d_2	d_1	d_2
Vacuum filtered water	7.0		8.9	
Vacuum filtered water + annealing	6.9		8.9	
Vacuum filtered ethylene glycol	8.6	4.3	28.4	15.5
Vacuum filtered 1-PtOH	8.5		2.6	
Photocured ethylene glycol	8.7	4.3	22.1	11.2
Photocured 1-PtOH	9.2		3.1	
Photocured 1-PtOH + annealing	7.2		2.7	

Photocuring increases the spacing observed between the graphene oxide sheets in the samples prepared from alcohol dispersions slightly in the case of ethylene glycol (from 8.6 Å in Figure 6-3c to 8.7 Å in Figure 6-3e), and significantly in the case of 1-PtOH (from 8.5 Å in Figure 6-3d, to 9.2 Å in Figure 6-3g). Annealing clearly makes a significant difference in the spacing between graphene oxide sheets in the photocured paper made from 1-PtOH dispersion as the ~9.2 Å spacing (Figure 6-3f) decreases to ~7.2 Å (Figure 6-3g). Evidently, a significant amount of the dispersant remains in the samples prepared by photocuring and is evaporated by annealing, bringing the graphene oxide sheets closer. This is consistent with the observations made by Lerf et al[200] of the fact that the spacing between the sheets depends on the concentration of the dispersant.

Table 7: Mechanical properties of graphene oxide papers

Graphene oxide paper	**Nanoindentation (n=25)**		**Tensile testing (n≥5)**			
	Er (GPa)		**Tensile strength (MPa)**		**Young's modulus (GPa)**	
	Average	**90% confidence interval***	**Average**	**90% confidence interval***	**Average**	**90% confidence interval***
Vacuum filtered water	0.46	0.02	4	2	0.8	0.2
Vacuum filtered water + annealing	3.2	0.4	6	3	1.1	0.5
Vacuum filtered ethylene glycol	2.8	0.5	1.3	0.5	0.5	0.1
Vacuum filtered 1-PtOH	23	4	5	4	2	1
Photocured ethylene glycol	1.2	0.2	1.0	0.8	0.3	0.2
Photocured 1-PtOH	1.9	0.6	1.7	0.6	0.5	0.3
Photocured 1-PtOH + annealing	2.0	0.4	4	1	1.5	0.7
Two-tail t-test	**P-value****		**P-value****		**P-value****	
Vacuum filtered water w/ and w/o annealing	6.2×10^{-11}		1.4×10^{-1}		3.2×10^{-1}	
Vacuum filtered ethylene glycol and 1-PtOH	3.4×10^{-9}		1.3×10^{-1}		8.1×10^{-2}	
Photocured ethylene glycol and 1-PtOH	5.7×10^{-2}		2.0×10^{-1}		3.1×10^{-1}	
Photocured 1-PtOH w/ or w/o annealing	9.1×10^{-1}		1.1×10^{-2}		2.5×10^{-2}	

$*90\%\ \text{confidence interval} = \text{t statistic value} \times \frac{\text{standard deviation}}{\sqrt{\text{sample size}}}$. For example, there is a 90% probability that the true Er of the vacuum filtered water paper falls in the range 0.46 ± 0.02.

** P-value is the probability that a null hypothesis is true. If the P-value comparing two sets of data is 0.1, then one can have 90% confidence that the two sets are different.

The anisotropic nature of the graphene oxide paper studied here makes the mechanical properties directional. Therefore, we use nanoindentation to measure the mechanical properties in the direction normal to the graphene oxide sheets and we use tensile testing to measure the mechanical properties in the direction parallel to the graphene oxide sheets. The results of both tests are in Table 7, which also includes the P-values of two-tail t-tests to assess the statistical significance in key comparisons. We note that the modulus calculations used in nanoindentation apply to isotropic materials while our graphene oxide paper is anisotropic. However, Hay et al[201] demonstrated that for the Berkovich pyramid indenters, used in this work, the indentation modulus is usually strongly biased toward Young's modulus and provides a useful first-order approximation of it. We also note that the small thickness of the graphene oxide paper involved in this study leads to many challenges in the sample preparation for tensile testing which led to large error bars relative to those in nanoindentation. This source of error makes it more difficult to determine statistically significant differences in key comparisons with a similar confidence level to what we can achieve when comparing nanoindentation data. In all cases, we observe substantial stiffness and strength indicating solid samples.

Consider first the reduced moduli measured by nanoindentation (normal to graphene oxide sheets). We observe an increase (>99% confidence) after annealing in vacuum filtered graphene oxide paper prepared using water, from 0.46 to 3.2 GPa. This increase can be explained by the reduction of oxygen containing groups by annealing as inferred from the XRD observations (Figure 6-3a and b, and Table 5) which restores the structural integrity of the sheets closer to the stronger graphene.

Further, we observe a much higher (>99% confidence) reduced modulus in vacuum filtered graphene oxide paper prepared from 1-PtOH dispersions (23 GPa) than that of graphene oxide paper prepared from ethylene glycol dispersions (2.8 GPa). This can be explained by the fact that ethylene glycol reduces the functional groups on the graphene oxide sheets so significantly that ordering is reduced (visible in Figure 6-3c and d), that there are much fewer functional groups to create bonds between the graphene oxide sheets compromising the formation of the liquid crystals, as can be inferred from SEM images (Figure 6-2c and d) and mechanical properties are compromised. Similarly, we observe a higher (>94% confidence) reduced modulus in photocured graphene oxide paper prepared from 1-PtOH dispersions (1.9 GPa) than that of photocured graphene oxide paper prepared using ethylene glycol dispersions (1.2 GPa). We have been unable to observe any statistically significant difference in the reduced modulus due to annealing the photocured graphene oxide paper prepared from 1-PtOH dispersions. Unlike vacuum filtered graphene oxide paper, the functional groups in photocured graphene oxide paper are already utilized in the photocured samples in the forms of crosslinks and are unaffected by annealing. Notably, all the photocured samples are weaker than the ones prepared via vacuum filtration from the dispersions using the same alcohol. This is likely because the vacuum forces lead to better packing than our photocuring procedure. Finally, we note that the reduced modulus of photocured graphene oxide paper prepared from 1-PtOH dispersions (1.9 GPa unannealed and 2 GPa annealed) are comparable to our benchmark samples prepared using vacuum filtration of aqueous dispersions common in the literature (0.46 GPa unannealed and 3.2 GPa annealed).

Next, consider the tensile strength and Young's moduli measured by tensile testing (parallel to the graphene oxide sheets). First, we note that the benchmark graphene oxide paper we prepared by vacuum filtering aqueous dispersions have lower tensile strength and Young's modulus (4 MPa and 1.1 GPa respectively) than those prepared by Dikin et al[115] (120 MPa strength and 32 GPa Young's modulus). This is likely because of the difference in the properties of the starting graphene oxide such as lateral size and degree of oxidation; both are known factors directly affecting the formation of liquid crystals and the resulting mechanical properties[122,126]. Figure 6-2h shows that the lateral size of our starting graphene oxide is 4.11 μm, which is much smaller than the ~30 μm commonly found in the graphene oxide, liquid crystal literature[110].

Annealing the graphene oxide paper prepared by vacuum filtering aqueous dispersions increases both tensile strength (from 4 to 6 MPa, 86% confidence) and Young's modulus (from 0.8 to 1.1 GPa, 68% confidence). Additionally, graphene oxide paper prepared by vacuum filtering 1-PtOH dispersions has higher tensile strength (5 MPa, 87% confidence) and Young's modulus (2 GPa, 92% confidence) than those prepared by vacuum filtering ethylene glycol dispersions (1.3 MPa strength and 0.5 GPa modulus). This increase is likely due to the reduction of the oxygen containing groups by ethylene glycol compromising both ordering of graphene oxide sheets and bonding as discussed earlier. Similarly, graphene oxide paper prepared by photocuring 1-PtOH dispersions has higher tensile strength (1.7 MPa, 80% confidence) and Young's modulus (0.5 GPa, 69% confidence) than those prepared by photocuring ethylene glycol dispersions (1 MPa strength and 0.3 GPa modulus). Finally, unlike with the nanoindentation observations, the annealing of photocured graphene oxide paper prepared from 1-PtOH dispersions significantly improves the mechanical properties: tensile strength (from 1.7 to 4 MPa, >99% confidence) and Young's modulus (from 0.5 to 1.5 GPa, 98% confidence). Annealing removes a significant amount of the remaining dispersant bringing the graphene oxide sheets closer as observed in SEM (Figure 6-2c and d) and XRD (Figure 6-3c and d). This closer packing leads to stronger bonds between the graphene oxide sheets that improves the mechanical properties in the direction parallel to the graphene sheets but does not affect those normal to the graphene sheets. Nonetheless, the tensile strengths and Youngs moduli of all photocured samples are smaller than those of the papers prepared using vacuum filtration of the same dispersant, indicating that there remains room for improvement in the photocured sample preparation procedure. Finally, we note that the annealed photocured graphene oxide paper prepared using 1-PtOH has comparable tensile strength and Young's modulus (4 MPa and 1.5 GPa respectively) to our benchmark samples prepared using vacuum filtration of aqueous dispersions common in the literature (Unannealed: 4 MPa and 0.8 GPa respectively, and annealed: 6 MPa and 1.1 GPa respectively).

6.4. Conclusions

We demonstrate that it is possible to photocure graphene oxide liquid crystals. The photocured graphene oxide paper we prepared has comparable mechanical properties to benchmark graphene oxide paper prepared by vacuum filtering aqueous dispersions in both directions relative to the graphene oxide sheets: normal (reduced modulus measured by nanoindentation) and parallel (Young's modulus and tensile strength measured by tensile tests). There remains significant potential to improve the mechanical properties of the photocured graphene paper by optimizing the sample preparation procedure, the quality of the starting graphene oxide and exploring the use of other alcohols as dispersant.

6.5. Experimental section

Graphene oxide (S Method, product #: GNOS0010) powder are purchased from ACS materials and used as is. Ethylene glycol (99.5%), 1-phenylethanol (98%) and bis(4-methylphenyl)iodonium hexafluorophosphate (photoinitiator, 98%) are purchased from Sigma Aldrich and used as is.

6.5.1. Sample preparation

Graphene oxide aqueous dispersions at a concentration of 3 mg/mL are prepared using di-ionized water. Batches of 40 ml are sonicated and then vacuum filtered for 3 hours. This process is repeated to make two layers. The sample is then peeled from the filter paper. Some samples were then annealed at 120 °C for 2 hours.

Graphene oxide paper prepared using alcohol dispersions followed a similar procedure but with a concentration of 12 mg/mL, batch volume of 25 mL, and the samples were dried under room conditions for 2 days before vacuum filtering overnight.

Photocured samples are prepared by first preparing a 2 wt% solution of photocuring initiator in the alcohol. Batches consisting of 9 g of those solutions and 0.12 g of graphene oxide are sonicated. Those dispersions were poured onto a filter paper and left to dry for 4 hours followed by photocuring under a benchtop UVA lamp (Model: UVP XX-15 L, peak emission: 365 nm, light intensity at sample surface: 4 mW/cm^2). Samples prepared from ethylene glycol dispersions are photocured until solid (72 hours per layer) and consist of 4 layers. Samples prepared from 1-PtOH dispersions are photocured until solid (24 hours per layer) and consist of 2 layers. Samples were then peeled from the filter paper. Some of the samples prepared from 1-PtOH dispersions are annealed at 190 °C for 2h. Note that the number of layers is different for the two systems because the samples prepared with ethylene glycol were too fragile to remove from the filter paper with fewer than 4 layers. This is consistent with the differences in mechanical properties observed (Table 7) which would have been amplified had they had the same number of layers.

6.5.2. Characterization

SEM was conducted with a Hitachi S-3400N Scanning Electron Microscope using a secondary electron detector under high vacuum.

XRD is conducted using a D8 Advance from Buker AXS Inc with a Cu (1.5418Å) source using a voltage of 40kV and a current of 40mA. Measurements are performed with the Bragg-Breganto geometry mode, in 0.02° increments and 1 second integration time.

Nanoindentation is used to provide indicators of thin film mechanical properties[202]and is conducted using an STM microscope (Multimode 8 AFM) for imaging and a Hysitron Triboscope equipped with a Berkovich tip for the indentation. The maximum indentation force is 25 μN with a 5-second hold period. We calculate the reduced modulus following Cheng and Cheng[203], and conducted 25 repeats at different locations on the specimen. The largest indentation depth observed is ~100 nm which is much smaller than 10% of the thickness of the thinnest sample (0.07 mm) indicating that we can ignore the influence of the substrate[204].

Tensile testing is conducted on razor cut ~40x12 mm rectangular samples using a Z5 Tensile machine from Hoskin Scientific using a preload of 0.2 N and a strain rate of 1 mm/min. The length and width of the sample are measured using a ruler with a 1 mm resolution. Sample thickness, measured by a micrometer, varied from 0.07 to 0.68 mm depending on the preparation procedure used. The graphene oxide paper samples are glued on garolite bars that are clamped on during the test as shown in Figure 6-4b. The gage length (between the two garolite sticks) is 20 mm, with the rest of the sample is glued to the garolite sticks (~10 mm for each side) to allow for gripping. The machine controls the applied force and measures the change in length. The strain is then calculated by dividing the change in length, as measured by the cross-head movement of the machine, by the initial sample length (~20 mm). The tensile strength corresponds to the maximum stress obtained and the Young's modulus corresponds to the slope of the linear region in the stress-strain curve (an example is shown in Figure 6-4a). At least five repeats are conducted.

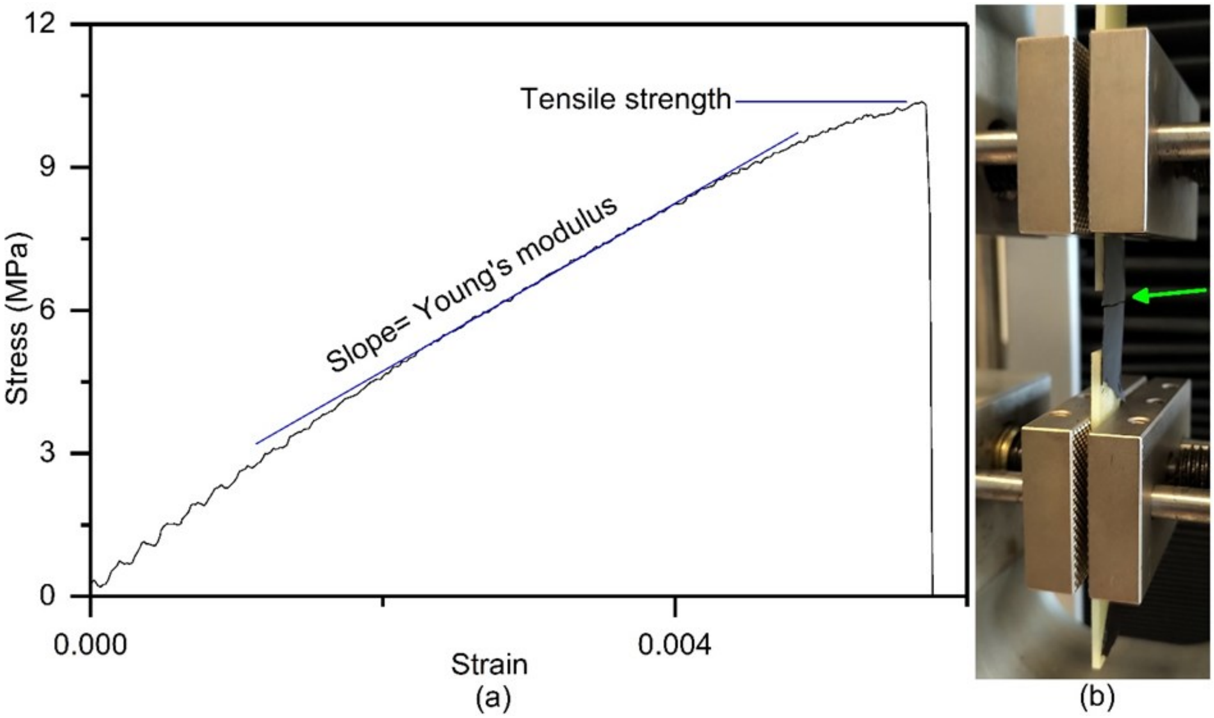

Figure 6-4: a) A typical stress-strain curve obtained from a tensile test of a graphene oxide paper prepared from aqueous dispersion. b) a picture of the tensile test setup after sample fracture (the green arrow points to the fracture site).

X-ray photoelectron spectroscopy (XPS) spectra are collected using a K-Alpha ThermoScientific spectrometer with an Aluminum Kα, 1486.6 eV source. An X-ray beam size with Φ400 μm is used. To minimize the effect of possible charge on the sample surface, the flood gun-generated, low energy electrons (plus Ar+ ions) are utilized to compensate for charging. Survey scanning, to provide the information of element percentage (at.%) for all possible atoms on the sample surface, is set up at a full energy scale, with a pass energy of 200 eV, a scanning step size of 1 eV, and a dwell time of 50μs, is an average of 5 scans. The high-resolution scanning to provide the chemical state (bond) information for individual elements C and O, is set up at a specific energy scale (C1s: 274.5 – 298.5 eV; O1s: 524.8 - 544.8 eV), with a pass energy of 50 eV, a scanning step size of 0.1 eV, and a dwell time of 50 μs, and is an average of 10 scans.

7. Conclusion and Future Work

The ability to design structures unrestrained by manufacturing and assembly limitations is every engineer's dream, brought at our fingertips by the technology of 3D printing, and curtailed by the lack of appropriate materials. For stereolithography 3D printing, those obstacles consist of the photo-instability and the categorical weakness of photocurable epoxy resins. I pursue photostable material by developing photoinitiators that are insensitive to sunlight on Earth. Additionally, I pursue better mechanical properties by using graphene oxide as building blocks of photocurable resin. While further distance remains in the path towards achieving a photostable and strong resin for stereolithography 3D printing, this thesis constitutes multiple distinct steps forward. Specifically, the contributions contained in this thesis are as follows:

1) The introduction of semiconducting nanoparticles as a class of initiators for the photopolymerization of epoxy. One can simply choose from a myriad of widely available metal oxide semiconducting nanoparticle material with standard synthesis to control the wavelength of light that can trigger the epoxy photopolymerization reaction.[16] Further, semiconducting nanoparticles can be cheaper and less toxic than the currently used organic photo initiators. However, the observed reaction kinetic is still too slow to be used in applications.
2) The discovery of a TiO_2(B) crystal structure in flame-made titania. Flame-made titania is mass-produced to the tune of 2 million tons/year constituting a \$4 billion/year industry (data from 2003).[85] Many properties of semiconducting nanoparticles such as band gap energy and catalytic behavior are dictated by the crystal structure(s) these particles consist of. I have demonstrated that the interaction between the TiO_2(B) and anatase crystal

structure makes flame-made titania 2-3 times better photocatalyst in photopolymerizing epoxy than P25 titania, the gold standard of photocatalysis.[17]

3) The introduction of flame spray pyrolysis as a mass production method for a range of silica-embedded quantum dots. One can obtain flame-made quantum dots of any band gap energy from UVC to dark red simply by choosing the metal oxide semiconducting material and silica loading using the one-step flame spray pyrolysis process. The silica matrix improves the mechanical, chemical, and thermal stability of quantum dots. This work generalizes the approach originally adopted by Madler et al[89] for flame-made ZnO quantum dots and applies it to a wider variety of metal oxide quantum dots.[18] The next step in the pursuit of photostable 3D printing resin is to verify that the flame-made quantum dots with bandgap energies larger than 4.1 eV do not trigger an epoxy photopolymerization reaction when exposed to UVA light but only when exposed to UVC light. Then, the photostability should be tested by measuring mechanical properties of UVC-cured parts over time as they are exposed to UVA light to monitor if there are any changes. Finally, optimization studies are required to improve reaction kinetics to allow for use in stereolithography 3D printing and other applications.

4) A demonstration of photocuring graphene oxide liquid crystals into paper-like structures with comparable mechanical properties to literature benchmark samples prepared by vacuum filtration. However, the measured tensile strength of the photocured graphene oxide paper is still weaker than the currently available stereolithography resins (~32 to 54 MPa). Stronger photocured graphene oxide paper requires graphene oxide of much better quality than the commercially available graphene oxide I used. This can be observed from how the properties of the benchmark vacuum filtered aqueous dispersion samples prepared

in this study are more than an order of magnitude weaker than those reported in the literature prepared using the same procedure. As discussed in Chapter 2.3, the properties of liquid crystals are dictated by parameters such as the size magnitude and distribution of graphene oxide and its degree of oxidation. Next, the starting graphene oxide should be optimized to improve the mechanical properties of the photocured graphene oxide paper. Additionally, the fact that vacuum filtered graphene oxide paper prepared from 1-PtOH dispersions are an order of magnitude stronger than the photocured ones using the same alcohol indicates that there remains a wide room of improvement. Therefore, the sample preparation procedure in photocured graphene oxide paper should also be further optimized. Moreover, evidently the alcohol used dictates photocuring kinetics as can be deduced from how 1-PtOH dispersions are much faster to photocure than the ethylene glycol dispersions. Thus, research remains necessary to improve reaction kinetics by, for example, exploring various alcohols. Finally, work should be conducted to create shapes more complicated than "paper" of photocured graphene oxide liquid crystals using a stereolithography 3D printer.

In addition to the next steps outlined above, the two tracks should merge to develop photostable *and* strong stereolithography 3D printing resin. This will come with its own set of challenges. Specifically, graphene oxide is in itself a semiconducting material with its own bandgap energy, and titania has been shown to reduce graphene oxide when irradiated by UVA light.[205] Perhaps, one way to navigate those challenges is by bandgap engineering using multicomponent system, similar to the study by Chuang[136] et al, where the electrons are blocked on the titania surface and prevented from reducing the graphene oxide. Flame spray pyrolysis will prove instrumental in the development of such multicomponent nanoparticle systems at an industrial scale.

8. Appendices

Appendix 1: Supplemental information for Chapter 3

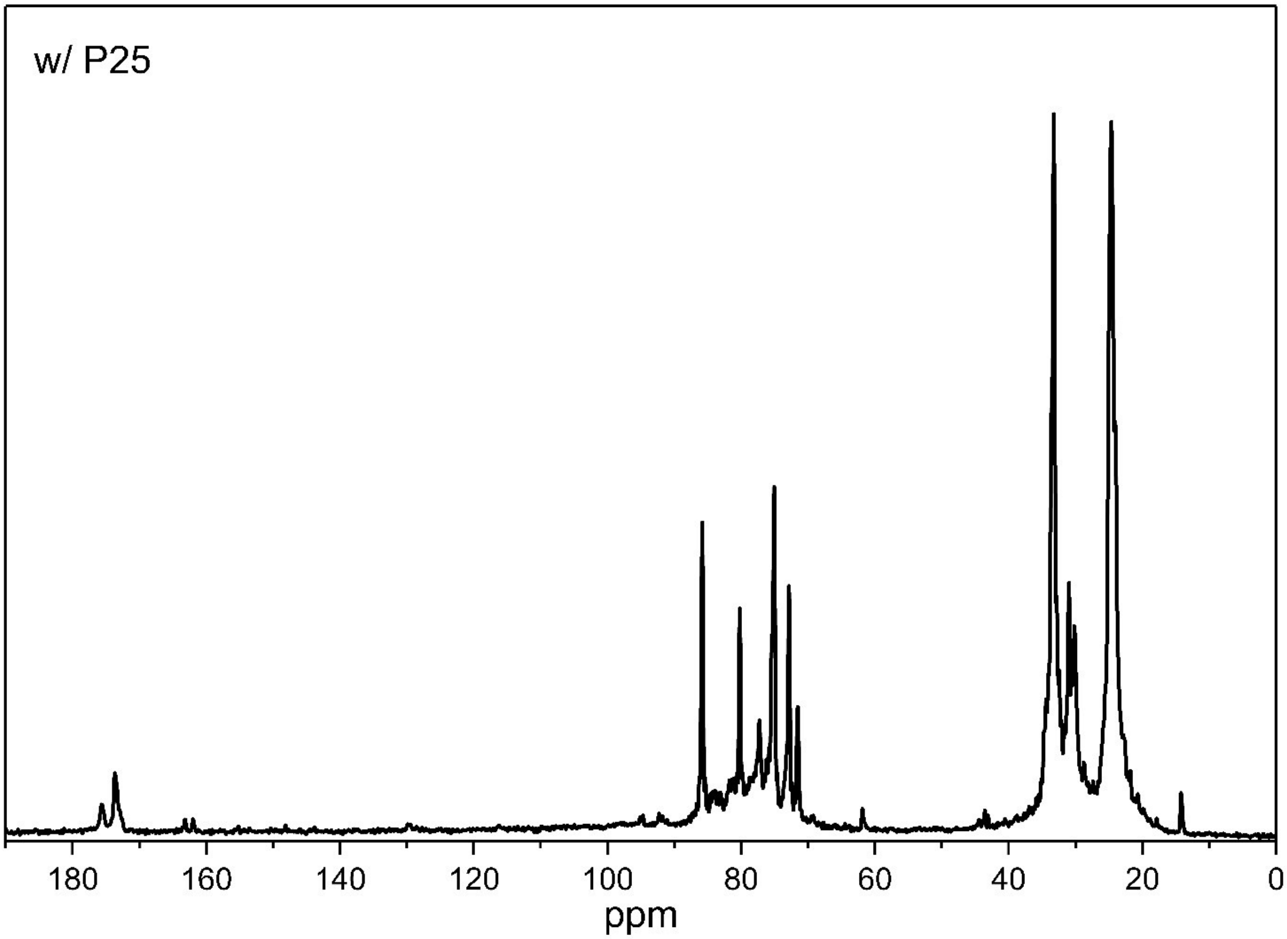

Figure 8-1: Single pulse 13C NMR of sample consisting of cyclohexene oxide, isopropanol and P25 TiO2 showing a ketone peak in the 170-180 PPM region.

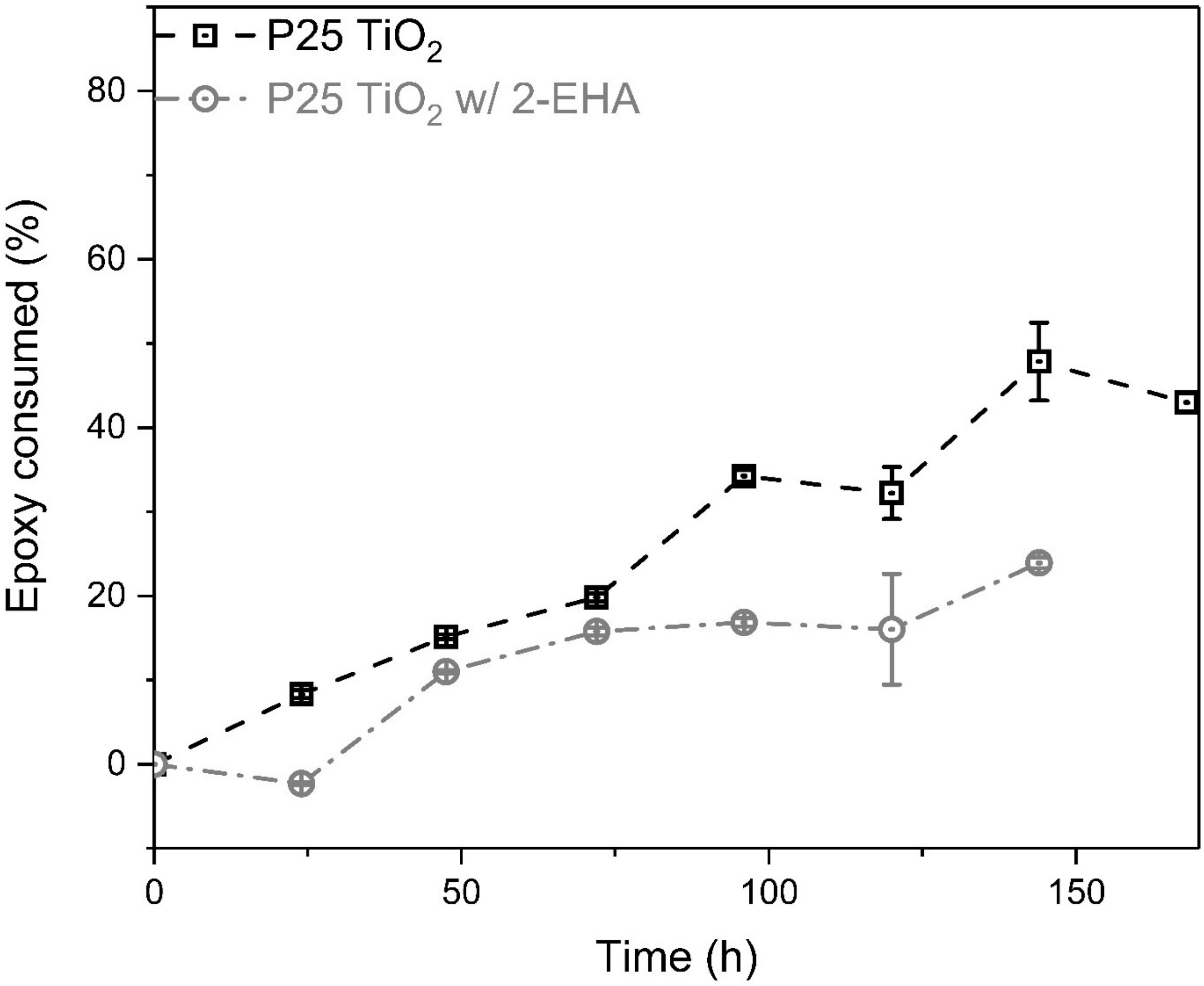

Figure 8-2. Effect of particle coating. Sample consisting of epoxy, isopropanol (5 wt%) and P25 TiO$_2$ (5 wt%) uncoated (black square and dashed line) and coated with 2-EHA (grey circle, and dash and dot line).

Appendix 2: Supplemental information for Chapter 5

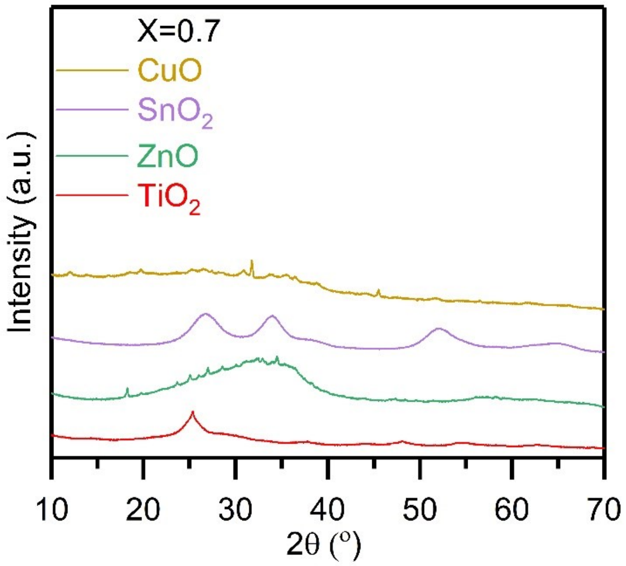

Figure 8-3: XRD patterns of flame-made particles: TiO2, CuO, SnO2 and ZnO (X=0.7).

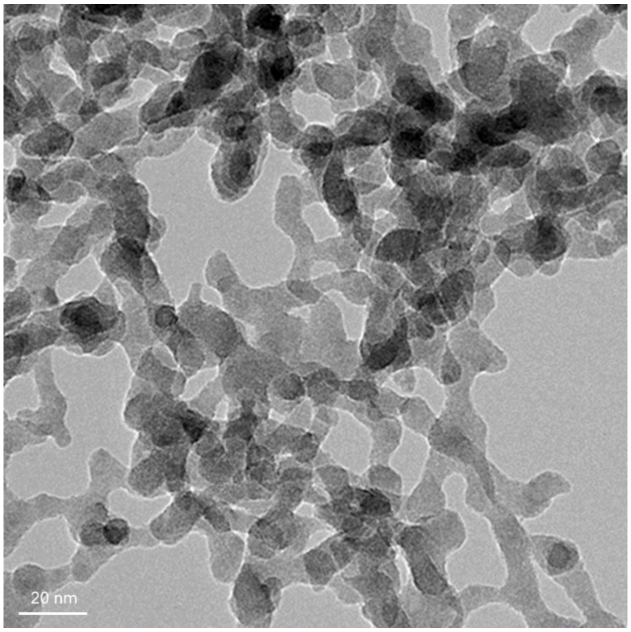

Figure 8-4: HRTEM of ZnO (X=0.7) flame-made particles.

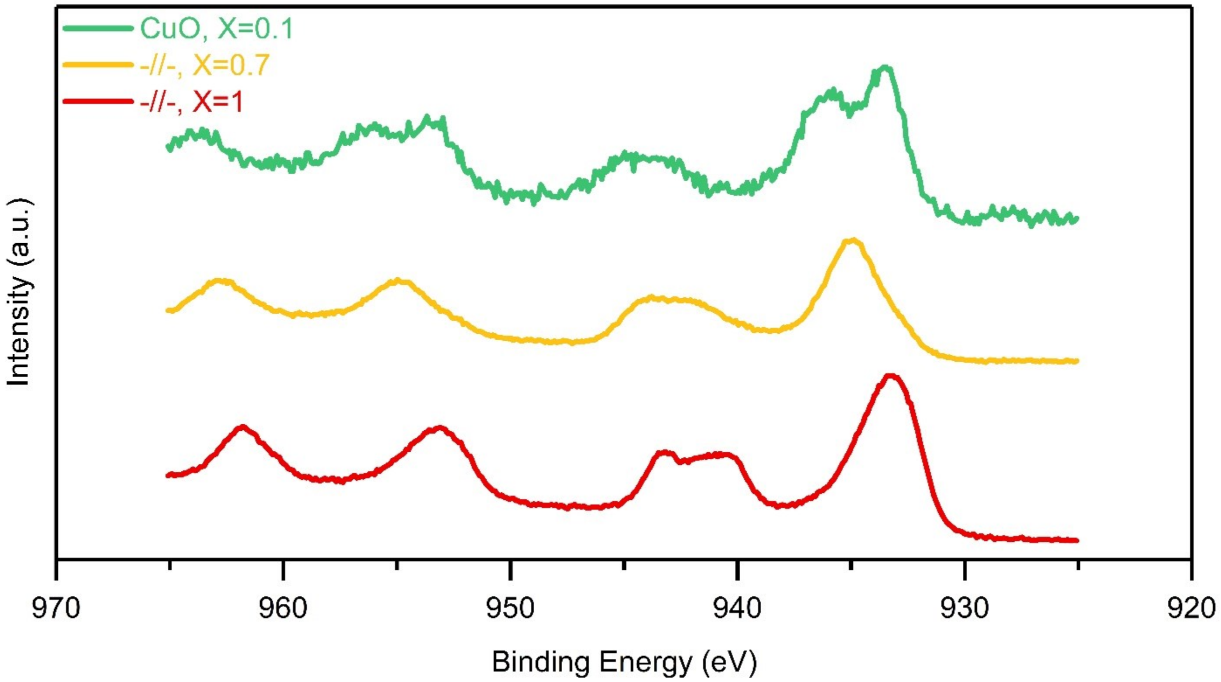

Figure 8-5: XPS spectra of flame-made CuO (X=1, 0.7 and 0.1).

Table 8: BET specific surface area.

Material	X	SSA (m^2)
TiO_2	1	289
	0.8	312
	0.7	323
	0.1	282
ZnO	1	25
	0.8	171
	0.7	168
	0.3	387
	0.1	567
SnO_2	1	162
	0.7	234
	0.5	268
	0.3	340
	0.2	344
	0.1	354
CuO	1	107
	0.9	131
	0.7	215
	0.5	256
	0.3	286
	0.2	207
	0.1	224
	0.05	174

References

---

[1] Riad, K. B. Photocuring epoxy with quantum dots for 3D printing. Master's Dissertation, *Concordia University*, **2016**.

[2] Liou, F. W. Modeling and virtual prototyping in *Rapid Prototyping and Engineering Applications: a Toolbox for Prototype Development*. Boca Raton: CRC, **2008**. Print.

[3] Petrovic, V.; Gonzalez, J. V. H.; Ferrando, O. J.; Gordillo, J. D.; Puchades, J. R. B.; Grinan, L. P. Additive layered manufacturing: sectors of industrial application shown through case studies. *Intternational Journal of Production Research,* **2011**, 49, 1061.

[4] "GE aviation executive, Greg Morris, honored for groundbreaking work in 3D printing". *General Electric Aviation press release*, **2015**.

[5] "Analysis: Aviation Could Consume a Quarter of 1.5C Carbon Budget by 2050." *Carbon Brief,* **2016**.

[6] Chand, S. Carbon fibers for composites. *Journal of Materials Science*, **2000**, 35, 1303.

[7] Riad, K. B.; Schmidt, R.; Arnold, A. A.; Wuthrich, R.; Wood-Adams, P. M. Characterizing the structural formation of epoxy-amine networks: The effect of monomer geometry. *Polymer*. **2016**, 104, 83.

[8] Hare, C. H. The degradation of coatings by ultraviolet light and electromagnetic radiation. *JPCL*, **1992**, 5, 58.

[9] Crivello, J. The discovery and development of onium salt cationic photoinitiators. *Journal of Polymer Science., Part A: Polymer Chemistry,* **1999**, 37, 4241.

[10] Yagci, Y.; Jockusch, S.; and Turro, N. Photoinitiated polymerization: advances, challenges, and opportunities. *Macromolecules.,* **2010,** 43, 6245.

---

[11] Jubsilp, C.; Takeichi, T.; Rimdusit, S. Polymerization Kinetics in *Handbook of Benzoxazine Resins*. **2011**, 157.

[12] Zhang, J.; Huang, Y.; Jin, X.; Nazartchouk, A.; Liu, M.; Tong, X.; Jiang, Y.; Ni, L.; Sun, S.; Sang, Y.; Liu, H.; Razzari, L.; Vetrone, F.; Claverie, J. Plasmon enhanced upconverting core@trible-shell nanoparticles as recyclable panchromatic initiators (blue to infrared) for radical polymerization. *Nanoscale Horizon*, **2019**, 4, 907.

[13] Crivello, J.; Liu, S. Photoinitiated cationic polymerization of epoxy alcohol monomers. *Journal of Polymer Science, Part A: Polymer Chemistry,* **2000**, 38, 389.

[14] Griffith, A. A. *Philosophical Transactions of the Royal Society A: Mathematical, Physical and Engineering Sciences*. **1920**, 221, 163.

[15] Lee, C.; Wei, X.; Kyser, J. W.; Hone, J. Measurement of the elastic properties and intrinsic strength of monolayer graphene. *Science*, **2008**, 321, 385.

[16] Riad, K. B.; Arnold, A. A.; Claverie, J. P.; Hoa, S. V.; Wood-Adams, P. M. Photopolymerization using metal oxide semiconducting nanoparticles for epoxy-based coatings and patterned films. *ACS Applied Nano Materials.* **2020**, 3, 2875.

[17] Riad, K. B.; Wood-Adams, P. M.; Wegner, K. Flame-made TiO_2(B). *Materials Research Bulletin,* **2018**, 106, 276.

[18] Riad, K, B.; Hoa, S. V.; Wood-Adams, P. M. Metal oxide quantum dots embedded in silica matrices made by flame spray pyrolysis. *ACS Omega*, **2021**, 6, 11411.

[19] Peiffer, R. W. Applications of photopolymer technology in *Photopolymerization Fundamentals and Applications.* Washington, DC: American Chemical Society. **1997,** Web.

[20] Leubner, W.; Albert, S.; Unruh, C. Light-Sensitive Polymers for Making Printing Plates. Eastman Kodac Co, assignee. Patent US2861058. November 18, **1958**.

---

[21] Barraud, J.; Gervat, S.; Ratovelmanana, V.; Boutevin, B.; Parisi, J.; Cahuzac, A.; Jocteur, R. Polymer Material of the Polyurethane Acrylate Type for Coating an Optical Fiber or for an Optical Fiber Tape. Alcatel Cable, assignee. Patent US5567794. October 22, **1996**.

[22] Jones, N. Three-dimensional printers are opening up new worlds to research. *Nature*, **2012**, 487, 22.

[23] D'Aveni, R. The 3-D printing revolution. *Harvard Business Review*. May, **2015**, Features.

[24] Hoffman, A.; Yee, H.; Mills, G.; Hoffmann, M. Photoinitiated polymerization of methyl methacrylate using Q-sized ZnO colloids. *The Journal of Physical Chemistry,* **1992**, 96, 5540.

[25] Stroyuk, A.; Granchak, V.; Korzhak, A.; Kuchmii, S. Photoinitiation of buthylmethacrylate polymerization by colloidal semiconductor nanoparticles. *Journal of Photochemistry and Photobiology A: Chemistry,* **2004,** 162, 339.

[26] Kuriacose, J. C.; Markham, M. C. Mechanism of the photo-initiated polymerization of methyl methacrylate at zinc oxide surfaces. *The Journal of Physical Chem*istry, **1961**, 65, 2232.

[27] Morseli, D.; Bondioli, F.; Sangermano, M.; Messori, M. Photo-cured epoxy networks reinforced with TiO_2 in-situ generated by means of non-hydrolytic sol-gel process. *Polymer*, **2012**, 53, 283.

[28] Bierwagen, G. P.; Tallman, D. E. Choice and measurement of crucial aircraft coatings system properties. *Progress in Organic Coatings,* **2001**, 41, 201.

[29] Bell, A. M.; Keltsch, N.; Schweyen, P.; Reifferscheid, G.; Ternes, T. UV aged epoxy coatings-ecotoxicological effects and released compounds. *Water Research X,* **2021**, 12, 100105.

[30] Driel, B. A.; Kooyman, P. J. Berg, K. J.; Schmidt-Ott, A.; Dik, J. A quick assessment of photocatalytic activity of TiO_2 pigments – From lab to conservation studio! *Microchemical Journal,* **2016**, 126, 162.

---

[31] Xiao, P.; Zhang, J.; Dumur, F.; Tehfe, M.; Morlet-Savary, F.; Graff, B.; Gigmes, D.; Fouassier, J.; Lalevee, J. Visible light sensitive photoinitiating systems: recent progress in cationic and radical photopolymerization reactions under soft conditions. *Progress in Polymer Science,* **2015,** 41, 32.

[32] Kamat, P. V.; Scholes, G. D. Quantum dots continue to shine brightly. *The Journal of Physical Chemistry Letters*, **2016**, 7, 584.

[33] Bera, D.; Qian, L.; Tseng, T.; Holloway, P. H. Quantum dots and their multimodal application: A review. *Materials*, **2010**, 3, 2260.

[34] Alivisatos, A. P. Semiconductor clusters, nanocrystals, and quantum dos. *Science,* **1996**, 271, 933.

[35] Ekimov, A. I.; Onuschenko, A. A. Quantum size effect in three-dimensional microscopic semiconductor crystals. *JETP Letters,* **1981**, 34, 345.

[36] Wang, Y.; Herron, N. Nanometer-sized semiconductor clusters: materials synthesis, quantum size effects, and photophysical properties. *The Journal of Physical Chemistry*, **1991**, 95, 525.

[37] Knox, R. S. Theory of excitons in *Solid state physics,* Supplement 5; Academic Press: New York, **1963**.

[38] Alivisatos, A. P.; Harris, A. I.; Levinos, N. J.; Steigerwald, M. L.; Brus, L. E. Electronic states of semiconductor clusters: Homogeneous and inhomogeneous broadening of the optical spectrum. *The Journal of Chemical Physics.,* **1988,** 89, 4001.

[39] Xue, J.; Wang, X.; Jeong, JH.; Yan, X. Fabrication, photoluminescence and applications of quantum dots embedded glass ceramics. *Chemical Engineering Journal,* **2020**, 383, 123082.

[40] Spanhel, L.; Anderson, M. A. Semiconductor Clusters in the sol-gel process: Quantized aggregation, gelation, and crystal growth in concentrated ZnO colloids. *JACS*, **1991**, 113, 2826.

---

[41] Meulenkamp, E.; Synthesis and growth of ZnO nanoparticles. *The Journal of Physical Chemistry B,* **1998**, 102, 5566.

[42] Satoh, N.; Nakashima, T.; Kamikura, K.; Yamamoto, K. Quantum size effect in TiO_2 nanoparticles prepared by finely controlled metal assembly on dendrimer templates. *Nature Nanotechnology*, **2008**, 3, 106.

[43] Xu, X.; Zhuang, J.; Wang, X. SnO_2 quantum dots and quantum wires: Controllable synthesis, self-assembled 2D architectures, and gas-sensing properties. *JACS*, **2008**, 130, 12527.

[44] Lin, K. F.; Cheng, H. M.; Hsu, H. C.; Lin, L. J.; Hsieh, W. F. Band gap variation of size-controlled ZnO quantum dots synthesized by sol-gel method. *Chemical Physics Letters,* **2005**, 409, 208.

[45] Sarkar, S.; Jana, P. K.; Chaudhuri, B. K. Copper (II) oxide as a giant dielectric material. *Applied Physics Letters*, **2006**, 89, 212905.

[46] Redmond, G.; O'Keeffe, A.; Burgess, C.; MacHale, C.; Fitzmaurice, D. Spectroscopic determination of the flatband potential of transparent nanocrystalline zinc oxide films. *The Journal Physical Chemistry A,* **1993,** 97, 11081.

[47] Parhizkar, M.; Singh, S.; Nayak, P. K.; Kumar, N.; Muthe, K. P.; Gupta, S. K.; Srinivasa, R. S.; Talwar, S. S.; Major, S. S. Nanocrystalline CuO films prepared by pyrolysis of Cu-arachidate LB multilayers. *Colloids and Surfaces A: Physicochemical and Engineering Aspects*, **2005**, 277, 257.

[48] Borgohain, K.; Mahamuni, S. Formation of single-phase CuO quantum particles. *Journal of Materials Research*, **2002**, 17, 1220.

[49] Chen, D.; Huang, S.; Huang, Ruting.; Zhang, Qian.; Le, T.; Cheng, E.; Hu, Z.; Chen, Z. Highlights on advances in SnO_2 quantum dots: insights into synthesis strategies, modifications and applications. *Materials Research Letters,* **2018**, 6, 462.

---

[50] Wan, Q.; Huang, J.; Xie, Z.; Wang, T.; Dattoli, E.; Lu, W.; *Appl. Phys. Lett.*, **2008**, 92, 102101.

[51] Ma, J.; Zhang, J.; Wang, S.; Wang, Q.; Jiao, L.; Yang, J.; Duan, X.; Liu, Z.; Lian, J.; Zheng, W. Superior gas-sensing and lithium-storage performance SnO_2 nanocrystals synthesized by hydrothermal method. *CrystEngComm*, **2011**, 13, 6077.

[52] Nath, S. S.; Ganguly, A.; Gope, G.; Kanjilal, M. R. SnO_2 quantum dots for nano light emitting devices. *Nanosystems: Physics, Chemistry, Mathematics*, **2017**, 8, 661.

[53] Tang, Z.; Wong, G.; Yu, P.; Kawasaki, M.; Ohtomo, A.; Koinuma, H.; Segawa, Y. Room-temperature ultraviolet laser emission from self-assembled ZnO microcrystallite thin films. *Applied Physics Letters,* **1998,** 72, 3270.

[54] Rehman, S.; Mumtaz, A.; Hasanain, S. Size effects on the magnetic and optical properties of CuO nanoparticles. *Journal Nanoparticle Research,* **2011**, 12, 2497.

[55] Ben-Mohse, T.; Dror, I.; Berkowitz, B. Oxidation of organic pollutants in aqueous solutions by nanosized copper oxide catalysts. *Applied Catalysis B: Environmental,* **2009**, 85, 207.

[56] Palkar, V.; Ayyub, P.; Chattopadhyay, S.; Multani, M. Size-induced structural transitions in the Cu-O and Ce-O systems. *Physical Review B,* **1996**, 53, 2167.

[57] Fujishima, A.; Honda, K. Electrochemical photolysis of water at a semiconductor electrode. *Nature*, **1972**, 238, 37.

[58] O'Regan, B.; Grätzel, M. A Low-cost, high-effeciency solar cell based on dye-sensitized colloidal TiO_2 films. *Nature*, **1991**, 353, 737.

[59] Leschkies, K. S.; Divakar, R.; Basu, J.; Enache-Pommer, E.; Boercker, J. E.; Carter, B. C.; Kortshagen, U. R.; Norris, D. J.; Aydil, E. S. Photosensitization of ZnO nanowires with CdSe quantum dots for photovoltaic devices. *Nano Letters*, **2007**, 7, 1793.

---

[60] Cai, J.; Li, Z.; Yao, S.; Meng, H.; Shen, PK.; Wei, Z. Close-packed SnO_2 nanocrystals anchored on amorphous silica as a stable anode material for lithium-ion battery. *Electrochimica Acta*, **2012**, 74, 182.

[61] Esteve-turtillas, F. A.; Abad-fuentes, A. Applications of quantum dots as probes in immunosensing of small-sized analytes. *Biosensors and Bioelectronics,* **2013**, 41, 12.

[62] Apte, S. K.; Garaje, S. N.; Naik, S. D.; Waichal, R. P.; Baeg, J. O.; Kale, B. B. Quantum confinement controlled solar hydrogen production from hydrogen sulfide using a highly stable $CdS_{0.5}Se_{0.5}$/CdSe quantum dot-glass nanosystem. *Nanoscale*, **2014**, 6, 908.

[63] Falci, R. F.; Freitas, A. M.; Silva, G. H.; Pinheiro, A. S.; Dantas, N. O.; Anjos, V.; Bell, M. J. V. Quantum efficiency of Yb^{3+}-ZnTe co-doped phosphate glass system. *Journal Luminescence,* **2016**, 176, 381.

[64] Teleki, A.; Akhtar, M. K.; Pratsinis, S. E. The quality of SiO_2-coatings on flame-made TiO_2-based nanoparticles. *J. Mater. Chem.,* **2008**, 18, 3547.

[65] Teleki, A.; Heine, M. C.; Krumeich, F.; Akhtar, M. K.; Pratsinis, S. E. In situ coating of flame-made TiO_2 particles with nanothin SiO_2 films. *Langmuir*, **2008**, 24, 12553.

[66] Wong, E.; Searson, P. ZnO quantum particle thin films fabricated by electrophoretic deposition. *Applied Physics Lett*ers, **1999**, 74, 2939.

[67] Koch, U.; Fojtik, A.; Weller, H.; Henglein, A. Photocemistry of semiconductor colloids. Preparation of extremely small ZnO paricles, fluorescence phenomena and size quantization effects. *Chemical Physics Letters,* **1985**, 122, 507.

[68] Zhu, H.; Yang, D.; Yu, G.; Zhang, H.; Yao, K. A simple hydrothermal route for synthesizing SnO_2 quantum dots. *Nanotechnology*, **2006**, 17, 2386.

---

[69] Hoffmann, M.; Martin, S.; Choi, W.; Bahneman, D. Environmental applications of semiconductor photocatalysis. *Chemical Reviews*, **1995**, 95, 69-96.

[70] Ulrich, G. D. *Chemical and Engineering News*, **1984**, 32, 22.

[71] Teoh, W, Y.; Pratsinis, S. E. Flame spray pyrolysis: an enabling technology for nanoparticles design and fabrication. *Nanoscale*, **2010,** 2, 1324.

[72] Robertson, C. G.; Hardman, N. J. Nature of carbon black reinforcement of rubber: Perspective on the original polymer nanocomposite. *Polymers*, **2021**, 13, 538.

[73] Broek, J.; Bischof, D.; Derron, N.l Abegg, S.; Gerber, P. A.; Guntner, A. T.; Pratsinis, S. E. Screening methanol poisoning with a portable breath detector. *Analytical Chemistry,* **2021**, 93, 1170.

[74] Teleki, A.; Haufe, F. L.; Hirt, A. M.; Pratsinis, S. E.; Sotiriou, G. A. Highly scalable production of uniformly-coated superparamagnetic nanoparticles for triggered drug release from alginate hydrogels. *RSC Advances*, **2016**, 6, 21503.

[75] Kelesidis, G. A.; Kholghy, R. M.; Zuercher, J.; Robertz, J.; Allemann, M.; Duric, A.; Pratsinis, S. E. Light scattering from nanoparticle agglomerates. *Powder Technology*. **2020**, 365, 52.

[76] Pratsinis, S. E. Flame Aerosol Synthesis of Ceramic Powders. *Progress in Energy and Combustion Science,* **1998**, 24, 197.

[77] Tsantilis, S.; Pratsinis, S. E. Soft- and hard-agglomerate aerosols made at high temperatures. *Langmuir,* **2004**, 20, 5933.

[78] Heine, M. C.; Pratsinis, S. E. High concentration agglomerate Dynamics at high temperatures. *Langmuir*, **2006**, 22, 10238.

[79] Kammler, H. K.; Mädler, L.; Pratsinis, S. E. Flame synthesis of nanoparticles. *Chemical Engineering and Technology,* **2001**, 24, 583.

---

[80] Oles, V. Shear-induced aggregation and breakup of polystyrene latex particles. *Journal of Colloid and Interface Science,* **1992**, 154, 351.

[81] Liu, C.; Camacho, J.; Wang, H. Phase equilibrium of TiO_2 nanocrystals in flame-assisted chemical vapor deposition. *ChemPhysChem*, **2018**, 19, 180.

[82] Gröhn A. J.; Pratsinis, S. E.; Sánchez-Ferrer, A.; Mezzenga, R.; Wegner, K. Scale-up of nanoparticle synthesis by flame spray pyrolysis: the high-temperature particle residence time. *Industrial and Engineering Chemistry Research*, **2014**, 53, 10734.

[83] Strobel, R.; Stark, W. J.; Mädler, L.; Pratsinis, S. E.; Baiker, A. Flame-made platinum/alumina: structural properties and catalytic behavior in enantioselective hydrogenation. *Journal of Catalysis*, **2003**, 213, 296.

[84] Mueller, R.; Mädler, L.; Pratsinis, S. E. Nanoparticles synthesis at high production rates by flame spray pyrolysis. *Chemical Engineering Science,* **2003**, 58, 1969.

[85] Wegner, K.; Pratsinis, S. E. Scale-up of nanoparticle synthesis in diffusion flame reactors. *Chemical Engineering Science,* **2003**, 58, 4581.

[86] Paulson, N. H.; Libera, J. A.; Stan, M. Flame spray pyrolysis optimization via statistics and machine learning. *Materials and Design*, **2020,** 196, 108972.

[87] Kelesidis, G. A.; Pratsinis, S. E. A perspective on gas-phase synthesis of nanomaterials: Process design, impact and outlook. *Chemical Engineering Journal*, **2021**, 421, 129884.

[88] Teleki, A.; Pratsinis, S. E. Blue nano titania made in diffusion flames. *Physical Chemistry Chemical Physics,* **2009**, 11, 3742.

[89] Mädler, L.; Stark, W.; Pratsinis S. Rapid synthesis of stable ZnO quantum dots. *Journal of Applied Physics*, **2002**, 92, 6537.

---

[90] Novoselov, K. S.; Geim, A. K.; Morozov, S. V.; Jiang, D.; Zhang, Y.; Dubonos, S. V.; Grigorieva, I. V.; Firsov, A. A. Electric field effect in atomically thin carbon films. *Science,* **2004**, 306*,* 666.

[91] Verdejo, R.; Bernal, M. M.; Romasanta, L. J.; Lopez-Manchado, A. *Journal of Material Chemistry*, **2011**, 21, 3301.

[92] Huang, X.; Qi, X.; Boey, F.; Zhang, H. Graphene-based composites. *Chemical Society Reviews,* **2012**, 41, 666.

[93] Young, R. J.; Kinloch, I. A.; Gong, L.; Novoselov, K. S. The mechanics of graphene nanocomposites: A review. *Composites Science and Technology*, **2012**, 72, 1459.

[94] Du, J.; Cheng, H. The fabrication, properties, and uses of graphene/polymer composites. *Macromolecular Chemistry and Physics*, **2012**, 213, 1060.

[95] Shrestha, L. K.; Strzelczyk, K. M.; Shrestha, R. G.; Ichikawa, K.; Aramaki, K.; Hill, J. P.; Ariga, K. Nonionic amphiphile nanoarchitectonics: self-assembly into micelles and lyotropic liquid crystals. *Nanotechnology*, **2015**, 26, 204002.

[96] Kim, J. E.; Han, T. H.; Lee, S. H.; Kim, J. Y.; Ahn, C. W.; Yun, J. M.; Kim, S. O. Graphene oxide liquid crystals. *Angewandte Chemie,* **2011**, 50, 3043.

[97] Ray, A. Solvophobic interactions and micelle formation in structure forming nonaqueous solvents. *Nature*, **1971**, 231, 313.

[98] Greaves, T. L.; Weerawardena, A.; Drummond, C. J. Nanostructures and amphiphile self-assembly in polar molecular solvents: amides and the “solvophobic effect”. *Physical Chemistry Chemical Physics,* **2011**, 13, 9180.

[99] Li, D.; Müller, M. B.; Gilje. S.; Kaner, R.B.; Wallace, G. G. Processable aqueous dispersions of graphene nanosheets. *Nature Nanotechnology,* **2007**, 3, 101.

---

[100] Neklyudov, V. V.; Khafizov, N. R.; Sedov, I. A.; Dimiev, A. M. New insights into the solubility of graphene oxide in water and alcohols. *Physical Chemistry Chemical Physics,* **2017**, 19, 17000.

[101] Naficy, S.; Jalili, R.; Aboutaleni, S. H.; Grokin, R. A.; Konstantinov, K.; Innis, P. C.; Spinks, G. M.; Poulin, P.; Wallace, G. G. Graphene oxide dispersions: tuning rheology to enable fabrication. *Materials Horizons,* **2014**, 1, 326.

[102] Dreyer, D. R.; Todd, A. D.; Bielawski, C. W. Harnessing the chemistry of graphene oxide. *Chemical Society Rev*iews, **2014**, 43, 5288.

[103] Xu, Z.; Gao, C. Aqueous liquid crystals of graphene oxide. *ACS Nano*, **2011**, 5, 2908.

[104] Pan, H.; Zhu, S.; Mao, L. Graphene nanoarchitectonics: approaching the excellent properties of graphene from microscale to macroscale. *Journal of Inorganic and Organometallic Polymers and Materials*, **2014**, 25, 179.

[105] Zhang, Y.; Gong, S.; Zhang, Q.; Ming, P.; Wan, S.; Peng, J.; Jiang, L.; Cheng, Q. Graphene-based artificial nacre nanocomposites. *Chemical Society Reviews*, **2016**, 45, 2378.

[106] Wu, D.; Zhang, F.; Liang, H.; Feng, X. Nanocomposites and macroscopic materials: assembly of chemically modified graphene sheets. *Chemical Society Reviews*, **2012**, 41, 6160.

[107] Xu, Z.; Liu, Y.; Zhao, X.; Peng, L.; Sun, H.; Xu, Y.; Ren, X.; Jin, C.; Xu, P.; Wang, M.; Gao, C. Ultrastiff and strong graphene fibers via full-scale synergetic defect engineering. *Advanced Materials*, **2016**, 28, 6449.

[108] Cheng, H.; Hu, C.; Zhao, Y.; Qu, L. Graphene fiber: a new material platform for unique applications. *NPG Asia Materials,* **2014**, 6, e113.

[109] Xin, G.; Yao, T.; Sun, H.; Scott, S. M.; Shao, D.; Wang, G.; Lian, J. Highly thermally conductive and mechanically strong graphene fibers. *Science*, **2015**, 349, 1083.

---

[110] Zhang, Y.; Li, Y.; Ming, P.; Zhang, Q.; Liu, T.; Jinag, L.; Cheng, Q. Ultrastrong bioinspired graphene-based fibers via synergistic toughening. *Advanced Materials*, **2016**, 28, 2834.

[111] Jiang, Z.; Li, Q.; Chen, M.; Li, J.; Li, J.; Huang, Y.; Besenacher, F.; Dong, M. Mechanical reinforcement fibers produced by gel-spinning of poly-acrylic acid (PAA) and graphene oxide (GO) composites. *Nanoscale*, **2013**, 5, 6265.

[112] Hu, X.; Xu, Z.; Liu, Z.; Gao, C. Liquid crystals self-templating approach to ultrastrong and tough biomimic composites. *Scientific Reports*, **2013**, 3, 2374.

[113] Xu, Z.; Sun, H.; Zhao, X.; Gao, C. Ultrastrong fibers assembled from giant graphene oxide sheets. *Advanced Materials*, **2013**, 25, 188.

[114] Chen, L.; He, Y.; Chai, S.; Qing, H.; Chen, F.; Fu, Q. Toward high performance graphene fibers. *NanoScale,* **2013**, 5, 5809.

[115] Dikin, D. A.; Stankovich, S.; Zimney, E. J.; Piner, R. D.; Dommett, G. H.; Evmenenko, G.; Nguyen, S. T.; Ruoff, R. S. Preparation and Characterization of graphene oxide paper. *Nature*, **2007**, 448, 457.

[116] Greaves, T. L.; Drummond, C. J. Ionic liquids as amphiphile self-assembly media. *Chemical Society Reviews,* **2008**, 37, 1709.

[117] Onsager, L. The effects of shape on the interaction of colloidal particles. *Annals of the New York Academy of Sciences,* **1949**, 51, 627.

[118] Langmuir, I. The role of attractive and repulsive forces in the formation of tactoids, thixotropic gels, protein crystals and coacervates. *The Journal of Chemical Physics*, **1938**, 6, 873.

[119] Flory, P. J. Statistical thermodynamics of semi-flexible chain molecules. *Proceedings of the Royal Society of London. Series A, Mathematical and Physical Sciences,* **1956**, 234, 60.

---

[120] Khokholov, A. R.; Semenov, A. N. Liquid-crystalline ordering in the solution of long persistent chains. *Physica A : Statistical Mechanics and its Applications,* **1981**, 108, 546.

[121] Jalili, R.; Aboutalebi, S. H.; Esrafilzadeh, D.; Konstantinov, K.; Razal, J. M.; Moulton, S. E.; Wallace, G. G. Formation and processability of liquid crystalline dispersions of graphene oxide. *Materials Horizons Communications*, **2014**, 1, 87.

[122] Aboutalebi, S. H.; Gudarzi, M. M.; Zheng, Q. B.; Kim, J. K. Spontaneous formation of liquid crystals in ultralarge graphene oxide dispersions. *Advanced Functional Materials*, **2011**, 21, 2978.

[123] Behabtu, N.; Lomeda, J. R.; Green, M. J.; Higginbotham, A. L.; Sinitskii, A.; Kosynkin, D. V.; Tsentalovich, D.; Parra-Vasquez, N. G.; Schmidt, J.; Kesselman, E.; Cohen, Y.; Talmon, Y.; Tour, J. M.; Pasquali, M. Spontaneous high-concentration dispersions and liquid crystals of graphene. *Nature Nanotechnology*, **2010**, 5, 406.

[124] Hummers, W. S. Jr.; Offeman, R. E. Preparation of graphite oxide. *JACS,* **1958**, 80, 1339.

[125] Bai, H.; Li, C.; Wang, X.; Shi, G. On the gelation of graphene oxide. *The Journal of Physical Chemistry*, **2011**, 115, 5545.

[126] Oh, J. Y.; Park, J.; Jeong, Y. C.; Kim, J. H.; Seung, J. Y.; Park, C. R. Secondary interactions of graphene oxide on liquid crystal formation and stability. *Particle and Particle Systems Characterization*, **2017**, 1600383.

[127] Van der Beek, D.; Lekkerkerker, N. W. Liquid crystal phases of charged colloidal platelets. *Langmuir,* **2004**, 20, 8582.

[128] Tkacz, R.; Abedin, M. J.; Sheath, P.; Mehta, S. B.; Verma, A.; Oldenbourg, R.; Majumder, M. Phase transition and liquid crystalline organization of colloidal graphene oxide as a function of pH. *Particle and Particle Systems Characterization,* **2017**, 1600391.

---

[129] Jalili, R.; Aboutalebi, S. H.; Esrafilzadeh, D.; Konstantinov, K.; Moulton, S. E.; Razal, J. M.; Wallace, G. G. Organic solvent-based graphene oxide liquid crystals : A facile route toward the next generation of self-assembled layer-by-layer multifunctional 3D architectures. *ACS Nano*, **2013**, 7, 3981.

[130] Du, W.; Wu, H.; Chen, H.; Xu, G.; Li, C. Graphene oxide in aqueous and nonaqueous media: dispersion behaviour and solution chemistry. *Carbon*, **2020**, 158, 568.

[131] Greaves, T. L.; Weerawardena, A.; Fong, C.; Drummond, C. J. Many protic ionic liquid mediate hydrocarbon-solvent interactions and promote amphiphile self-assembly. *Langmuir*, **2007**, 23, 402.

[132] Evans, D. F. Self-organizations of amphiphiles. *Langmuir*, **1988**, 4, 3.

[133] GarcÍa-Tuñon, E.; Barg, S.; Franco, J;. Bell, R.; Eslava, S.; D'Elia, E.; Maher, R. C.; Guitian, F.; Saiz, E. Printing in three dimensions with graphene. *Advanced Materials*. **2015**, 27, 1688.

[134] Xiao, L.; Green, A.; Haque, S.; Mills, A.; Durrant, J. Light-driven oxygen scavenging by titania/polymer nanocomposite films. *Journal of Photochemistry and Photobiology A: Chemistry,* **2004**, 162, 253.

[135] Ilyas, M.; Sadiq, M. Kinetics of heterogeneous solvent-free liquid phase oxidation of alcohol using ZrO2 catalyst with molecular oxygen. *Chinese Journal of Chemistry,* **2008**, 26, 941.

[136] Chuang, C.; Brown, P.; Bulovic, V.; Bawendi, M. Improved performance and stability in quantum dot solar cells through band alignment engineering. *Nature Materials*, **2014**, 13, 796.

[137] Ohtani, B.; Prieto-Mahaney, O.; Li, D.; Abe, R. What is Degussa (Evonik) P25? Crystalline composition analysis, reconstruction from isolated pure particles and photocatalytic activity test. *Journal of Photochemistry and Photobiology A: Chemistry*, **2010,** 216, 179.

---

[138] Emeline, A.; Smirnova, L.; Kuzmin, G.; Basov, L.; Serpone, N. Spectral dependence of quantum yields in gas-solid heterogeneous photosystems: influence of anatase/rutile content on photostimulated adsorption of dioxygen and dihydrogen on titania. *Journal of Photochemistry and Photobiology A: Chemistry*, **2002**, 148, 97.

[139] Fu, Y.; Du, X.; Kulinich, S.; Qiu, J.; Qin, W.; Li, R.; Sun, J.; Liu, J. Stable aqueous dispersion of ZnO quantum dots with strong blue emission via simple solution route. *JACS*, **2007**, 129, 16029.

[140] Güntner, A.; Pineau, N.; Chie, D.; Krumeich, F.; Pratsinis, S. Selective sensing of isoprene by Ti-doped ZnO for breath diagnostics. *Journal of Materials Chemistry B*, **2016,** 4, 5358.

[141] Yahiaoui, A.; Belbachir, M.; Soutif, J.; Fontaine, L. Synthesis and structural analyses of poly (1,2- cyclohexene oxide over solid acid catalyst. *Materials Letters*, **2005**, 48, 759.

[142] González, M.; Cabanelas, J.; Baselga, J. Applications of FTIR on epoxy resins – Identification, monitoring the curing process, phase separation and water uptake in *Infrared Spectroscopy – Materials Science, Engineering and Technology.* **2012**, 261-284.

[143] Neppolian, B.; Sakthivel, S.; Arabindoo, B.; Palanichamy, M.; Murugesan, V. Degradation of textile due by solar light using TiO_2 and ZnO photocatalysts. *Journal of Environmental Science and Health A*, **1999**, 34, 1829.

[144] Crivello, J. Cationic photopolymerization of alkyl glycidyl ethers. *Journal of Polymer Science Part A: Polymer Chemistry*, **2006**, 44, 3036.

[145] Lin, Y.; Chu, T.; Li, S.; Chuang, C.; Chang, C.; Su, W.; Chang, C.; Chu, M.; Chen, C. Interfacial nanostructuring on the performance of polymer/TiO_2 nanorod bulk heterojunction solar cells. *JACS*, **2009**, 131, 3644.

---

[146] Kočí, K.; Obalová, L.; Matějová, L.; Plachá, D.; Lacný, Z.; Jirkovský, J.; Šolcová, O. Effect of TiO_2 particle size on the photocatalytic reduction of CO_2. *Applied Catalysis B: Environmental,* **2009**, 89, 494.

[147] Morselli, D.; Bondioli, F.; Sangermano, M.; Messori, M. Photo-cured epoxy networks reinforced with TiO_2 in-situ generated by means of non-hydrolytic sol-gel process. *Polymer*, **2012,** 53, 283.

[148] Rubab, Z.; Adzal, A.; Siddiqi, H.; Saeed, S. Preparation, characterization, and enhanced thermal and mechanical properties of epoxy-titania composites. *The Scientific World Journal*, **2014**, 515739.

[149] Mikhailov, M.; Li, C.; Neshchimenko, V. Optical property degradation of titanium dioxide micro- and nanopowders under irradiation. *Nuclear Instruments and Methods in Physics Research Section B: Beam Interactions with Materials and Atoms,* **2014**, 333, 52.

[150] Mikhailov, M.; Yuryev, S.; Remnev, G.; Sazonov, R.; Kholodanaya, G.; Ponomarev, D. Effect of temperature on radiation resistance of TiO_2 powders during heating and modification by SiO_2 nanoparticles. *Nuclear Instruments and Methods in Physics Research Section B: Beam Interactions with Materials and Atoms,* **2014**, 336, 96.

[151] Auer, G.; Griebler, W.; Jahn B. White pigments. In *Industrial inorganic pigments*; Buxbaum, G., Pfaff, G., Eds.; Wiley-VCH, **2005**; 51-97.

[152] Akhtar, M. K.; Pratsinis, S. E. Dopants in vapor-Phase synthesis of titania powders. *Journal American Ceramic Society,* **1992**, 75, 3408.

[153] Bickmore, C. R.; Waldner, K. F.; Baranwal, R.; Hinklin, T.; Treadwell, D. R.; Laine, R. M. Ultrafine titania by flame spray pyrolysis of a titanatrane complex. *Journal of the European Ceramic Society,* **1998**, 18, 287.

---

[154] Teoh, W. Y.; Mädler, L.; Beydoun, D.; Pratsinis, S. E.; Amal, R. Direct (one-step) synthesis of TiO_2 and Pt/TiO_2 nanoparticles for photocatalytic mineralisation of sucrose. *Chemical Engineering Science,* **2005,** 60, 5852.

[155] Kho, Y. K.; Teoh, W. Y.; Mädler, L.; Amal, R.; Dopant-free, polymorphic design of TiO_2 nanocrystals by flame aerosol synthesis. *Chemical Engineering Science*, **2011**, 66, 2409.

[156] Banfield, J. F.; Veblen, D. R.; Smith, D. J. The identification of naturally occurring TiO_2(B) by structure determination using high-resolution electron microscopy, image simulation and distance-least-squares refinement. *American Mineralogist,* **1991**, 76, 343.

[157] Fehse, M.; Ventosa, E. Is TiO_2(B) The Future of titanium-based battery materials? *ChemPlusChem,* **2015**, 80, 785.

[158] Fröschl, T.; Hörmann, U.; Kubiak, P.; Kučerovà, G.; Pfanzelt, M.; Weiss, C. K.; Behm, R. J.; Hüsing, N.; Kaiser, U.; Landfester, K.; Wohlfahrt-Mehrens, M. High surface area crystalline titanium dioxide: potential and limits in electrochemical energy storage and catalysis. *Chemical Society Reviews,* **2012**, 41, 5313.

[159] Armstrong, A. R.; Armstrong, G.; Canales, J.; Bruce, P. G. TiO_2-B Nanowires. *Angewandte Chemie International Edition,* **2004**, 43, 2286.

[160] Nuspl, G.; Yoshizawa, K.; Yamabe, T. Lithium intercalation in TiO_2 modifications. *Journal of Materials Chemistry,* **1997**, 7, 2529.

[161] Zukalová, M.; Kalbáč, M.; Kavan, L.; Exnar, I.; Graetzel, M. Pseudocapacitive lithium storage in TiO_2(B). *Chemistry of Materials,* **2005**, 17, 1248.

[162] Armstrong, A. R.; Armstrong, G.; Canales, J.; García, R.; Bruce, P. G. Lithium ion intercalation into TiO_2-B nanowires. *Advanced Materials,* **2005**, 17, 862.

---

[163] Armstrong, G.; Armstrong, A. R.; Bruce, P. G.; Reale, P.; Scrosati, B. TiO_2(B) Nanowires as an improved anode material for lithium-ion batteries containing $LiFePO_4$ or $LiNi_{0.5}Mn_{1.5}O_4$ cathodes and a polymer electrolyte. *Advanced Materials,* **2006**, 18, 2597.

[164] Sun, Z.; Huang, X.; Muhler, M.; Schuhmann, W.; Ventosa, E. A. Carbon-coated TiO_2(B) nanosheet composite for lithium ion batteries. *Chemical Communication,* **2014**, 50, 5506.

[165] Yang, D.; Liu, H.; Zheng, Z.; Yuan, Y.; Zhao, J.; Waclawik, E. R.; Ke, X.; Zhu, H. An efficient photocatalyst structure: TiO_2(B) nanofibers with a shell of anatase nanocrystals. *JACS,* **2009**, 131, 17885.

[166] Yin, S.; Zhang, P.; Liu, B.; Liu, X.; Sato, T.; Xue, D.; Lee, S. W. Microwave-assisted hydrothermal synthesis of monoclinic nitrogen-doped titania photocatayst and its $DeNO_x$ ability under visible LED right irradiation. *Research on Chemical Intermediates,* **2010**, 36, 69.

[167] Marchand, R.; Brohan, L.; Tournoux, M. TiO_2(B) A new form of titanium dioxide and the potassium pctatitanate $K_2Ti_8O_{17}$. *Materials Research Bulletin,* **1980**, 15, 1129.

[168] Kogure, T.; Umezawa, T.; Kotani, Y.; Matsuda, A.; Tatsumisago, M.; Minami, T. Formation of TiO_2(B) nanocrystallitess in sol-gel-derived SiO_2-TiO_2 Film. *Journal of the American Ceramic Society,* **1999**, 82, 3248.

[169] Grosjean, R.; Fehse, M.; Pigeot-Remy, S.; Lorenzo, S.; Monconduit, L.; Cassaignon, S. Facile synthetic route towards nanostructured Fe-TiO_2(B), used as negative electrode for Li-ion batteries. *Journal of Power Sources,* **2015**, 278, 1.

[170] Mädler, L.; Kammler, H. K.; Mueller, R.; Pratsinis, S. E. Controlled synthesis of nanostructured particles by flame spray pyrolysis. *Journal of Aerosol Science,* **2002**, 33, 369.

[171] Mädler, L.; Stark, W. J.; Pratsinis, S. E. Simultaneous deposition of Au nanoparticles during flame synthesis of TiO_2 and SiO_2. *Journal of Materials Research,* **2003**, 18, 115.

---

[172] Waser, O.; Hess, M.; Günther, A.; Novák, P.; Pratsinis, S. E. Size controlled CuO nanoparticles for Li-Ion batteries. *Journal of Power Sources,* **2013**, 241, 415.

[173] Hubbard, C. R.; Synder R. L. RIR -Measurements and use in quantitative XRD. *Powder Diffraction,* **1988**, 3, 74.

[174] Fujiwara, K.; Müller, U.; Pratsinis, S. E. Pd Subnano-clusters on TiO_2 for solar-light removal of NO. *ACS Catalysis,* **2016**, 6, 1887.

[175] Beuvier, T.; Richard-Plouet, M.; Brohan, L. Accurate methods for quantifying the relative ratio of anatase and TiO_2(B) nanoparticles. *The Journal of Physical Chemistry,* **2009**, 113, 13703.

[176] Jossen, R.; Heine, M. C.; Pratsinis, S. E.; Augustine, S. M.; Akhtar, M. K. Thermal stability and catalytic activity of flame-made silica-vanadia-tungsten oxide-titania. *Applied Catalysis B: Environmental,* **2007**, 69, 181.

[177] Kim, S.; Gislason, J. J.; Morton, R. W.; Pan, X. Q.; Sun, H. P.; Laine, R. M. Liquid-feed flame spray pyrolysis of nanopowders in the alumina-titania system. *Chemistry of Materials,* **2004**, 16, 2336.

[178] Ohsaka, T.; Izumi, F.; Fujiki, Y. Raman Spectrum of Anatase, TiO_2. *Journal of Raman Spectroscopy,* **1978**, 7, 321.

[179] Bassi, L. A.; Cattaneo, D.; Russo, V.; Bottani, C. E.; Barborini, E.; Mazza, T.; Piseri, P.; Milani, P.; Ernst, F. O.; Wegner, K.; Pratsinis, S. E. Raman spectroscopy characterization of titania nanoparticles produced by flame pyrolysis: The influence of size and stoichiometry. *Journal of Applied Physics,* **2005**, 98, 074305.

[180] Teleki, A.; Bjelobrk, N.; Pratsinis, S. E. Flame-made Nb- and Cu-doped TiO_2 sensors for CO and ethanol. *Sensors and Actuators B: Chemical,* **2008**, 130, 449.

---

[181] Zhuang, W.; Lu, L.; Li, W.; An, R.; Feng, X.; Xu, X.; Zhu, Y.; Lu, X. In-Situ Synthesized Mesoporous TiO2-B/anatase microparticles: improved anodes for lithium ion batteries. *Chinese Journal of Chemical Engineering*, **2015**, 23, 583.

[182] Brohan, L.; Verbaere, A.; Tournoux, M.; Demazeau, G. La transformation TiO_2(B) →Anatase. *Materials Research Bulletin,* **1982**, 17, 255.

[183] Gröhn, A. J,; Pratsinis, S. E.; Wegner, K. Fluid-particle dynamics during combustion spray aerosol synthesis of ZrO_2. *Chemical Engineering Journal,* **2012**, 191, 491.

[184] Laine, R. M. Liquid feed-flame spray pyrolysis (LF-FSP) in *Ceramics Science and Technology: The Synthesis of Single- and Mixed-Oxide Nanopowders*. Wiley-VCH, **2012**, 102-103.

[185] Kingery, W. D. *Introduction to Ceramics*. John Wiley, **1960**.

[186] Mu, J.; Liu, Y.; Zheng, S. Inorganic-organic interpenetrating polymer networks involving polyhedral oligomeric silsesquioxane and poly(ethylene oxide). *Polymer,* **2007**, 48, 1176.

[187] Fan, Z.; Meng, F.; Gong, J.; Li, H.; Ding, Z.; Ding, B. One-step hydrothermal synthesis of mesoporous Ce-doped anatase TiO_2(B) nanoparticles with enhanced photocatalytic activity. *Journal of Materials Science: Materials in Electronics,* **2016**, 27, 11866.

[188] Meng, F.; Sun, Z. Enhanced photocatalytic activity of silver nanoparticles modified TiO_2 thin films prepared by RG magnetron sputtering. *Materials Chemistry and Physics,* **2009**, 118, 349.

[189] Ge, Y.; Shah, Z, H.; Wang, C.; Want, J.; Mao, W.; Zhang, S.; Lu, R. In situ encapsulation of ultrasmall CuO quantum dots with controlled band-gap and reversible thermochromism. *ACS Applied NanoMaterials International,* **2015**, 7, 26437.

[190] Tani, T.; Mädler, L.; Pratsinis, S. E. Synthesis of zinc oxide/silica composite nanoparticles by flame spray pyrolysis. *Journal of Materials Science,* **2002**, 37, 4627.

---

[191] Spanhel, L.; Anderson, M. A. Semiconductor Clusters in the sol-gel process: Quantized aggregation, gelation, and crystal growth in concentrated ZnO colloids. *JACS*. **1991**, 113, 2826.

[192] Hembram, K.; Sivaprakasam, D.; Rao, T.; Wegner, K. Large-scale manufacture of ZnO nanorods by flame spray pyrolysis. *Journal Nanoparticle Research,* **2013**, 15, 1.

[193] Tauc, J.; Absorption edge and internal electric fields in amorphous semiconductors. *Materials Research Bulletin,* **1970**, 5, 721.

[194] Brunauer, S.; Emmett, P.; Teller, E. Adsorption of gases in multimolecular layers. *JACS*. **1938**, 60, 309.

[195] Cheary, R. W.; Coelho, A. A. Axial divergence in a conventional X-ray powder diffractometer. I. Theoretical Foundation. *Journal of Applied Crystallography,* **1998**, 31, 851.

[196] Haynes, W. M. *CRC handbook of chemistry and physics*. CRC press, **2014**.

[197] Bartram, S. F. in Handbook of X-rays (ed. Kaelble, E. F.) 17.1-17 (Mcgraw-Hill, New York, **1967**).

[198] Jeong, H.; Lee, Y, P.; Jin, M. H.; Kim, E. S.; Bae, J. J.; Lee, Y. H. Thermal stability of graphite oxide. *Chemical Physics Letters*, **2009**, 470, 255.

[199] Liu, T.; Zhang, Y.; Ma, G.; Wang, Z.; Liu, K.; Liu, H. Ethylene glycol reduced graphene oxide/polypyrrole composite for supercapacitor. *Electrochemica Acta*, **2013**, 519.

[200] Lerf, A.; Buchsteiner, A.; Pieper, J.; Schöttl, S.; Dekany, I.; Szabo, T.; Boehm, H. P. Hydration behavior and dynamics of water molecules in graphite oxide. *Journal of Physics and Chemistry of Solids*, **2006**, 1106.

[201] Hay, J. C.; Sun, E. Y. Pharr, G. M. Becher, P. F. Alexander, K. B. Elastic anisotropy of β-silicon nitride whiskers. *J. Am. Ceram. Soc.,* **1998**, 81, 2661.

---

[202] Saha, R.; Nix, W. D. Effects of the Substrate on the Determination of Thin Film Mechanical Properties by Nanoindentation. *Acta Materialia*, **2002,** 50, 23.

[203] Cheng, Y. T.; Cheng, C. M. General relationship between contact stiffness, contact depth and mechanical properties for indentation in linear viscoelastic solids using axisymmetric indenters of arbitrary profiles. *Applied Physics Letters*, **2005**, 87, 111914.

[204] Wang, M.; Liechti, K. M.; White, J. M.; Winter, R. M. *Int. J. Mech. Phys. Sol.,* **2004,** 52, 2329.

TOC

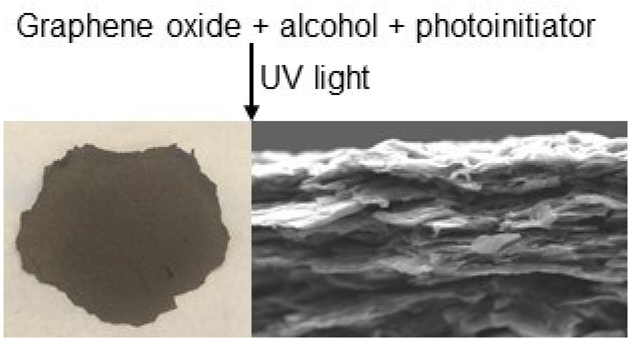

[205] Williams, G.; Seger, B.; Kamat, P. V. TiO_2-graphene nanocomposites UV-assisted photocatalytic reduction of graphene oxide. *ACS Nano*, **2008**, 2, 1487.